Use of CO_2 as working fluid in geothermal systems

Theoretical analysis and system behaviour modelling

PhD Candidate:
Pietro Ungar

Turor:
Prof. Giampaolo Manfrida
Prof. Daniele Fiaschi

April 12, 2024

Abstract

This thesis has focused on the thermodynamic modelling of geothermal wells focusing on the behaviour of such systems using different working fluid. A specific attention has been given to CO_2-based geothermal system, a configuration that has received increasingly more attention in recent years.

In the scope of this thesis two different models have been developed: **a simplified model** based on simple cubic real-gas Equation of State (EoS) has been used to perform a theoretical analysis in order to gain a better understanding of the system behaviour. The results of this analysis are presented in *Chapter 2*. A more **detailed model**, developed to allow more exact estimation of the system performances, is presented in *Chapter 3*. Together with the detailed model, a tool capable of performing exergo-economic analyses has been developed to speed up surface equipment modelling, and is presented in *Appendix A*.

Finally, in *Chapter 4*, a possible application, a geothermal-based High Temperature Heat Pumps (HTHP) for industrial steam production, has been presented.

Keywords: Gethermal, Themodynamics, Well Model, Carbon Dioxide.

Contents

List of Figures

List of Tables

Acronyms

BHE Borehole Heat Exchanger. VIII, 22, 23, 24, 26, 65, 68, 69, 70, 71, 72

CAPEX Capital Expenditure. 88, 89

CHP Combined Heat and Power. 11

CPG CO2 Plume Geothermal. VIII, 10, 11, 23, 24, 26, 63, 68, 72

EEA Exergo-Economic Analysis. 102

EEvA Exergo-Environmental Analysis. 102

EGS Enhanced Geothermal Systems. VIII, 4, 10, 11, 12, 23, 24, 26, 68, 71

EoS Equation of State. II, VII, VIII, XI, 23, 31, 33, 34, 36, 37, 51, 52, 54, 55, 56, 57, 58, 59, 60, 61

FEM Finite Element Method. 67, 77

HDR Hot Dry Rocks. 6, 7

HTHP High Temperature Heat Pumps. II, IX, XI, 87, 88, 90, 91, 92, 93, 94, 95, 97

LCOE Levelized Cost of Heat. 21

NCGs Non-Condensable Gases. 4

OPEX Operational Expenditure. 88, 90

Chapter 1

Introduction

1.1 Geothermal Energy

Geothermal energy, deriving its power from the Earth's natural heat, represents a fundamental pillar of sustainable energy solutions, offering a reliable and continuous source of power. With its roots deeply embedded in the Earth's crust, geothermal energy harnesses the planet's intrinsic thermal energy, which is a result of the Earth's formation and radioactive decay processes. This renewable energy source holds the promise of being a cornerstone in the global transition towards cleaner and more sustainable energy systems.
The incredible amount of energy stored beneath earth surface makes this source of energy almost inexhaustible by any practical means. To put things in perspective, the power leaving the heart crust (which amounts to 47TW [1], more than the mean power required by all human activities, around 20TW in 2022 [2]), requires a time-scale of billions of years to impact earth temperature [3].

1.1.1 Direct uses of geothermal heat

Geothermal heat naturally reaching the surface through hot springs or other forms of thermal emissions has been utilized by humans for thousands of years. Archaeological evidence proves that the practice of thermal balneology, which was later developed by the Romans, was fully established in Southern Tuscany, an area abundant with natural thermal manifestations, as early as the Bronze Age [4]. However, the utilization of geothermal heat remained primarily limited to thermal activities until the 20th century, when other potential applications began to be envisioned.
In recent years, direct uses of geothermal heat have seen a great increase especially for low temperature heating applications (such as, space or greenhouses heating and geothermal heat pumps) as can be seen in *Fig 1.1*. Most of these new installation comes from cold and developed country, with *North-Western Europe* and *North-America* accounting for 47.9% of the global installed power. Additionally, *China* serves as another significant user, accounting for 37.7% of the total [5].
An exceptional case study is that of Iceland, where the combination of favorable geological conditions and the extremely cold environment has resulted in geothermal energy contributing to 90% of the energy utilized for space heating [6].
In this context, Italy, despite having a strong geothermal background, is struggling to keep pace with the global trend, possessing only 1.35 GWt of installed power capacity in 2014 [7], notably lower compared to the 2.59 GWt of installed capacity in France and 4.81 GWt in Germany [5].

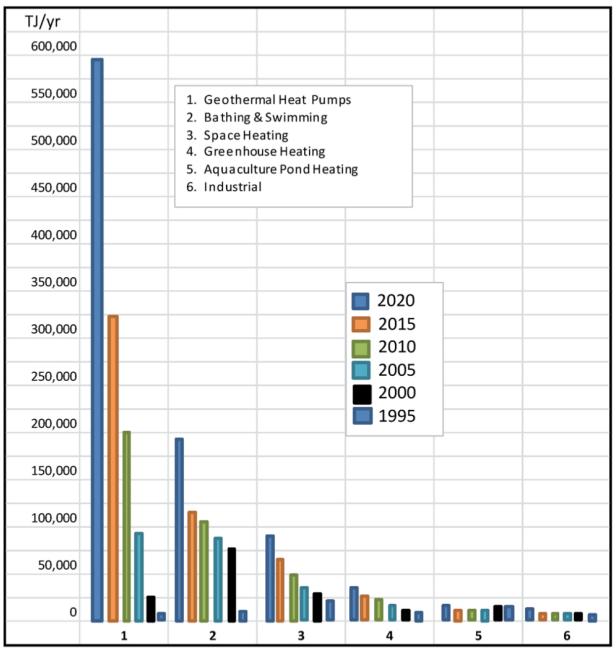

Figure 1.1: Increase in geothermal energy direct uses from 1995 to 2020 for different sector. *Image from Lund (2021) [5]*

This disparity can be attributed to the fact that Italy, characterized by a warmer climate, generally experiences less demand for space heating throughout the year, resulting in a lower *capacity factor*[1] and a slower investment recovery for the installed system.
To stress this, is worth comparing the mean *capacity factors* of the power plants installed in Iceland, 44.9%, and Germany, 19.2% [5], which means that a power plant in Germany produces less than half the energy compared to the same plant installed in Iceland, making profitability harder to achieve.

1.1.2 Electrical energy production

The utilization of geothermal energy for electricity production traces its origins back to the early 20th century in Larderello, a geothermal field located in southern Tuscany, thanks to *Piero Ginori Conti*, an Italian nobleman at the time General Manager of the *Larderello Company*, an established chemical industry in the region focusing on *boric acid* production from hydrothermal water sources [4]. *Ginori Conti* in his efforts to modernize and expand the company's activities, initiated experimental endeavors to assess the feasibility of harnessing energy from the hot water used in boric acid extraction. His initial experiment on July 4, 1904, successfully powered five low-wattage light bulbs, leading to the installation of the first operational geothermal power plant capable of producing 250kW, in 1913 [4].
The experimental power plant in 1904 comprised a reciprocating steam engine that directly received natural steam extracted from the steam vents or fumaroles in the vicinity. To protect the engine from corrosive acid fumes laden with minerals, a cylindrical tank was positioned before the engine to separate a significant portion of the water droplets carried by the steam [8].
Although this configuration worked well in the early years, the power plant realized in 1913 was based

[1]The *capacity factor* is the ratio between the energy produced by a plant and the maximum amount of power the plant could generate if it operated continuously at full capacity during the same period of time

on the *binary cycle* [9], in which power is generated using an external fluid, initially water, heated by the geothermal brine. This change was necessary due to the replacement of the reciprocating engine with a more susceptible steam turbine as the plant scaled up in size [8]. The natural steam started to be used again directly as the power plant working fluid in 1923 after a complex system of steam purification (shown in *Fig 1.2*) was developed.

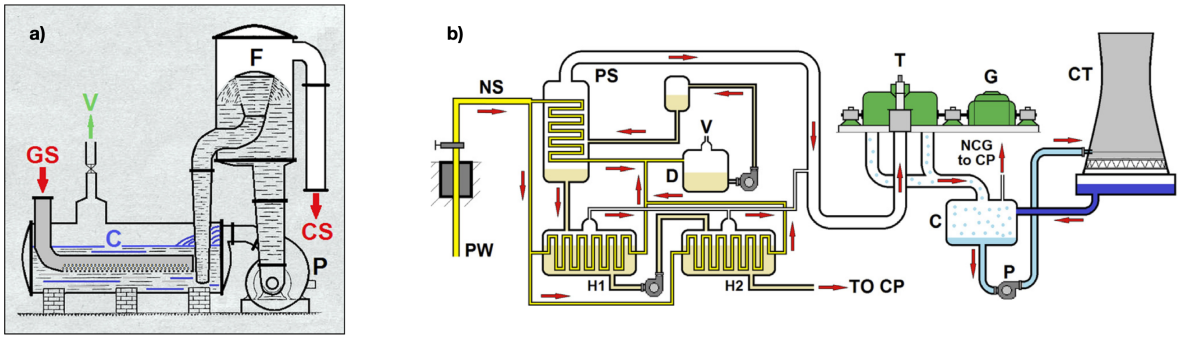

Figure 1.2: Steam deputation system employed in early geothermal power plants for the removal of most of the acid gasses dissolved into the geothermal brine: a) *Bringhenti boiler or "depurator"* installed in the 1923 geothermal power plant. b) Configuration of the 1939 geothermal power plant in Larderello. *Images from Di Pippo (2015) [8], citing Parri (2013) [10]*

Nowadays different plant configuration exists to extract power from the geothermal brine:

- For mid-low temperature resources (<150°C) usually *binary cycles* using some organic refrigerants as working fluid are employed. Such as the ones presented in [11], [12]
- For high temperature water resources (>150°C) *flash or direct steam power plants* are usually employed. An example of this is the Hellisheidy power plant in Iceland [13]

In the locations were it can easily be extracted, geothermal energy has an important in the decolonization of the area. With geothermal production being almost 25% of the overall electrical power production in Tuscany [14] , thanks to the *Larderello* and *Mt. Amiata* geothermal fields, and 30% in Iceland [6].

1.1.3 Current limits to geothermal energy development

Unfortunately, though in general accessible everywhere on the earth surface, as the temperature of the crust increase steadily with depth, the extraction of this source of energy has proven to be economically feasible only in the limited areas where the geothermal gradient is more relevant or if only low temperature heat is needed, such as for domestic use, limiting the depth that has to be reached. Moreover, despite being based on an extremely consolidated technology that also benefits from the know-how and technical innovations developed in the field of hydrocarbon extraction, continues to face some problems that have limited its diffusion over the years, on which research in this field must concentrate.

Emissions, Scaling and Corrosion

Since the geothermal reservoir is often located in an area characterized by magmatic intrusions, the fluid contained within it is sometimes characterized by the presence of Non-Condensable Gases (NCGs) and heavy metals. For example, in the Larderello area, significant concentrations of CO_2 , H_2S, and Hg are recorded [15]. These elements represent the most important technical challenge that engineers must face in order to make a geothermal power plant to work as they are usually associated with scaling deposition and components corrosion.
Scaling deposition usually occurs because the solubility of different salts in water changes with pressure and temperature, leading to their deposition in heat exchangers, making the operation of binary cycles quite challenging. On the other hand, corrosion is often associated with the presence of CO_2 in geothermal brine, which makes the water particles acidic when entrained with the steam. Moreover, these elements must be somehow treated to prevent them from being dispersed into the atmosphere while venting the condenser.
While the scaling and corrosion problems have been addressed by many researchers throughout the years [16]–[19] and can be controlled with a careful planning, emission problems still remains an open question.
Although significant results have already been achieved in this area, such as the reduction of Hg and H_2S emissions from Tuscan plants through the introduction of the AMIS system [15], [20], the elimination of CO_2 emissions remains one of the main objectives that continues to drive research in this sector, as evidenced by the effort made by the European research project GECO.

Economic Feasibility

In a geothermal energy production plant, the installation of surface facilities and well drilling requires a substantial initial investment, estimated at about 75% of the total investment by Sigfusson and Uihlein [21]. This currently limits economically sustainable exploitation to easily accessible resources. In fact, all studies on the prospects of geothermal energy in the coming years [21], [22] assume the assertion of technologies such as EGS, which in some analyses would surpass traditional systems in production volume by 2050 [22], primarily due to a drastic reduction in drilling and installation costs. To quantify this, the table below presents the average investment costs required for the installation of various energy production plants, with data provided by the EIA (US Energy Information Administration) and referred to 2019:

Table 1.1: Investment costs of various energy production plants
Source: EIA Annual Energy Outlook [23]

Technology Used	Investment Cost
Traditional Wind	1319 [$/kW]
Gas Turbine	710 [$/kW]
Geothermal Plant	**2680 [$/kW]**
Hydroelectric Plant	2752 [$/kW]
Photovoltaic Solar	1331 [$/kW]

The same source [23] specifies that since the cost of a geothermal plant is highly influenced by the conditions of the selected location for installation, the reported value is related to the Great Basin

region (Nevada), where most US plants are located. Note, however, that the initial investment for a geothermal system is comparable only to that required for a hydroelectric plant.
Anyhow, despite the high initial investment costs, a geothermal plant has relatively contained operating costs, making the cost of the energy produced still competitive. Unfortunately this has currently limited the installation of geothermal power plant in developed countries, especially for small to medium scales projects like the installation of District Heating networks or of geothermal heat pumps.
To overcome these issues, a large number of solutions have been proposed that pursue two complementary objectives: reducing investment costs and optimizing resource exploitation. To cite some of these: geothermal energy production from wells for the extraction of depleted hydrocarbons [24], [25]; coupling a geothermal plant with a CCS plant where the captured CO_2 is used as a thermal vector instead of water [26], [27]; Recovery of residual heat from the geothermal plant through district heating applications or low-temperature ORC cycles [28].

Social Acceptance

In recent years, in some country the development of new geothermal projects, especially large scale geothermal power plants, have face an increasing resistance from the population of the area, which is a problem shared in general by many renewable energy project [29], [30]. The reasons for this resistance are various and have been addresses in literature [31]–[33]. The referenced studies indicate that limited public awareness about the technology, negative media portrayal, and concerns regarding water use and seismic activity are among the primary factors influencing geothermal acceptance.
While some of the technical problems causing apprehension in the public are being addressed by the researchers [34]–[36], it is interesting to note that many of the reasons for opposition are not technically related. For instance, in 2018, Payera identified, through interviews, a lack of trust in the industrial entity proposing the project as a contributing factor to the lack of support for a proposed geothermal plant in Chile [33].

1.2 CO_2 in Geothermal Systems

In recent years, researchers have begun to explore the potential of employing alternative working fluids in geothermal systems, with CO_2 emerging as the most promising candidate.
This choice is largely attributed to CO_2 's distinct advantages, including its notably lower viscosity compared to water. This lower viscosity facilitates smoother fluid flow, reducing the energy required for pumping within the geothermal system and thus enhancing overall operational efficiency. Furthermore, CO_2 demonstrates low solubility with salt, minimizing the risks associated with corrosion and scale formation, which are persistent challenges in water-based geothermal systems. Additionally, under typical geothermal conditions, CO_2 can be injected into the reservoir with a liquid-like density and retrieved with a gas-like density after being heated up by the surrounding rocks. This transformation allows the formation of a significant thermosyphon effect, which can drive the fluid without the need for a pump.
In this section, we will analyze how the proposal of using CO_2 instead of water has emerged in literature and the current state of the art of the research in this field.

1.2.1 Historical Introduction

An analysis of the literature regarding the utilization of carbon dioxide reveals an intriguing timeline of publications, see *Fig 1.3*. This timeline provides valuable insights into the inception and evolution of this concept, shedding light on its origins and developmental stages.

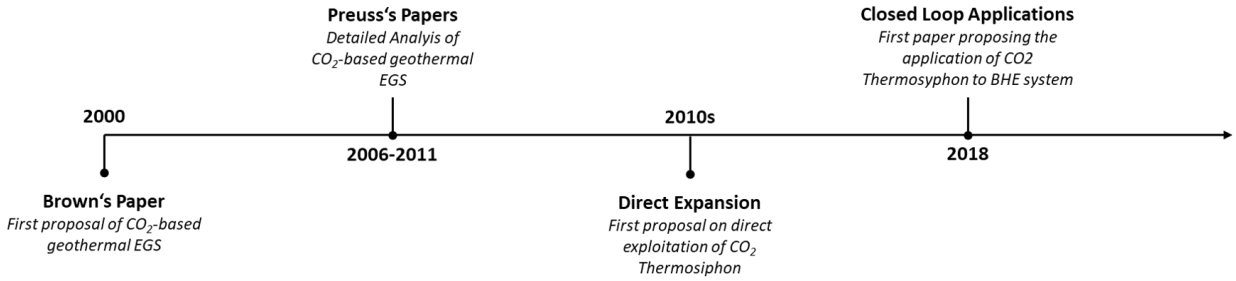

Figure 1.3: Timeline highlighting the key milestones in the proposal for utilizing CO_2 as a working fluid in geothermal systems

Brown's Paper

As shown in *Fig 1.3*, the first publication illustrating the possibility of using CO_2 instead of water in geothermal systems is a conference paper by Brown [37], which was presented in January 2000 during the *Twenty-Fifth Workshop on Geothermal Reservoir Engineering* at the Stanford University in California. Brown was a geologist and a petroleum engineer and has worked in the *Hot Dry Rocks (HDR) Geothermal Development System* at *Los Alamos Scientific Laboratory* since 1971 [38] participating in the analysis of the data acquired from the *Fenton Hill HDR test* site in north-central New Mexico [39]–[41].
In the conference proceedings, Brown pointed out many advantages of the usage of CO_2 , summarized in *Tab 1.2*. Brown's geological expertise prompted him to focus on the challenges related to reservoir behavior, such as scaling issues and silica precipitation limitations that affect water-based

HDR systems, on which he has extensively worked during his career [40], [41]. He realized that sCO_2 could address these challenges effectively, because of its unique properties. The minimization of scaling problems, the potential for operating at higher temperatures, and the environmental benefits of carbon sequestration were all reservoir-driven aspects pointed out by Brown in his research.

Table 1.2: CO_2 advantages from Brown's Paper [37]

CO_2 Property	**Advantages**
Lower Viscosity	Decrease in reservoir pressure loss, reduced pumping power (otherwise significant for water-based systems)
Density Variation	The density difference between the injection and production well generates a thermo-syphon effect that can reduce the pumping power needed to circulate the fluid
Poor solubility for inorganic materials	Almost no minerals will dissolve in the sCO_2 flux within the reservoir, thus drastically reducing the scaling problems that affect most binary geothermal systems. Furthermore, water-based HDR systems are limited to temperatures no higher than 384°C due to silica precipitation issues. sCO_2 does not dissolve silica and is therefore not constrained by this limit.
Environmental Impact	sCO_2 will be sequestered in the reservoir (up to 2 million ton of sCO_2 is expected to be sequestrated in a reservoir with the same condition as the one developed during the Fenton Hill Project) resulting in a huge environmental benefit.

Brown's work, although pioneering and revolutionary, also exhibited certain limitations. In fact, being only a conference paper is notable absence of detailed modeling making Brown's suggestions primarily relied on rough estimations and anticipated behaviors.
For instance, when evaluating system pressurization, Brown employed a simplified approach by determining the mean density along the injection and production wells for an isothermal transformation and use the difference between the two to estimate the natural pressurization effect. In another instance, he estimated the amount of CO_2 sequestration in the reservoir by converting observed water losses from their experimental activities.

Pruess's Work

Perhaps due to these limitations or the fact that it was initially presented only as a conference paper, Brown's groundbreaking proposal remained relatively unnoticed by the scientific community for several years. The first researcher to begin working on Brown's suggestions was Pruess, a Senior Scientist at the Lawrence Berkeley National Laboratory, who was already renowned as one of the principal architects of the TOUGH simulator [42], a testament to his profound expertise in reservoir simulation. It is likely that Pruess was present at Stanford during Brown's presentation, as he coauthored five works during that conference [43]–[47]. Furthermore, he was already working on a related topic, having supervised a PhD thesis on the disposal of carbon dioxide into saline aquifers in 2003 [48].
Anyway, it wasn't until 2006 that Pruess published his first scientific work on the topic [49], which is the initial contribution of a series of related publications over the following years [50]–[60].
Again, due to his background, his research mainly focuses on the reservoir analysis. The importance

of Pruess work is that, due to his expertise in reservoir modelling, he was able to model and predict the behaviour of a sCO_2 EGS system. In contrast, Brown's analysis remains confined to a qualitative description and preliminary calculations.
In his first and most cited work [49], Pruess evaluate the the buoyant drive for both sCO_2 and water by considering both an *isothermal* and an *isoenthalpic* model for production and injection wells. Moreover he provides detailed calculation of the reservoir behaviour with time.
Presented results were extremely promising showing that CO_2 will provide an enormous buoyancy drive and that the overall flow rate of CO_2 will be 4 time grater with respect to water in the same condition resulting in a 50% increase in extracted heat.
In the same work, Pruess also perform a sensitivity analysis proving that the advantages of using CO_2 instead of water increased as pressure and temperature of the reservoir decrease. Meaning that CO_2 can be of great interest also for low-temperature application.
In the following years, in collaboration with his colleagues, Pruess addressed a variety of complex modeling challenges for CO_2 -based EGS systems, including:

- Analyzing the geologic storage process of CO_2 , considering both diffusion [56] and of chemical reactive transport [58]
- Investigating geochemical processes occurring in the reservoir, such as salt dissolution and water-CO_2 interactions [52], [59]
- Examining the interaction between rocks and CO_2 [51], [61]

Subsequent Works Citing Pruess or Brown

The work of Pruess allow other scientist to discover Brown idea and start working on it, as clearly result from the analysis of the number of yearly citation of both Pruess's and Brown's works resulting from a *Goolge Scholar* query and plotted in *Fig 1.4*

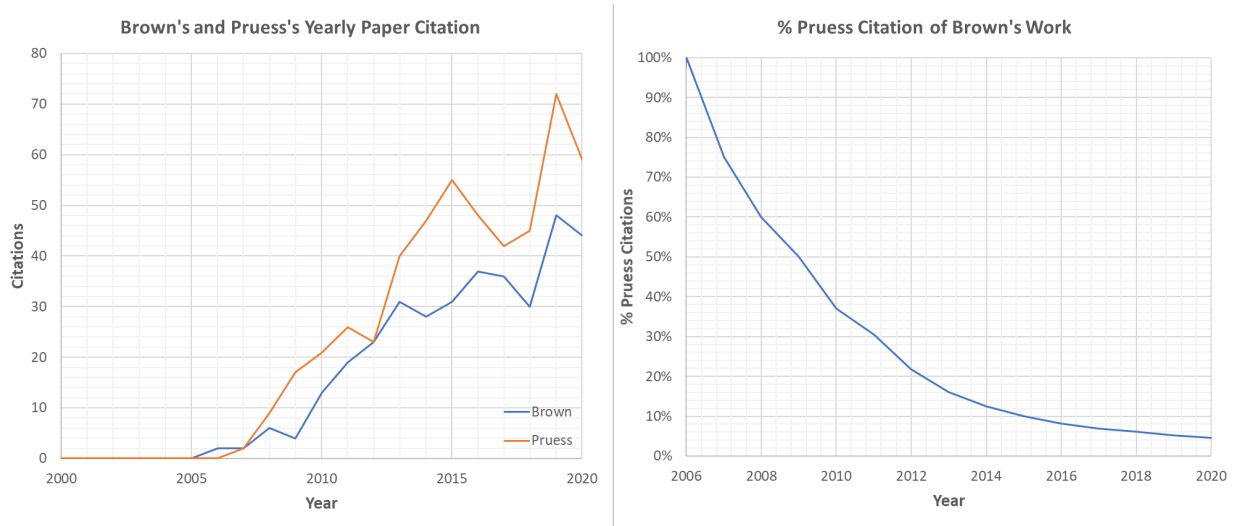

Figure 1.4: Comparison between Pruess's and Brown's works yearly citations: *Left*, Brown paper [37] (blue) an Pruess's main work [49] (Orange) new citation by year. *Right*, percentage of Preuss's works over Brown [37] overall citation

From *Fig 1.4*, it is evident that not only was Brown's work not cited until the publication of Pruess's paper, but also that during the first few years, the majority of citations to Brown came from Pruess itself, clearly indicating that the scientific community become aware of Brown proposal trough the publications of Pruess.
Further analysis of the literature citing either Pruess or Brown, shown in *Fig 1.5*, reveals that the field they initiated has become quite popular, with over 700 published works identified on *Google Scholar*.
It is interesting to note that almost immediately a distinction emerges, with 40% of the published works citing Pruess exclusively, while 20% cite only Brown, and the remaining 40% acknowledge the work of both researchers.

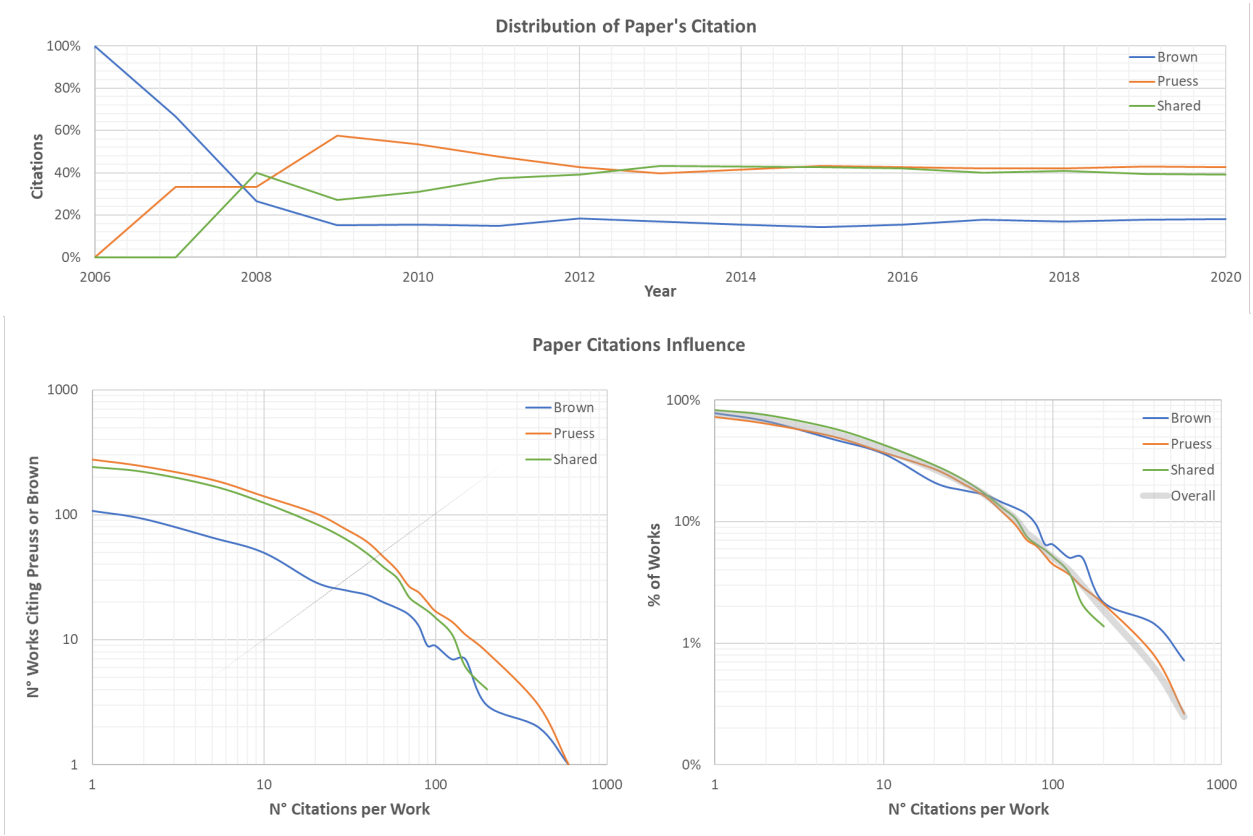

Figure 1.5: Analysis of the literature citing Brown of Pruess: *Top*, Distribution of work citing Brown only, Pruess only, or both trough-out the years *Down-Left*, *h-graph* of the collection of papers. *Down-Right*, Graph displaying the same distribution in relative terms (percentage of papers with more than a specific number of citations).

Some of these publications have been relatively influential, with the papers citing Pruess or both Pruess and Brown receiving in general more citation. In 2022, the *H-index* of the collection of papers was 23 for the papers citing Brown only, 58 for the papers citing Pruess only, and 53 the papers citing both.
The disparity depicted in the *"h-graph"* doesn't necessarily imply that the works citing only Brown are of lower quality. On the contrary, this is more likely an evidence of the fact that these two groups of papers, i.e., those citing only Brown and those citing only Pruess, *might not be cross-referencing each other*. In simpler terms, papers citing only Brown are unlikely to cite papers that exclusively reference Pruess, and vice versa. This situation might arise from a *lack of awareness about the*

existence of the other set of papers. Consequently, papers citing only Brown might have a smaller *"citation pool"*, which could give the impression of lower influence, but this doesn't necessarily reflect the quality of the work. This can be proven by looking at the relative version of the *"h-graph"* (down-right in *Fig 1.5*) in which the curves for the three groups overlaps.
Among the numerous researchers who have significantly contributed to this field, we will conclude this historical section by spotlighting the work of three groups of researchers who have made substantial and relevant contributions. We will focus our attention on their influential work closely related to the topic of this thesis. This is not intended to be an exhaustive collection of contributions from recent years, but rather a starting point for the subsequent state-of-the-art analysis.
The contribution of the three groups have been summarized in *Fig 1.6*.

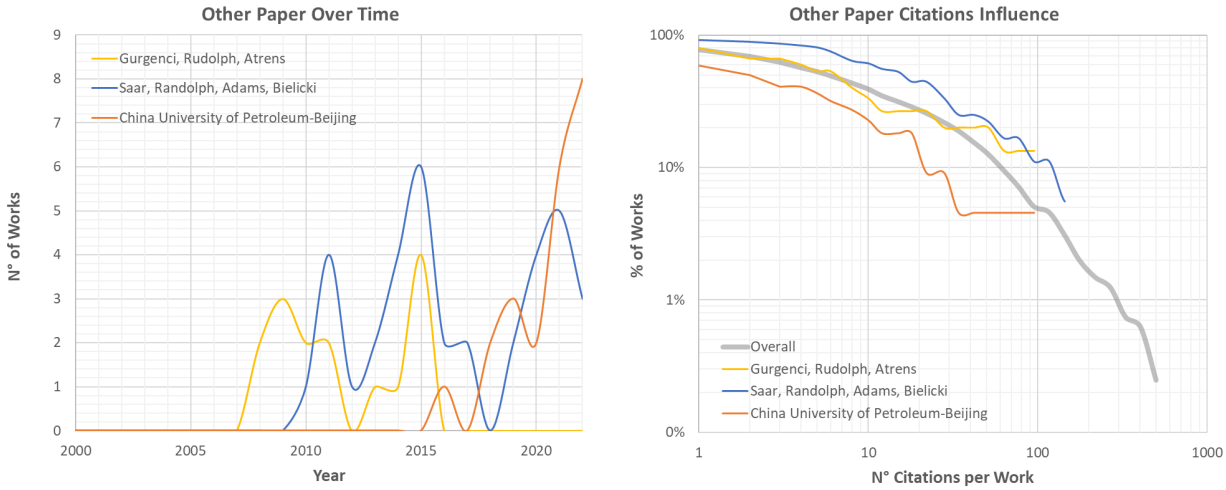

Figure 1.6: Analysis of the influence in literature by the papers published by other research groups: *Left*, number of publication per year. *Right*, relative "h-graph" compared with the overall publication for the works citing Brown or Pruess

H. Gurgenci, V. Rudolph, and A. Atrens

The first to build upon Pruess's work was a research group from the *Geothermal Energy Centre of Excellence* of the *University of Queensland*, Australia, composed mainly of H. Gurgenci, V. Rudolph, and A. Atrens. They collectively publish 15 works between 2008 and 2015 citing both Pruess and Brown.
Among the others, their most influential works was two publications, presented in 2009 and 2010, introducing for the first time the possibility of directly expanding the working fluid instead of using the thermosiphon effect for circulating the fluid in the reservoir [62], [63]. Their work mainly focus on the thermodynamic [62], [63] and thermo-economic [64] optimizations of CO_2 -based EGS. As can be seen from *Fig 1.6*, their interest in the field decrease after 2015.

M. Saar, J. Randolph, B. Adams, J. Bielicki et Al.

Another pivotal contributor in the field is the research group associated with J. Randolph and M. Saar at the time researchers at *the University of Minnesota*.
In 2011, they first published two papers [65], [66] introducing for the first time the concept of CPG, the injection of CO_2 into natural high-permeable reservoirs with the goal of both increasing the

power production and the CO_2 sequestration, proving the appeal of the concept for the development of which they also co-founded a startup *TerraCOH*.
In the following years they collaborated with many other researcher in the analysis of this technology. Together with B. Adams, at the time a PhD student at *the University of Minnesota* co-supervised by Prof. Saar [67], they published high quality thermodynamic analysis of the behaviour of the system and of the surface equipment [68], [69].
At the same time with other PhD students, N. Garapati and B. Tutolo, they analyze the complex geological interaction between the CO_2 and the water already existing in the reservoir [70], and perform some experimental analysis of the mineralization of CO_2 in the reservoir [71], [72].
The collaboration has also included prof. J. Bielicki from the *Ohio State University*, who coauthored most of the published papers.
This collaborative effort, that continue until now [73], [74], has led to the production of high-quality publications, analyzing also different geothermal system than the CPG [75], earning recognition within the scientific community, as reflected in the *h-graph* presented in *Fig 1.6*.

China University of Petroleum-Beijing

In 2018, a group of four researchers from the *China University of Petroleum-Beijing*, F. Sun, Y. Yao, G. Li and X. Li, initiated research in the field of utilizing CO_2 in closed-loop wells. The three papers that they published that year, investigated the application of CO_2 in both U-shaped wells [76] and horizontal wells with a coaxial geometry [77], [78], laying the foundation for further studies in this area (these tree papers have collectively gathered almost 300 citations).
Almost at the same time, another group of the same institution have published the results of an experimental campaign on a vertical coaxial closed loop system [79] publishing very interesting results.

1.2.2 State of the Art

System Modelling

In recent years, numerous researchers have examined various surface power plant configurations to optimize the conversion of energy derived from the well. Schifflechner et al. [80] compared the expected power production of a direct expansion CO_2 plant with a traditional water-based ORC system. On the other hand, Gładysz et al. [81] optimized the direct expansion configuration for a proposed CO_2 bases EGS in Poland. This latter study was expanded upon by Tagliaferri et al. [82] to identify the optimal position of the heat exchanger for heat production in a Combined Heat and Power (CHP) configuration.
Regarding closed-loop systems, the most recent study was pubblished in 2022 by Malek et al. [75]. This study is an extensive thermo-economic analysis of what the authors called an *Advanced Geothermal System (AGS)*. In this system, the working fluid is heated up while circulating in 4, 5km-long u-shaped horizontal wells. The study again compared the use of water as a heat carrier with an ORC for power production, along with the direct-expansion CO_2 case.
In all of this most recent studies, the model of the geothermal system is quite simplified, avoiding to deal to much with the geological description of the reservoir. For open-systems, such as the one described by Schifflechner or Gładysz, the geothermal system model has been based on the

model proposed by Adams in 2015 [69], which apparently has become a standard in these kind of simulations.
To conclude, it is worth mentioning the remarkable *generalizable GEOthermal techno-economic simulator (genGEO)*, a tool recently published by Adams et al. [73] that consists of five different models for performing techno-economic analyses on geothermal systems. The most interesting part of the tool is the advanced economic correlation that have been developed for the estimation of cost for well drilling in different conditions.
Regarding cost correlations, in 2019 a group of researcher from the Department of Energy (DOE) National Laboratories, have published a paper presenting the cost correlations for sCO_2 components that they have developed starting from the significant pool of vendor that they have contact with. [83] These correlations are very useful in estimating the investment cost of CO_2 based surface power plant.

Experimental Activities

Up to 2022 the only operational test of a CO_2 based EGS was performend in 2015 in Cranfield, at the SECARB test site [84]. The test was a failure as it was not able to initiate a self sustainable thermosiphon circulation. Adams et al. have analyzed the results [74] concluding that a natural circulation was not possible in such circumstances but that heat extraction could anyway be achieved trough CO_2 pumping.

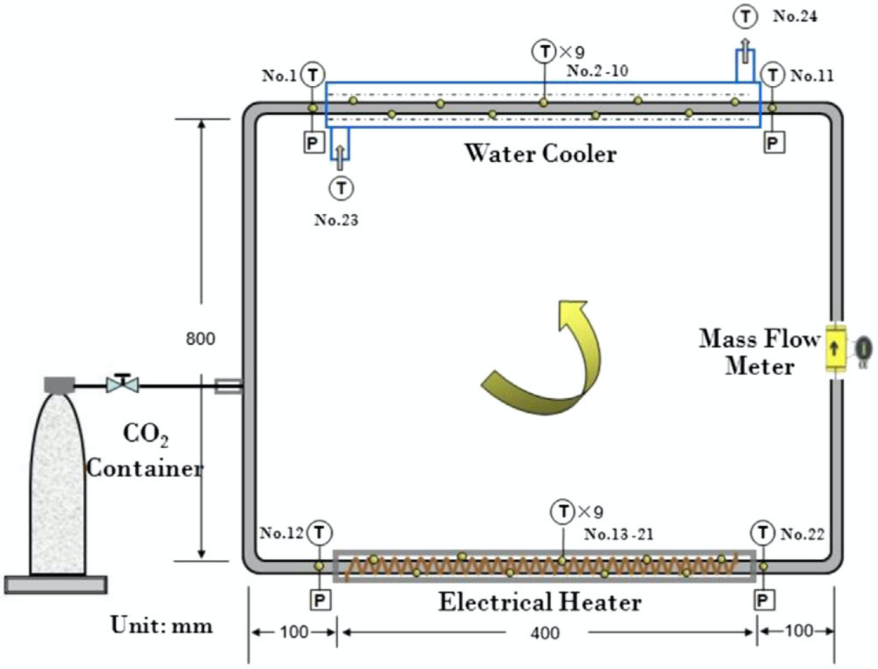

Figure 1.7: Scheme of the experimental apparatus developed by Chen et al.
Image from Chen et al. (2013) [85]

On lab scale, many small scale experimental activities has been performed to study different aspects of the CO_2 behaviour in geothermal systems. The first was an experiment conducted by L. Chen, B. Deng and X. Zhang form the Peking University in Beijing in 2013 using a square loop depicted in *Fig 1.7* to asses the feasibility and the stability of the natural thermosyphon circulation [85].

The same experimental setup has been used by L.R. Thippeswamy and A. Kumar Yadav to compare experimentally the water and CO_2 based circulation loops [86].
On the other hand, other researcher have used more traditional test benches to evaluate heat transfer behaviour of CO_2 in different conditions [87].

References

[1] J. H. Davies and D. R. Davies, "Solid Earth Earth's surface heat flux," Tech. Rep., 2010, pp. 5–24. [Online]. Available: www.solid-earth.net/1/5/2010/.

[2] EnerData, "World Energy & Climate Statistics – Yearbook 2023," Tech. Rep., 2023. [Online]. Available: https://yearbook.enerdata.net/total-energy/world-consumption-statistics.html.

[3] P. Driscoll and D. Bercovici, "On the thermal and magnetic histories of Earth and Venus: Influences of melting, radioactivity, and conductivity," *Physics of the Earth and Planetary Interiors*, vol. 236, pp. 36–51, Nov. 2014, ISSN: 00319201. DOI: 10.1016/j.pepi.2014.08.004.

[4] UGI (Unione Geotermica Italiana), *Geothermal Energy Yesterday, Today, Tomorrow*, 2007. [Online]. Available: http://www.unionegeotermica.it/la-geotermia-ieri-oggi-domani/.

[5] J. W. Lund and A. N. Toth, "Direct utilization of geothermal energy 2020 worldwide review," *Geothermics*, vol. 90, p. 101 915, Feb. 2021, ISSN: 03756505. DOI: 10.1016/j.geothermics.2020.101915.

[6] Á. Ragnarsson, B. Steingrímsson, and S. Thorhallsson, "Geothermal development in Iceland 2015-2019," in *Proceedings World Geothermal Congress*, vol. 1, 2020.

[7] P. Conti, W. Grassi, G. Passaleva, and R. Cataldi, "Geothermal Direct Uses in Italy: Country Update for WGC2015," in *Proceedings of the World Geothermal Congress*, 2015, pp. 1–10.

[8] R. DiPippo, "Geothermal power plants: Evolution and performance assessments," *Geothermics*, vol. 53, pp. 291–307, 2015, ISSN: 03756505. DOI: 10.1016/j.geothermics.2014.07.005.

[9] R. DiPippo, *Geothermal power plants: principles, applications, case studies and environmental impact*. Butterworth-Heinemann, 2012, ISBN: 0123947871.

[10] R. Parri, "La Nascita della Prima Central Geotermica," *Associazione Nazionale Dipendenti e Pensionati Gruppo Enel, Lettera ai Soci, Numero Speciale (in Italian)*, 2013.

[11] P. Ungar, Z. Özcan, G. Manfrida, Ö. Ekici, and L. Talluri, "Off-Design Modelling of ORC Turbines for Geothermal Application," *E3S Web of Conferences*, vol. 312, p. 11 015, 2021. DOI: 10.1051/e3sconf/202131211015.

[12] P. H. Niknam, L. Talluri, D. Fiaschi, and G. Manfrida, "Sensitivity analysis and dynamic modelling of the reinjection process in a binary cycle geothermal power plant of Larderello area," *Energy*, vol. 214, Jan. 2021, ISSN: 03605442. DOI: 10.1016/j.energy.2020.118869.

[13] G. Manfrida, L. Talluri, P. Ungar, *et al.*, "Exergo-economic and exergo-environmental assessment of two large CHP geothermal power plants," *Geothermics*, vol. 113, Sep. 2023, ISSN: 03756505. DOI: 10.1016/j.geothermics.2023.102758.

[14] G. Buonasorte, R. Cataldi, and G. Passaleva, "Geothermal development in Italy: from present to future," in *Proceedings European Geothermal Congress*, Unterhaching, Germany, May 2007.

[15] N. Ferrara, R. Basosi, and M. L. Parisi, "Data analysis of atmospheric emission from geothermal power plants in Italy," *Data in Brief*, vol. 25, p. 104 339, Aug. 2019, ISSN: 23523409. DOI: 10.1016/j.dib.2019.104339.

[16] M. R. Castro, D. L. López, J. A. Reyes-López, *et al.*, "Modeling scaling of silica from reinfection waters at well head conditions in the Berlin Geothermal field, El Salvador, Central America," in *Thirty-First Workshop on Geothermal Reservoir Engineering*, 2006.

[17] B. Sigfusson, I. Gunnarsson, and R. Energy Baejarhalsi, "Scaling prevention experiments in the Hellisheidi power plant, Iceland," in *Thirty-Sixth Workshop on Geothermal Reservoir Engineering*, 2011.

[18] E. Gunnlaugsson, H. Ármannsson, S. Thorhallsson, and B. Steingrímsson, "Problems in geothermal operation - scaling and corrosion," in *Goethermal Training Program, United Nations University*, 2014.

[19] S. N. Karlsdóttir, S. M. Hjaltason, and K. R. Ragnarsdóttir, "Corrosion behavior of materials in hydrogen sulfide abatement system at Hellisheiði geothermal power plant," *Geothermics*, vol. 70, pp. 222–229, Nov. 2017, ISSN: 03756505. DOI: 10.1016/j.geothermics.2017.06.010.

[20] A. Baldacci, M. Mannari, and F. Sansone, "Greening of geothermal power. An innovative technology for abatement of hydrogen sulphide and mercury emission," in *Proceedings of World Geothermal Congress 2005*, Jan. 2005, pp. 24–29.

[21] B. Sigfusson and A. Uihlein, *2014 JRC Geothermal Energy Status Report*. 2015, p. 64, ISBN: 9789279446146. DOI: 10.2790/460251. [Online]. Available: http://publications.jrc.ec.europa.eu/repository/handle/JRC93338.

[22] J. van Wees, T. Boxem, L. Angelino, and P. Dumas, "A prospective study on the geothermal potential in the EU," Deliverable n° 2.5 - GeoElec Project, Tech. Rep., 2013. [Online]. Available: http://www.geoelec.eu/wp-content/uploads/2011/09/D-2.5-GEOELEC-prospective-study.pdf.

[23] U.S. Energy Information Administration (EIA), "Cost and Performance Characteristics of New Generating Technologies, Annual Energy Outlook 2022," Tech. Rep., 2022. [Online]. Available: https://www.eia.gov/outlooks/aeo/assumptions/pdf/table_8.2.pdf.

[24] Q. Lei, H. Wang, and W. Wei, "Potential analysis on exploration of geothermal resources in oil and gas fields," *Natural Gas Industry*, vol. 28, pp. 127–129, Jan. 2008.

[25] X. Bu, W. Ma, and H. Li, "Geothermal energy production utilizing abandoned oil and gas wells," *Renewable Energy*, vol. 41, pp. 80–85, May 2012, ISSN: 09601481. DOI: 10.1016/j.renene.2011.10.009.

[26] E. Miranda-Barbosa, B. Sigfússon, J. Carlsson, and E. Tzimas, "Advantages from Combining CCS with Geothermal Energy," *Energy Procedia*, vol. 114, pp. 6666–6676, Jul. 2017, ISSN: 18766102. DOI: 10.1016/j.egypro.2017.03.1794.

[27] M. X. Li, L. P. Ricard, J. Underschultz, and B. M. Freifeld, "Reducing operational costs of CO2 sequestration through geothermal energy integration," *International Journal of Greenhouse Gas Control*, vol. 44, pp. 238–248, Jan. 2016, ISSN: 17505836. DOI: 10.1016/j.ijggc.2015.11.012.

[28] D. Fiaschi, A. Lifshitz, G. Manfrida, and D. Tempesti, "An innovative ORC power plant layout for heat and power generation from medium- to low-temperature geothermal resources," *Energy Conversion and Management*, vol. 88, pp. 883–893, Dec. 2014, ISSN: 01968904. DOI: 10.1016/j.enconman.2014.08.058. [Online]. Available: https://linkinghub.elsevier.com/retrieve/pii/S0196890414007821.

[29] R. Wüstenhagen, M. Wolsink, and M. J. Bürer, "Social acceptance of renewable energy innovation: An introduction to the concept," *Energy Policy*, vol. 35, no. 5, pp. 2683–2691, May 2007, ISSN: 03014215. DOI: 10.1016/j.enpol.2006.12.001.

[30] M. Segreto, L. Principe, A. Desormeaux, *et al.*, "Trends in Social Acceptance of Renewable Energy Across Europe—A Literature Review," *International Journal of Environmental Research and Public Health*, vol. 17, no. 24, p. 9161, Dec. 2020, ISSN: 1660-4601. DOI: 10.3390/ijerph17249161.

[31] A.-M. Dowd, N. Boughen, P. Ashworth, and S. Carr-Cornish, "Geothermal technology in Australia: Investigating social acceptance," *Energy policy*, vol. 39, no. 10, pp. 6301–6307, 2011, ISSN: 0301-4215.

[32] A. Pellizzone, A. Allansdottir, R. De Franco, G. Muttoni, and A. Manzella, "Social acceptance of geothermal energy in southern Italy," in *Proceedings world geothermal congress*, 2015.

[33] S. V. Payera, "Understanding social acceptance of geothermal energy: Case study for Araucanía region, Chile," *Geothermics*, vol. 72, pp. 138–144, 2018, ISSN: 0375-6505.

[34] E. Gaucher, M. Schoenball, O. Heidbach, *et al.*, "Induced seismicity in geothermal reservoirs: A review of forecasting approaches," *Renewable and Sustainable Energy Reviews*, vol. 52, pp. 1473–1490, 2015, ISSN: 1364-0321.

[35] L. Buijze, L. van Bijsterveldt, H. Cremer, *et al.*, "Review of induced seismicity in geothermal systems worldwide and implications for geothermal systems in the Netherlands," *Netherlands Journal of Geosciences*, vol. 98, e13, Feb. 2019, ISSN: 0016-7746. DOI: 10.1017/njg.2019.6.

[36] V. Maurer, E. Gaucher, M. Grunberg, R. Koepke, R. Pestourie, and N. Cuenot, "Seismicity induced during the development of the Rittershoffen geothermal field, France," *Geothermal Energy*, vol. 8, pp. 1–31, 2020.

[37] D. Brown, "A Hot Dry Rock Geothermal Energy Concept Utilizing Supercritical CO2 Instead of Water," *Twenty-Fifth Workshop on Geothermal Resevoir Engineering*, 2000, ISSN: 2195-9706.

[38] C. A. Clark, *Obituary: Donald Weber Brown Oct. 20, 1931 – Dec. 24, 2017*, Dec. 2017. [Online]. Available: https://ladailypost.com/obituary-donald-weber-brown-oct-20-1931-dec-24-2017/.

[39] Z. Dash, H. Murphy, R. Aamodt, *et al.*, "Hot dry rock geothermal reservoir testing: 1978 to 1980," *Journal of Volcanology and Geothermal Research*, vol. 15, no. 1-3, pp. 59–99, Jan. 1983, ISSN: 03770273. DOI: 10.1016/0377-0273(83)90096-3.

[40] D. Brown, "The US Hot Dry Rock Program-20 Years of Experience in Reservoir Testing," in *Proc. World Geothermal Congress*, Florence, Italy, 1995, pp. 2607–2611.

[41] D. W. Brown, "Evidence for the existance for a stable, highly fluid-pressurized region of deep, jointed crystalline rock from Fenton Hill Hot Dry Rock test data," in *Twenty-Fourth Workshop on Geothermal Reservoir Engineering*, Stanford, California, 1999.

[42] K. Pruess, C. Oldenburg, and G. Moridis, "TOUGH2 USER'S GUIDE, VERSION 2," Tech. Rep., 1999.

[43] K. Pruess and B. Kennedy, "Modeling of phase-partitioning tracers in fractured reservoirs," in *Twenty-Fifth Workshop on Geothermal Resevoir Engineering*, 2000.

[44] M. J. Lippmann, A. H. Truesdell, and K. Pruess, "The control of fault H on the hydrology of the Cerro Prieto III area," in *Twenty-Fifth Workshop on Geothermal Resevoir Engineering*, 2000.

[45] A. Kiryukhin, K. Pruess, K. Maltseva, I. Delemen, and Y. Tishenko, "Modeling studies of the Paratunsky geothermal field, Kamchatka, Russia," in *Twenty-Fifth Workshop on Geothermal Resevoir Engineering*, 2000.

[46] C. M. Oldenburg and K. Pruess, "Thermohaline convective mixing at a brine interface," in *Twenty-Fifth Workshop on Geothermal Resevoir Engineering*, 2000.

[47] M. Trew, M. O'sullivan, C. Harvey, E. Anderson, and K. Pruess, "Computer modelling of gas and liquid tracers in geothermal reservoirs," in *Twenty-Fifth Workshop on Geothermal Resevoir Engineering*, 2000.

[48] J. E. Garcia, "Fluid Dynamics of Carbon Dioxide Disposal into Saline Aquifers," Ph.D. dissertation, Lawrence Berkeley National Laboratory (LBNL), Berkeley, CA (United States), Jan. 2003. DOI: 10.2172/821335.

[49] K. Pruess, "Enhanced geothermal systems (EGS) using CO2 as working fluid - A novel approach for generating renewable energy with simultaneous sequestration of carbon," *Geothermics*, vol. 35, no. 4, pp. 351–367, Aug. 2006, ISSN: 03756505. DOI: 10.1016/j.geothermics.2006.08.002.

[50] K. Pruess and M. Azaroual, "On the feasibility of using supercritical CO2 as heay transmission fluid in an engineered Hot Dry Rock geothermal system," in *PROCEEDINGS, Thirty-First Workshop on Geothermal Reservoir Engineering*, Stanford, California, Jan. 2006.

[51] M. Magliocco, T. J. Kneafsey, K. Pruess, and S. Glaser, "Laboratory experimental study of heat extraction from porous media by means of CO2," in *PROCEEDINGS, Thirty-Sixth Workshop on Geothermal Reservoir Engineering*, Stanford, California, Jan. 2011.

[52] A. Borgia, K. Pruess, T. J. Kneafsey, C. M. Oldenburg, and L. Pan, "Numerical simulation of salt precipitation in the fractures of a CO2-enhanced geothermal system," *Geothermics*, vol. 44, pp. 13–22, Oct. 2012, ISSN: 03756505. DOI: 10.1016/j.geothermics.2012.06.002. [Online]. Available: https://linkinghub.elsevier.com/retrieve/pii/S0375650512000363.

[53] K. Pruess, "Enhanced Geothermal Systems (EGS) comparing water with CO2 as heat transmission fluids," Lawrence Berkeley National Laboratory, Tech. Rep., 2007.

[54] K. Pruess, "On production behavior of enhanced geothermal systems with CO2 as working fluid," *Energy Conversion and Management*, vol. 49, no. 6, pp. 1446–1454, Jun. 2008, ISSN: 01968904. DOI: 10.1016/j.enconman.2007.12.029.

[55] K. Pruess, "Role of Fluid Pressure in the Production Behavior of Enhanced Geothermal Systems with CO2 as Working Fluid," Lawrence Berkeley National Laboratory, Tech. Rep., May 2008. [Online]. Available: https://escholarship.org/uc/item/7rr249rc.

[56] K. Pruess and N. Spycher, "Enhanced Geothermal Systems (EGS) with CO2 as Heat Transmission Fluid - A Scheme for Combining Recovery of Renewable Energy with Geologic Storage of CO2," Lawrence Berkeley National Laboratory, Tech. Rep., 2009.

[57] N. Spycher and K. Pruess, "A Phase-partitioning model for CO2-brine mixtures at elevated temperatures and pressures: Application to CO2-enhanced geothermal systems," *Transport in Porous Media*, vol. 82, no. 1, pp. 173–196, Feb. 2010, ISSN: 01693913. DOI: 10.1007/s11242-009-9425-y.

[58] T. Xu and K. Pruess, "Reactive Transport Modeling to Study Fluid-Rock Interactions in Enhanced Geothermal Systems (EGS) with CO2 as Working Fluid," in *Proceedings World Geothermal Congress*, Bali, Indonesia, Apr. 2010.

[59] J. Apps and K. Pruess, "Modeling geochemical processes in enhanced geothermal systems with CO2 as heat transfer fluid," in *Thirty-Sixth Workshop on Geothermal Reservoir Engineering*, Stanford, California, Jan. 2011. [Online]. Available: https://www.researchgate.net/publication/228707224.

[60] N. Spycher and K. Pruess, "A model for thermophysical properties of CO2-brine mixtures at elevated temperatures and pressures," in *Thirty-Sixth Workshop on Geothermal Reservoir Engineering*, Stanford, California, Jan. 2011.

[61] Y. Wan, T. Xu, and K. Pruess, "Impact of fluid-rock interactions on enhanced geothermal systems with CO2 as heat transmission fluid," in *Thirty-Sixth Workshop on Geothermal Reservoir Engineering*, Stanford, California, Jan. 2011.

[62] A. D. Atrens, H. Gurgenci, and V. Rudolph, "CO2 Thermosiphon for Competitive Geothermal Power Generation," *Energy & Fuels*, vol. 23, no. 1, pp. 553–557, Jan. 2009, ISSN: 0887-0624. DOI: 10.1021/ef800601z.

[63] A. D. Atrens, H. Gurgenci, and V. Rudolph, "Electricity generation using a carbon-dioxide thermosiphon," *Geothermics*, vol. 39, no. 2, pp. 161–169, Jun. 2010, ISSN: 03756505. DOI: 10.1016/j.geothermics.2010.03.001.

[64] A. D. Atrens, H. Gurgenci, and V. Rudolph, "Economic Optimization of a CO2-Based EGS Power Plant," *Energy & Fuels*, vol. 25, no. 8, pp. 3765–3775, Aug. 2011, ISSN: 0887-0624. DOI: 10.1021/ef200537n.

[65] J. B. Randolph and M. O. Saar, "Combining geothermal energy capture with geologic carbon dioxide sequestration," *Geophysical Research Letters*, vol. 38, no. 10, 2011, ISSN: 0094-8276.

[66] J. B. Randolph and M. O. Saar, "Coupling carbon dioxide sequestration with geothermal energy capture in naturally permeable, porous geologic formations: Implications for CO2 sequestration," in *Energy Procedia*, vol. 4, Elsevier Ltd, 2011, pp. 2206–2213. DOI: 10.1016/j.egypro.2011.02.108.

[67] B. M. Adams, "On the Power Performance and Integration of Carbon-dioxide Plume Geothermal (CPG) Electrical Energy Production," Ph.D. dissertation, 2015.

[68] B. M. Adams, T. H. Kuehn, J. M. Bielicki, J. B. Randolph, and M. O. Saar, "On the importance of the thermosiphon effect in CPG (CO2 plume geothermal) power systems," *Energy*, vol. 69, pp. 409–418, May 2014, ISSN: 03605442. DOI: 10.1016/j.energy.2014.03.032.

[69] B. M. Adams, T. H. Kuehn, J. M. Bielicki, J. B. Randolph, and M. O. Saar, "A comparison of electric power output of CO2 Plume Geothermal (CPG) and brine geothermal systems for varying reservoir conditions," *Applied Energy*, vol. 140, pp. 365–377, Feb. 2015, ISSN: 03062619. DOI: 10.1016/j.apenergy.2014.11.043.

[70] N. Garapati, J. B. Randolph, and M. O. Saar, "Brine displacement by CO2, energy extraction rates, and lifespan of a CO2-limited CO2-Plume Geothermal (CPG) system with a horizontal production well," *Geothermics*, vol. 55, pp. 182–194, May 2015, ISSN: 03756505. DOI: 10.1016/j.geothermics.2015.02.005.

[71] B. M. Tutolo, "Carbon Dioxide Sequestration in Sedimentary Reservoirs: Fundamental and Applied Considerations," Ph.D. dissertation, 2015.

[72] B. M. Tutolo, A. J. Luhmann, X. Z. Kong, M. O. Saar, and W. E. Seyfried, "CO2 sequestration in feldspar-rich sandstone: Coupled evolution of fluid chemistry, mineral reaction rates, and hydrogeochemical properties," *Geochimica et Cosmochimica Acta*, vol. 160, pp. 132–154, Jul. 2015, ISSN: 00167037. DOI: 10.1016/j.gca.2015.04.002.

[73] B. M. Adams, J. Ogland-Hand, J. Bielicki, P. Schädle, and M. Saar, "Estimating the Geothermal Electricity Generation Potential of Sedimentary Basins Using genGEO (the generalizable GEOthermal techno-economic simulator)," *ChemRxiv Preprint*, 2021.

[74] B. M. Adams, M. R. Fleming, J. M. Bielicki, N. Garapati, and M. O. Saar, "An Analysis of the Demonstration of a CO2-based Thermosiphon at the SECARB Cranfield Site," in *46th Workshop on Geothermal Reservoir Engineering Stanford University*, vol. 46, Stanford University, Stanford, California, 2021. DOI: https://doi.org/10.3929/ethz-b-000467171.

[75] A. E. Malek, B. M. Adams, E. Rossi, H. O. Schiegg, and M. O. Saar, "Techno-economic analysis of Advanced Geothermal Systems (AGS)," *Renewable Energy*, vol. 186, pp. 927–943, 2022, ISSN: 09601481. DOI: 10.1016/j.renene.2022.01.012.

[76] F. Sun, Y. Yao, G. Li, and X. Li, "Geothermal energy development by circulating CO2 in a U-shaped closed loop geothermal system," *Energy Conversion and Management*, vol. 174, pp. 971–982, Oct. 2018, ISSN: 01968904. DOI: 10.1016/j.enconman.2018.08.094.

[77] F. Sun, Y. Yao, G. Li, and X. Li, "Performance of geothermal energy extraction in a horizontal well by using CO2 as the working fluid," *Energy Conversion and Management*, vol. 171, pp. 1529–1539, Sep. 2018, ISSN: 01968904. DOI: 10.1016/j.enconman.2018.06.092.

[78] F. Sun, Y. Yao, G. Li, and X. Li, "Geothermal energy extraction in CO2 rich basin using abandoned horizontal wells," *Energy*, vol. 158, pp. 760–773, Sep. 2018, ISSN: 03605442. DOI: 10.1016/j.energy.2018.06.084.

[79] Y. Zhang, C. Yu, G. Li, *et al.*, "Performance analysis of a downhole coaxial heat exchanger geothermal system with various working fluids," *Applied Thermal Engineering*, vol. 163, Dec. 2019, ISSN: 13594311. DOI: 10.1016/j.applthermaleng.2019.114317.

[80] C. Schifflechner, F. Dawo, S. Eyerer, C. Wieland, and H. Spliethoff, "Thermodynamic comparison of direct supercritical CO2 and indirect brine-ORC concepts for geothermal combined heat and power generation," *Renewable Energy*, vol. 161, pp. 1292–1302, 2020, ISSN: 18790682. DOI: 10.1016/j.renene.2020.07.044.

[81] P. Gładysz, A. Sowiżdżał, M. Miecznik, and L. Pajak, "Carbon dioxide-enhanced geothermal systems for heat and electricity production: Energy and economic analyses for central Poland," *Energy Conversion and Management*, vol. 220, Sep. 2020, ISSN: 01968904. DOI: 10.1016/j.enconman.2020.113142.

[82] M. Tagliaferri, P. Gładysz, P. Ungar, *et al.*, "Techno-Economic Assessment of the Supercritical Carbon Dioxide Enhanced Geothermal Systems," *Sustainability*, vol. 14, no. 24, p. 16 580, Dec. 2022, ISSN: 2071-1050. DOI: 10.3390/su142416580.

[83] N. T. Weiland, B. W. Lance, and S. R. Pidaparti, "sCO2 Power Cycle Component Cost Correlations From DOE Data Spanning Multiple Scales and Applications," in *ASME Turbo Expo 2019: Turbomachinery Technical Conference and Exposition*, Phoenix, Arizona, USA: American Society of Mechanical Engineers, Jun. 2019, ISBN: 978-0-7918-5872-1. DOI: 10.1115/GT2019-90493.

[84] L. Pan, C. Doughty, and B. Freifeld, "How to sustain a CO2-thermosiphon in a partially saturated geothermal reservoir: Lessons learned from field experiment and numerical modeling," *Geothermics*, vol. 71, pp. 274–293, Jan. 2018, ISSN: 03756505. DOI: 10.1016/j.geothermics.2017.10.004.

[85] L. Chen, B. L. Deng, and X. R. Zhang, "Experimental study of trans-critical and supercritical CO2 natural circulation flow in a closed loop," *Applied Thermal Engineering*, vol. 59, no. 1-2, pp. 1–13, 2013, ISSN: 13594311. DOI: 10.1016/j.applthermaleng.2013.05.017.

[86] L. R. Thippeswamy and A. Kumar Yadav, "Heat transfer enhancement using CO2 in a natural circulation loop," *Scientific Reports*, vol. 10, no. 1, Dec. 2020, ISSN: 20452322. DOI: 10.1038/s41598-020-58432-6.

[87] J. Chen, S.-G. Yang, R. Zhao, and W.-L. Cheng, "Experimental study on the effect of wall roughness on heat transfer characteristics of supercritical carbon dioxide in vertical tubes," *International Journal of Heat and Mass Transfer*, vol. 196, p. 123 258, Nov. 2022, ISSN: 00179310. DOI: 10.1016/j.ijheatmasstransfer.2022.123258.

Chapter 2

Theoretical Analysis

2.1 Introduction

Geothermal energy is of extreme interest for the decarbonization of the energetic sector as it is both renewable and dispatchable. According to Thomsen's research [1], which focuses on the Californian energy market, these features make geothermal power production competitive with photovoltaic systems, even when the *Levelized Cost of Heat (LCOE)* is in the range of 70-80€/MWh. However, the use of geothermal energy for power generation is currently restricted to areas with a natural aquifer and high geothermal flux, due to technical and economic challenges. To address these challenges, in recent years multiple studies has proposed the usage of sCO_2 as working fluid for geothermal power production, due to its thermodynamics properties.
The first Idea of a CO_2 based system is due to Brown [2] who identify the clear benefit of CO_2 in terms of scaling and pumping power reduction, possible sequestration of the CO_2 in the reservoir, and of the foreseeable natural pressurization of the fluid. Brown's work has been brought to the attention of the scientific community by Pruess [3] who extended it by developing a model of the CO_2 behaviour in the reservoir and refining the rough estimate presented by Brown.
Starting from these two founding works, multiple papers have been published in recent years exploring various aspect of this kind of systems such as estimating the CO_2 sequestration effect [4], [5], analysing different reservoirs and well geometries [6]–[8], surface plant configurations [9]–[13] or possible usages of the extracted heat [12].
Unfortunately, due to the complexity of CO_2 geothermal systems, it is challenging to find a generalized analysis of their characteristics in literature. The amount of possible solutions for heat extraction from the reservoir, coupled with the strong dependence of the geological properties with the selected location, make it difficult to identify universal trends or design principles. Moreover, the multitude of parameters that can be fine-tuned during optimization, make the identification of the most impacting ones a complex task.
The scope of this paper is to simplify the analysis of such systems in order to identify the general trend underlying their behaviour in order to guide the choice of future designers that will have to deal with the complexity of the real implementation.

2.2 General Model Description

2.2.1 Geothermal System Model

In its simplest form a geothermal system can be divided into 3 main sections (as shown in *Fig 2.1*)

- **Descending Section (0-1)**: The fluid is brought from the surface to the reservoir. The pressure increase a result of the change in gravitational potential. Represent the re-injection well of a classical geothermal system or the descending part of a BHE system.
- **Heat Exchange Section (1-2)**: The fluid is heated up by the hot rocks in the reservoir and brought to the production well.
- **Ascending Section (2-3)**: The heated fluid is brought back to the surface to be exploited. The pressure decrease again because of the change in gravitational potential. Represent the production well of a classical geothermal system or the ascending part of a BHE system.

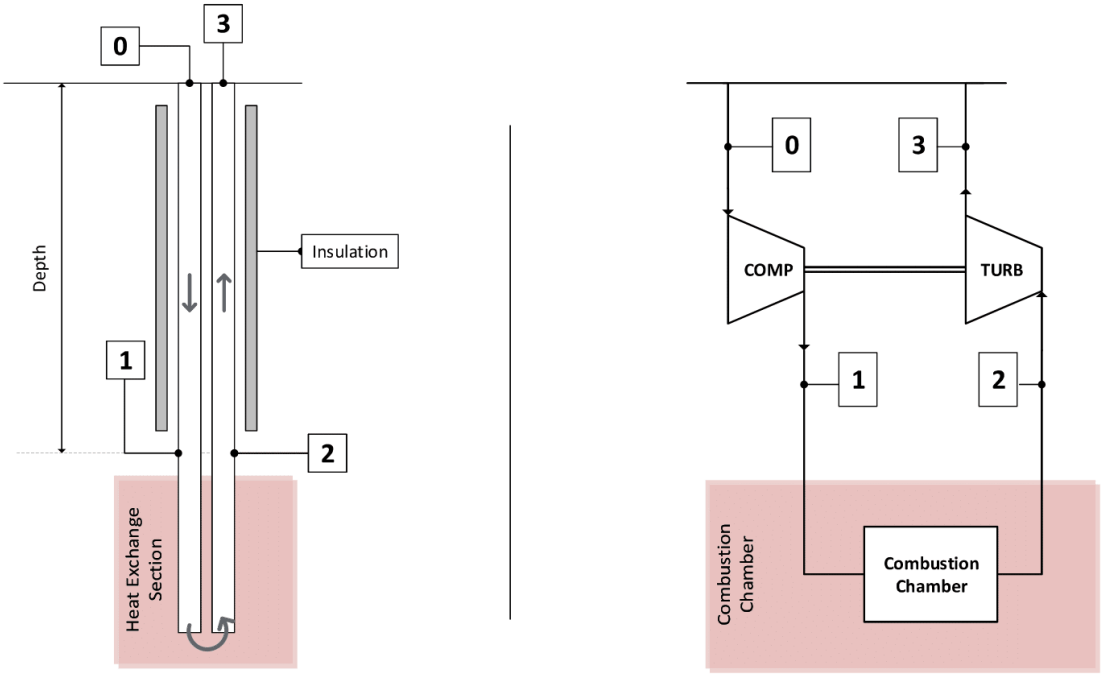

Figure 2.1: Simplified Model Scheme. The scheme itself is equivalent to a Brayton or Rankine cycle (depending on the state of the input) as noted by Adams et Al. [14]

It is important to notice that, as shown in *Fig 2.1*, the thermodynamic cycle of the well is equivalent to a Rankine or a Brayton cycle (depending on the state of the fluid at the inlet). This fact will be very useful in the analysis of the results.

Ascending/Descending section (2-3/0-1)

In order to limit the number of parameter of the model the section has been considered as completely insulated from the surroundings rock and the pressure losses has been neglected.
Given these hypothesis, the pressure increase can be easily determined from the momentum and energy balance equations:

$$dp = -\rho g dz \tag{2.1}$$

$$dh = -g dz \tag{2.2}$$

The kinetic term in both the equations has been neglected in order to eliminate the need for a geometrical description of the well. This assumption is true as long as the velocity remains relatively low in the pipes. The integration of *Eq 2.1* requires the knowledge of the equation of state of the fluid as pressure and density are function of each other. Different equation of states have been considered for different purposes:

- The ideal gas EoS and a simple liquid correlation ($\rho = \text{const.}$) have been employed to obtain an analytic solution, enabling a more profound comprehension of the system's behavior. The derivation of the analytic solution is detailed in Appendix 2.A.
- To describe the behaviour of real fluid in a *qualitative* way, a simple **two-parameter EoS** has been used, as it can roughly approximate the sub-critical, trans-critical and supercritical region of a generic fluid requiring only the critical properties for the fluid definition (because of the principle of corresponding states). The developed model is presented in Appendix 2.C.
- For a *quantitative* analysis, the fluid properties have been retrieved from **REFPROP** [15].

Where an analytic solution is not achievable, the integration of the system of equations has been performed in python using a Runge-Kutta solver [16] (as implemented in the *SciPy* Python package [17]).

Heat Exchange Section (1-2)

Two different models has been developed for the heat exchange section depending on the geothermal system used for heat extraction (*Fig 2.2* should help to clarify the discussion):

- **Open System** (e.g. *CPG* or *Traditions Geothermal systems*): In this kind of systems, the working fluid is injected in an existing reservoir displacing the water that was filling it. The pressure in the reservoir is fixed by the displaced water and, following the approach used by Adams et Al. [14], has considered to be equal to the hydro-static pressure for the selected reservoir depth ($p_{res} = \rho_{water} g \Delta z$). The pressure in Points 1 and 2 (reference to *Fig 2.1*) have been set to the reservoir pressure.
- **Closed System** (e.g. *EGS* or *BHE systems*): In these systems, the working fluid is relatively isolated from natural fluids hence the pressure inside the reservoir can be controlled adjusting the injection pressure. The pressure drop inside the reservoir has been neglected to avoid the need for the definition of the geological parameter in the reservoir.

In both cases, the temperature of Point 2 has been fixed based on the geothermal gradient.
The different behaviour between the two kind of system is due to the effect of the displaced water in the reservoir that acts like a piston allowing the volume of the region in which the working fluid is confined to expand or contract while keeping a constant pressure. This makes the flow rate in the production and re-injection well independent of each other decoupling the input and output

condition of the system. On the other hand, in EGS or BHE systems, the volume in which the working fluid is confined is relatively fixed. For this reason, any imbalances in the flow rate between injection and production well will quickly result in a change in the reservoir pressure that will restore the balance between the flow rates.

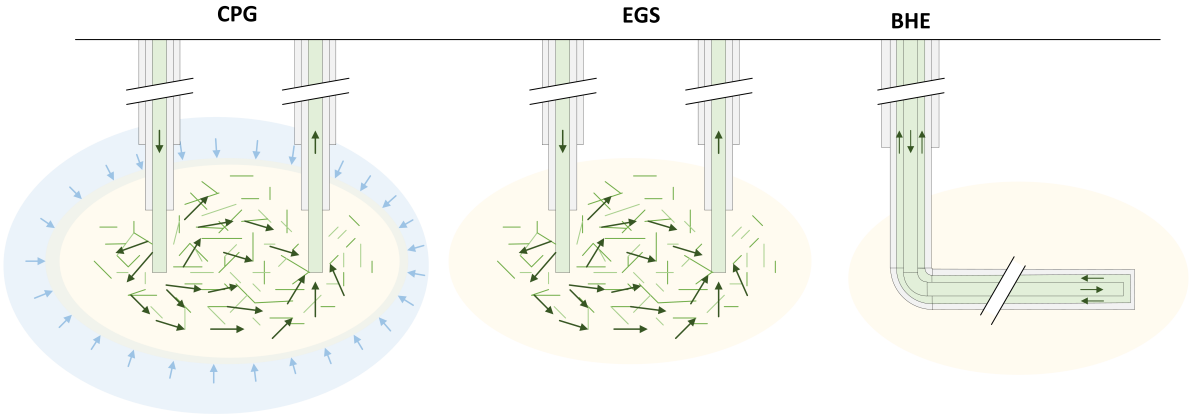

Figure 2.2: Different existing geothermal systems

To conclude, the equations used to describe the different heating sections are summarized in the table below:

Table 2.1: Equations used for the *heating section* modelling

Equation	*Heating Section Type*	
	Open Systems	**Closed Systems**
Pressure (p_2)	$p_2 = \rho_{water} g \Delta z$	$p_2 = p_1$
Temperature (T_2)	$T_2 = T_{amb} + \nabla T_{rocks} \Delta z$	

Where T_{amb} is the ambient temperature and ∇T_{rocks} is the geothermal gradient. It is interesting to notice that the system is capable of extracting heat from the rocks only if the temperature at the inlet of the heating section is lower than the rocks temperature itself.

$$T_1 < T_2 = T_{amb} + \nabla T_{rocks} \Delta z \tag{2.3}$$

This is usually not a problem for liquid based systems but could be a limiting factor for other fluids for which the compression is associated with an increase in temperature.

Remarks on the assumption made: In both cases the assumption made result in a overestimation of the system performances with respect to the real-world scenario. For CPG and EGS systems, the pressure at Point 2 is expected to be lower than the predicted one due to the pressure losses in the reservoir (that can be modelled according to the Darcy's law: $\Delta P = \frac{\mu L}{\rho k A} \dot{m}$ linearly increasing with the flow rate).
On the other hand, for BHE systems, the amount of heat that can be extracted from the reservoir is limited by the heat conduction into the rocks surrounding the well. For this reason usually, increasing the flow rate will result in a decrease of the temperature reached in Point 2.

In both cases, the difference between the model presented and the actual behavior of the system becomes more apparent as the flow rate increases. For this reason, the results presented should be considered as a theoretical maximum performance of the system and have been evaluated relative to the flow rate. The advantage of this kind of analysis is that the results are extremely general, and does not require any knowledge of the geometry of the installation except for the depth of the reservoir.
A model developed for a more detailed analysis is presented in the next chapter.

2.2.2 Surface Plant Configuration

Once the fluid reaches the surface, the extracted energy from the rocks manifests in two distinct forms: pressurization and heat.
In general, different configurations of the surface plant can be used to extract energy from the fluid depending on the reservoir conditions and on the users need. Nevertheless, two limiting condition can be identified (as shown in *Fig 2.3*):

(a) Cooling to input temperature with subsequent expansion to reach input pressure (maximum exergy from heat extraction, minimum exergy from direct expansion)

(b) Expansion to input pressure and cooling to input temperature (minimum exergy from heat extraction, maximum exergy from direct expansion)

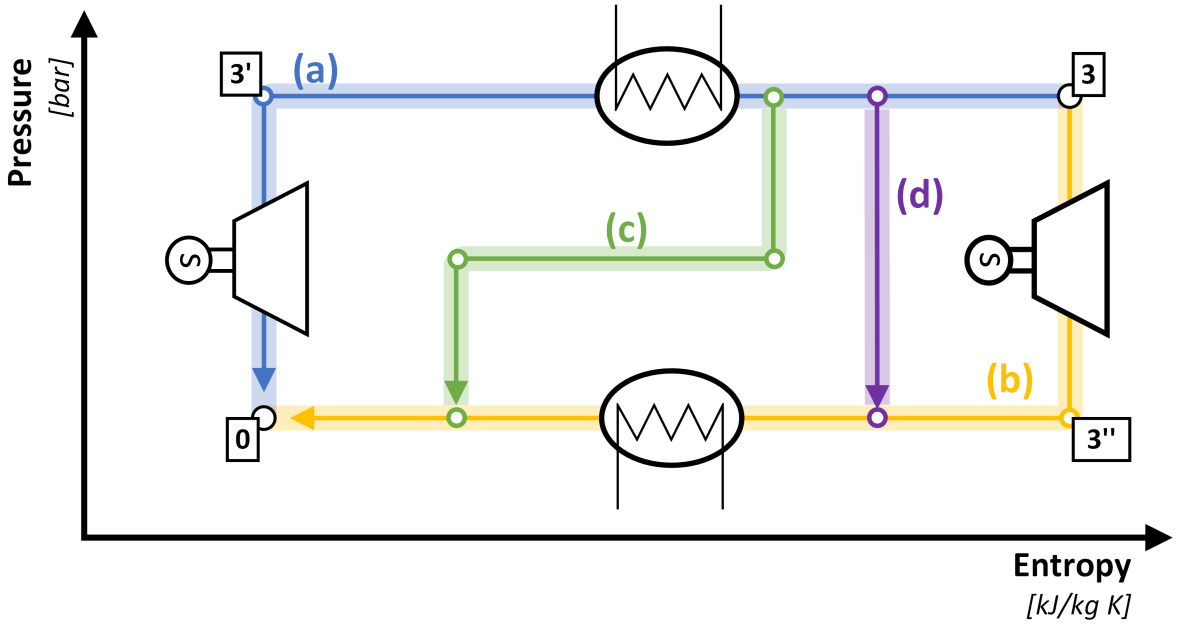

Figure 2.3: Different energy extraction processes: a) heat extraction before expansion, b) expansion before heat extraction, c) and d) alternative solution with alternatives heat transfers and expansions. Points 0 and 3 are the geothermal system inlet and outlet respectively as in *Fig 2.1*.

Other configuration (such as *(c)* and *(d)* in *Fig 2.3*) will result in an exergy extraction from cooling and direct expansion that lies between the two extremes identified before.
To conclude, because of what just stated, the results will be presented in terms of overall specific energy and exergy productions:

$$\dot{w} = \Delta h_{3\to 0} \tag{2.4}$$

$$\dot{e}_x = \Delta h_{3\to 0} - T_{amb}\Delta s_{3\to 0} \tag{2.5}$$

Where the pedex $a \to b$ implies that the difference is evaluated between points a and b (for example $\Delta h_{3\to 0} = h_3 - h_0$), and the points indices refers to *Fig 2.3*.
Another important parameter is the *exergy*, or *second low*, *efficiency* of the system, evaluated as follows:

$$\eta_{e_x} = \frac{\dot{e}_x}{c_f\ \dot{w}} \tag{2.6}$$

where c_f is the Carnot factor relative to the energy extracted from the rock, which has been evaluated as follows:

$$c_f = 1 - \frac{T_{amb}}{T_{rocks}} = 1 - \frac{T_{amb}}{T_{amb} + \nabla T_{rocks}\Delta z} = \frac{\nabla T_{rocks}\Delta z}{T_{amb} + \nabla T_{rocks}\Delta z} \tag{2.7}$$

In addition, the relative amount of energy that can be retrieved using the direct expansion can be identified:

$$[\dot{w}_{dex_{min}},\ \dot{w}_{dex_{max}}] = \left[\frac{\Delta h_{3'\to 0}}{\Delta h_{3\to 0}},\ \frac{\Delta h_{3\to 3''}}{\Delta h_{3\to 0}}\right] \tag{2.8}$$

Remarks on the parameters selection: $\dot{w}$ and $\dot{e}_x$ are crucial parameters in geothermal systems where pressure losses are the primary limiting factors for achievable heat extraction. In these systems, such as the EGS or the CPG, higher flow rates necessitate increased pumping power to overcome system pressure losses, often outweighing the advantages of extracting more power from the well. In such scenarios, having a higher specific heat extraction rate $\dot{w}$ enables more power extraction at the same flow rate, providing a clear advantage.
Conversely, in completely closed systems, like the BHE, overall power extraction is typically constrained by the cooling of the rocks surrounding the well. In these conditions, to some extent, a lower $\dot{w}$ can be compensated by increasing the flow rate, with pressure losses having only a limited impact. Conversely, a higher exergy efficiency η_{e_x} facilitates better conversion of the limited power that can be extracted from the well.

2.3 Liquids and Ideal Gasses Results

For ideal gasses and liquids the overall system can be solved analytically enabling a deeper understanding of the behaviour of the fluid inside the geothermal well. The analytical calculation produces the following outcomes (refer to Appendix 2.A for a comprehensive derivation):

Table 2.2: Analytic Model results for Ideal Gas and Liquids *(Non Dimensional)*

Element	*Fluid Type* **Liquid**	**Ideal Gas**
Spec. Work ($\dot{w}^{\#}$)	$\Delta z^{\#}\nabla {T_{rocks}}^{\#}$	$\Delta z^{\#}\left(\nabla {T_{rocks}}^{\#}-1\right)$
Spec. Exergy ($\dot{e}_x^{\#}$)	$\dot{w}^{\#}-ln\left(1+\Delta z^{\#}\nabla {T_{rocks}}^{\#}\right)$	$\dot{w}^{\#}-ln\left(\frac{1+\Delta z^{\#}\nabla {T_{rocks}}^{\#}}{1+\Delta z^{\#}}\right)$
Exergy Efficiency (η_{e_x})	$\left[1-\frac{ln\left(1+\Delta z^{\#}\nabla {T_{rocks}}^{\#}\right)}{\Delta z^{\#}\nabla {T_{rocks}}^{\#}}\right]/c_f$	$\left[1-\frac{ln\left(\frac{1+\Delta z^{\#}\nabla {T_{rocks}}^{\#}}{1+\Delta z^{\#}}\right)}{\Delta z^{\#}\left(\nabla {T_{rocks}}^{\#}-1\right)}\right]/c_f$
Direct Exp$_{\%\ \min}$ ($\dot{w}_{dex_{min}}$)	0.	$\frac{\Delta z^{\#}}{1+\Delta z^{\#}\nabla {T_{rocks}}^{\#}}$
Direct Exp$_{\%\ \max}$ ($\dot{w}_{dex_{max}}$)	0.	$\frac{\Delta z^{\#}}{\left(1+\Delta z^{\#}\nabla {T_{rocks}}^{\#}-\Delta z^{\#}\right)\left(1+\Delta z^{\#}\right)}$
with $c_f=\nabla {T_{rocks}}^{\#}\Delta z^{\#}/\left(1+\nabla {T_{rocks}}^{\#}\Delta z^{\#}\right)$		

The result in *Tab 2.2* are presented in a non-dimensional form to allow for a direct comparison between different fluid. The adimensional parameter are:

$$\dot{w}^{\#}=\frac{\dot{w}}{c_pT_{amb}} \tag{2.9}$$

$$\dot{e}_x^{\#}=\frac{\dot{e}_x}{c_pT_{amb}} \tag{2.10}$$

$$\Delta z^{\#}=\frac{g\Delta z}{c_pT_{amb}} \tag{2.11}$$

$$\nabla {T_{rocks}}^{\#}=\frac{c_p\nabla T_{rocks}}{g} \tag{2.12}$$

Where T_{amb} is the ambient temperature (in K) which is also the input temperature ($T_{amb}=T_0$), c_p is the specific heat (supposed constant in the presented analytical relations). The choice of such parameters is explained in Appendix 2.A. The relations described in *Tab 2.2* have been plotted in *Fig 2.5* and in *Fig 2.5*

From *Fig 2.4* it is clear that, in general, liquid has higher specific energy and exergy extraction rates while the usage of ideal gasses results in higher exergy efficiency, approaching 1 as $\nabla {T_{rocks}}^{\#}\to 1$. Moreover, for $\nabla {T_{rocks}}^{\#}\to\infty$ the ideal gas system approaches the liquid behaviour both in therms of extraction rates and exergy efficiency.

This happens because an high value of $\nabla {T_{rocks}}^{\#}$ indicates either a high heat capacity (c_p) of the fluid or a high thermal gradient in the rocks, which in turn reduces the temperature increase in the descending section or increases the temperature of the rocks in the reservoir, respectively. In both cases, the role of the compressibility of the fluid, whose main effect is to reduce the temperature difference between the fluid and the rocks at the *heating section* inlet, is decreased.

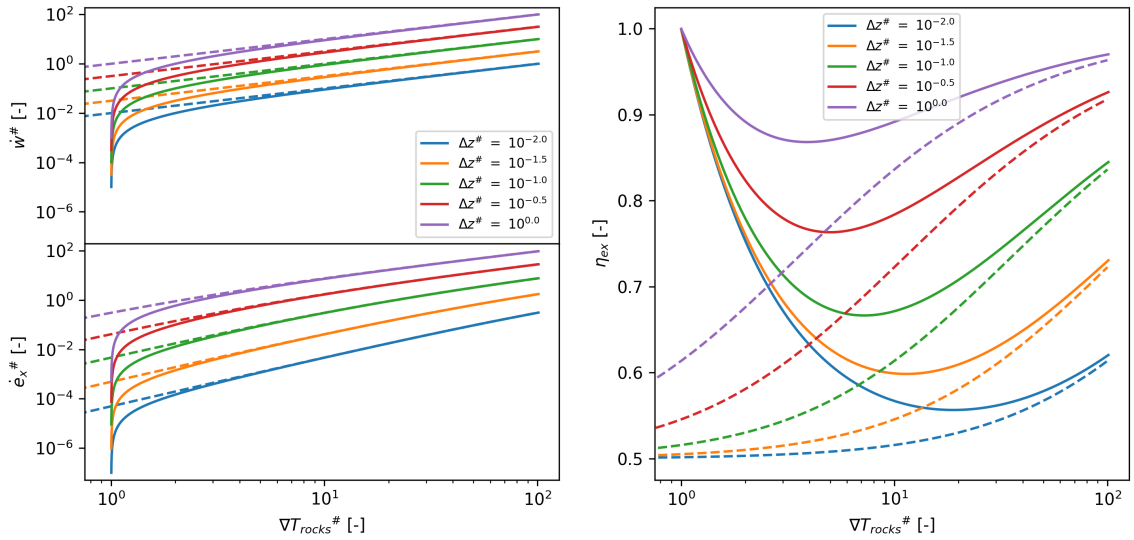

Figure 2.4: Analytical solution results. *Left: non dimensional specific energy (top) and exergy (bottom) extraction rate. Right: Exergy efficiency. Liquid results are represented by the dashed line.*

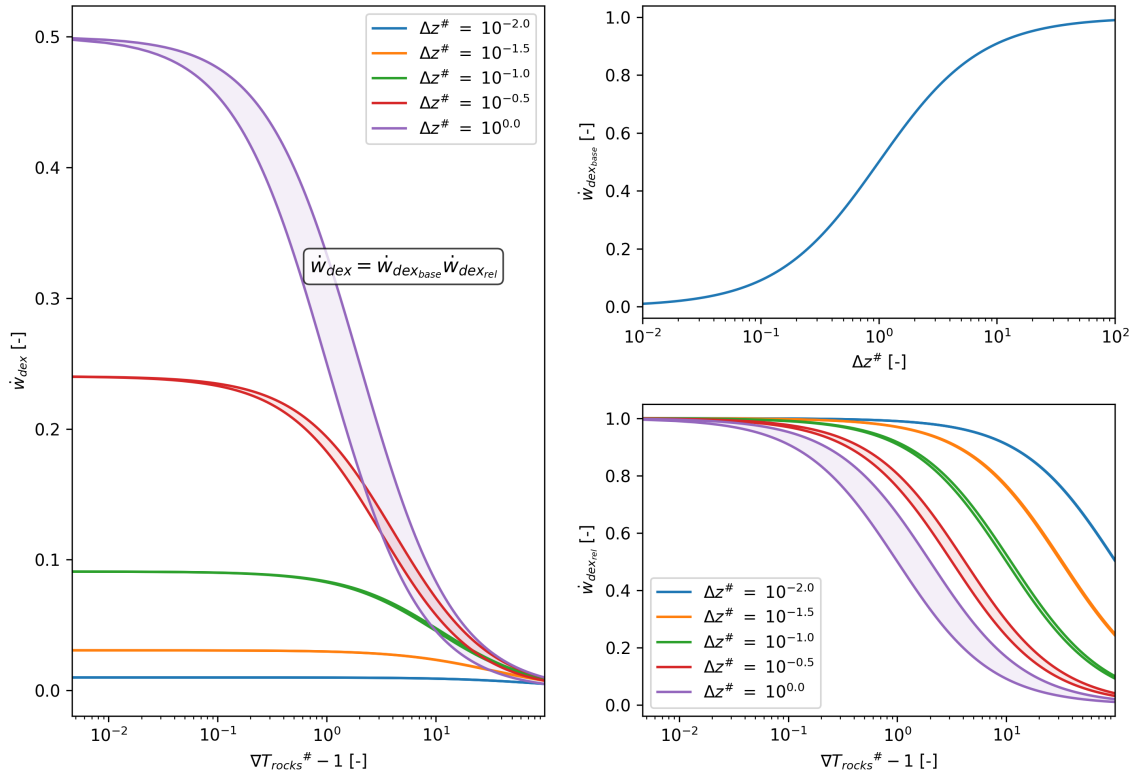

Figure 2.5: Relative impact of the direct expansion power production on the overall power extraction from the well. The two limiting curves for each value of $\Delta z^{\#}$ represents the conditions described in Section 2.2.2 *(expansion followed by cooling or cooling followed by expansion)*. The shaded area represents the intermediate states between these two conditions. $\dot{w}_{dex}$ is composed by two factors, $\dot{w}_{dex_{base}}$ and $\dot{w}_{dex_{rel}}$, shown on the right side, both constrained between 0 and 1.

On the other hand, as $\nabla T_{rocks}{}^{\#} \to 1$, the temperature at the inlet of the *heating section* approaches the surrounding rocks temperature reducing the relative amount of heat that can be extracted but, at the same time, increasing the efficiency (which, in an heat exchange process, is proportional to

the temperature difference between the two interacting elements).

Direct Expansion Relative Power

What has just been explained can also be observed by considering the relative amount of power extracted through direct expansion, as shown in *Fig 2.5*. In fact, for $\nabla T_{rocks}{}^{\#} \to \infty$, $\dot{w}_{dex} \to 0$. indicating that nearly all the power is extracted as heat, similar to a system that employs a liquid as a working fluid.
In contrast, when $\nabla T_{rocks}{}^{\#} \to 1$, $\dot{w}_{dex}$ approaches $\Delta z^{\#} / \left(1 + \Delta z^{\#}\right)$, representing a limiting value. For instance, when $\Delta z^{\#} = 1$, the maximum value of $\dot{w}_{dex}$ that can be achieved is 0.5. This implies that, in such a scenario, the amount of energy that can be converted using direct expansion cannot exceed 50% of the overall energy extracted from the reservoir, regardless of whether the expansion occurs before or after the cooling.
This can be further explained by noticing that $\dot{w}_{dex}$ can be seen as composed by two factors as follows:

$$[\dot{w}_{dex_{min}},\ \dot{w}_{dex_{max}}] = \underbrace{\frac{\Delta z^{\#}}{1 + \Delta z^{\#}}}_{\dot{w}_{dex_{base}}} \overbrace{\left[\frac{1 + \Delta z^{\#}}{1 + \Delta z^{\#} \nabla T_{rocks}{}^{\#}},\ \frac{1}{1 + \Delta z^{\#} \nabla T_{rocks}{}^{\#} - \Delta z^{\#}}\right]}^{\left[\dot{w}_{dex_{rel_{min}}},\ \dot{w}_{dex_{rel_{max}}}\right]} \tag{2.13}$$

$$[\dot{w}_{dex_{min}},\ \dot{w}_{dex_{max}}] = \dot{w}_{dex_{base}} \left[\dot{w}_{dex_{rel_{min}}},\ \dot{w}_{dex_{rel_{max}}}\right] \tag{2.14}$$

Where $\dot{w}_{dex_{base}}$ is the limiting value just described and is independent of both $\nabla T_{rocks}{}^{\#}$ and the placement of the expansion on the surface equipment.
On the other hand, $\dot{w}_{dex_{rel}}$ models how the rate of expansion power decreases with increasing $\nabla T_{rocks}{}^{\#}$ and is influenced by the placement of the expansion within the surface system.
From these results it is clear that **the maximum power ratio for the direct expansion can be achieved for high $\Delta z^{\#}$ and $\nabla T_{rocks}{}^{\#} \approx 1$ meaning deep reservoirs with limited geothermal gradients exploited by low c_p fluids**

Limiting non dimensional gradient

In addition to what just said, is interesting to notice that the curves presented in *Fig 2.4* could be re-scaled using for the x-axis another adimensional gradient defined as:

$$\nabla T_{rocks}{}^{\#\#} = \nabla T_{rocks}{}^{\#} - \nabla T_{rocks}{}^{\#}_{lim} \tag{2.15}$$

Where $\nabla T_{rocks}{}^{\#}_{lim}$ is the value of $\nabla T_{rocks}{}^{\#}$ below which no useful power can be extracted from the well (*0* for liquid and *1* for ideal gasses). The resized graphs are shown in *Fig 2.6*.
The new perspective presented in the figure can be interpreted as a comparison of the two different fluid behaviors as they approach their respective limiting gradients. In this perspective, the specific work for ideal gases and liquids is exactly the same, while the specific exergy behavior diverges, with ideal gases having a higher exergy production.
This difference becomes even more pronounced when considering exergy efficiency: For $\nabla T_{rocks}{}^{\#\#} \to$

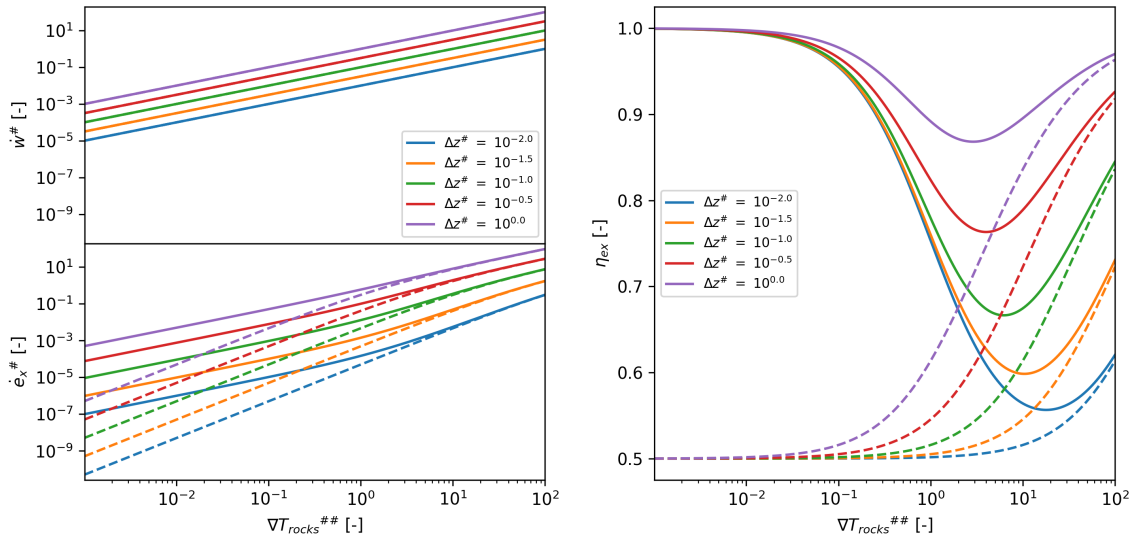

Figure 2.6: *Fig 2.4* with x-axis resized according to *Eq 2.15*

0, for liquid $\eta_{e_x} \to 0.5$, while for ideal gasses $\eta_{e_x} \to 1$. This can be explained by the fact that for gradients closer to the limit, liquid fluids continue to extract power as heat, whereas for ideal gases, power is extracted through direct expansion.

Real case scenario for an ideal gas: Using air in geothermal wells

To better understand the behavior of an ideal gas employed as the working fluid in a geothermal well, dimensional results have been obtained considering air properties ($c_p = 1$ kJ/(kg K), $\gamma = 1.4$). The outcomes are depicted in *Fig 2.7*.

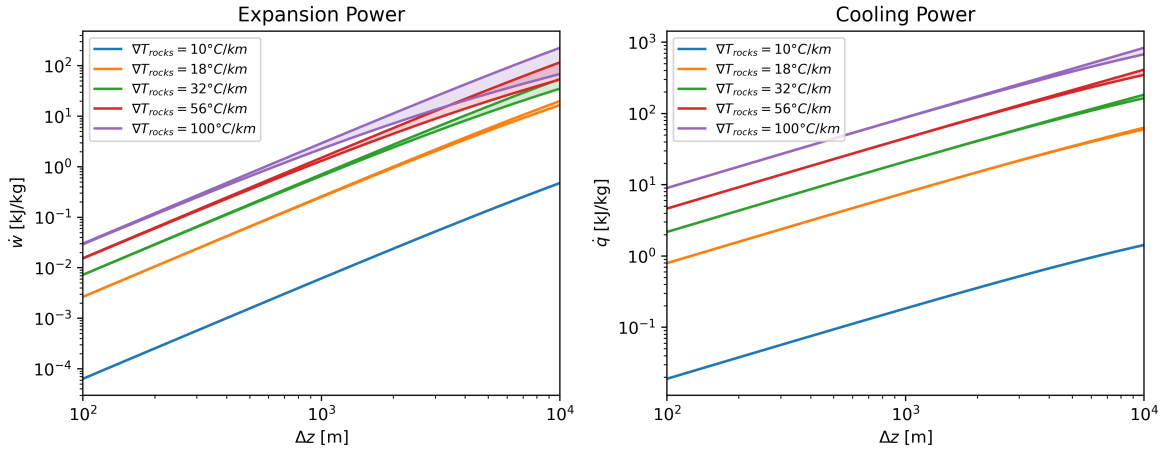

Figure 2.7: Dimensional results using air as working fluid. Again, the two limiting curves for each value of geothermal gradient represents the limiting conditions described in Section 2.2.2 *(expansion followed by cooling or cooling followed by expansion)*.

It is interesting to note that, theoretically, up to 100 kJ/kg can be achieved with air for direct expansion in a well with a depth in the order of kilometers and a geothermal gradient of 100°C/km. This implies that a MW-grade turbine could be powered with a flow rate of 10 kg/s of air. These values are, of course, theoretical limits and are not achievable in practical systems, but they provide an interesting basis for comparison.

2.4 Real Gasses Results

2.4.1 Introduction

In some condition, the pressurization of the system can be enhanced by the real fluid behaviour making their evaluation of extreme interest.
Unfortunately, an analytic solution is not easily achievable due to the increased complexity resulting from the implementation of a real gas EoS. For this reason, the ascending an descending section has been numerically integrated using Python.

Vertical Sections Integration To better integrate these sections, the system presented in *Eq 2.2* and *Eq 2.1* has been rewritten in order to explicit the density derivative (see the Appendix 2.B for the complete derivation and for the model validation):

$$dp = -\frac{g}{v}dz \tag{2.16}$$

$$dv = \frac{1}{\left.\frac{\partial p}{\partial v}\right|_T}\left(\left.\frac{\partial p}{\partial T}\right|_v \frac{v - \left.\frac{\partial h}{\partial p}\right|_T}{\left.\frac{\partial h}{\partial T}\right|_p} - 1\right)\frac{g}{v}dz \tag{2.17}$$

Or, expliciting the enthalpy derivatives:

$$dv = \frac{1}{\left.\frac{\partial p}{\partial v}\right|_T}\left(1 - \frac{R^\dagger}{c_p}\right)dp \tag{2.18}$$

Sometimes is better to use temperature instead of specific volume for the integration process:

$$dT = \left.\frac{\partial T}{\partial p}\right|_v dp + \left.\frac{\partial T}{\partial v}\right|_p dv = \frac{1}{\left.\frac{\partial p}{\partial v}\right|_T}\frac{R^\dagger}{c_p}dp \tag{2.19}$$

Where:

$$c_p = c_p^* + c_p^{dev} \; with \; c_p^{dev}(T, v) = R^\dagger - R_{spc} + \int_\infty^v T \left.\frac{\partial^2 p}{\partial T^2}\right|_v dv \tag{2.20}$$

And:

$$R^\dagger = -T\left(\left.\frac{\partial p}{\partial T}\right|_v\right)^2 / \left.\frac{\partial p}{\partial v}\right|_T ; \; v = \frac{1}{\rho}; \; R_{spc} = R/M_{molar} \tag{2.21}$$

The integral and the partial derivatives in *Eq 2.16*, *Eq 2.18* and *Eq 2.21* can be evaluated with the selected equation of state (derived in Appendix 2.C), c_p^* is ideal gas heat capacity of the fluid while c_p^{dev} is the deviation term of the real heat capacity. The integral and the partial derivatives in *Eq 2.16*, *Eq 2.18* and *Eq 2.21* can be evaluated with the selected equation of state *(derivation in Appendix 2.C*, c_p^* is ideal gas heat capacity of the fluid while c_p^{dev} is the deviation term of the real heat capacity. For REFPROP based calculation the system has been integrated using *Eq 2.16* and *Eq 2.17* while for EoS based calculation equation *Eq 2.18* has been used.

Additional Non-dimensional Parameters Another difference respect to the liquid and ideal gas behaviour is that with real gasses two more adimensional parameters are needed to describe the

inlet condition:

$$T_{rel} = \frac{T_0}{T_{crit}} \tag{2.22}$$

$$v_{rel} = \frac{v_0}{v_{crit}} \tag{2.23}$$

Where T_{crit} and v_{crit} are the critical temperature and specific volume. For some analysis, it is better to define the relative input pressure p_{rel} that the relative specific volume v_{rel}:

$$p_{rel} = \frac{p_0}{p_{crit}} \tag{2.24}$$

The need for these new parameters arises because real gas properties depend significantly more on the fluid state than those of ideal gases or liquids. For instance, for ideal gases and for liquids, $R = c_p - c_v$, remains constant regardless of the fluid's condition, while for the real gas this value will change.

Remarks on the derived equations

Some quick considerations can be derived from the equations just presented:

- *Eq 2.16* and *Eq 2.18* requires only the knowledge of the equation of state and of two additional parameters (c_p^* and M_{molar}) to model the be behaviour of the fluid. Because of this, especially for two or three-parameters based equation of state it is possible, instead of testing different fluids to identify the most suitable one for the selected application, to optimize the equation of state parameters and subsequently identify the fluid or the mixture with the closest behaviour to the theoretical optimum.
- $R^\dagger$ is a state function that is the *real gas equivalent* of the specific gas constant R_{spc} in terms of relation between c_p and c_v:

  $$R_{spc} = c_p^* - c_v^*; \quad R^\dagger = c_p - c_v \tag{2.25}$$

  Again, see Appendix 2.B for a complete derivation. This mean that $R^\dagger \to R_{spc}$ for low density conditions while $R^\dagger \to 0$ for liquids. This correctly model the fact that, from *Eq 2.18*, for incompressible fluids, an adiabatic transformation is very close to an isotherm:

  $$\frac{dv}{dp} \to \left.\frac{\partial v}{\partial p}\right|_T \quad for\ R^\dagger \to 0 \tag{2.26}$$

  The behavior of $R^\dagger$ just described can be clearly seen in *Fig 2.8* and *Fig 2.9*.
- $R^\dagger$ is very useful for understanding how to model the fluid for **ionic-fluids** mixture application. In fact, inserting a stream of particles in the fluid will equally increase both c_p and c_v so that $R^\dagger$ will not change. This can be modelled by simply increasing the value of $c_p^*(T)$ by a fixed amount depending on the concentration of the ionic particles in the fluid, while c_p^{dev} will remain unchanged. For REFPROP based calculation, the same thing can be done increasing $\left.\frac{\partial h}{\partial T}\right|_p$ in *Eq 2.17*. Is interesting to notice that increasing the particle concentration will decrease $R^\dagger/c_p$ again making the adiabatic transformation closer to an isotherm.

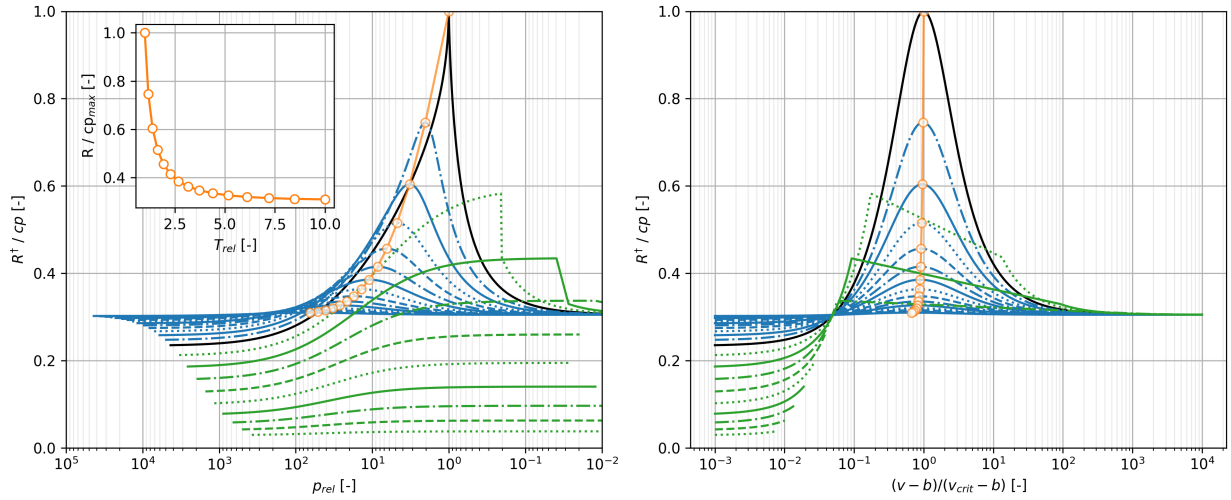

Figure 2.8: Behaviour of $R^\dagger/c_p$ as modelled by the Peng-Robinson EoS for a fixed c_p^* fluid. Blue lines represent super-critical isotherms, green lines correspond to sub-critical isotherms, and black lines depict the critical isotherm. *Note that in the supercritical region, each isotherm exhibits a distinct maximum for $R^\dagger/c_p$ (indicated by the orange line), which is plotted against the relative temperature in the inset graph. The volume at which the maximum occurs closely aligns with the critical volume for every isotherm. Furthermore, at high temperatures or high specific volumes, the behavior approaches that of an ideal gas (as $R^\dagger/c_p$ levels off to a specific value). Conversely, liquid behavior emerges under low-temperature sub-critical conditions ($R^\dagger/c_p \to 0$).*

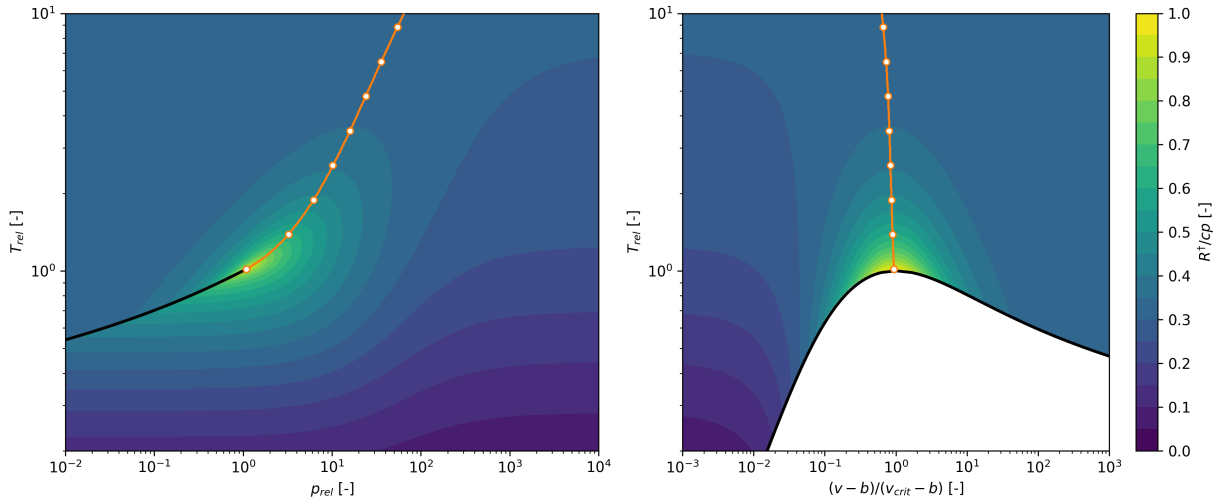

Figure 2.9: Behaviour of $R^\dagger/c_p$ as modelled by the Peng-Robinson EoS for a fixed c_p^* fluid (as in *Fig 2.8*). Shown as contours in the $p-t$ and $p-v$ planes

Limiting Gradient for Real Gasses

Considering very shallow depths ($\Delta z^\# \to 0$) the temperature profile in the well can be reconstructed integrating *Eq 2.19* with constant $\frac{R^\dagger}{c_p}$ resulting in:

$$\Delta T = \frac{g}{v \left.\frac{\partial p}{\partial T}\right|_v} \frac{R^\dagger}{c_p} \Delta z \tag{2.27}$$

For this reason, the limiting equation (*Eq 2.3*) results in:

$$\cancel{T_{amb}} + \frac{g}{v\left.\frac{\partial p}{\partial T}\right|_v}\frac{R^\dagger}{c_p}\cancel{\Delta z} < \cancel{T_{amb}} + \nabla T_{rocks}\cancel{\Delta z} \tag{2.28}$$

Rearranging:

$$\nabla {T_{rocks}}^{\#} = \frac{c_p \nabla T_{rocks}}{g} > \frac{R^\dagger}{v\left.\frac{\partial p}{\partial T}\right|_v} \tag{2.29}$$

Meaning that:

$$\nabla T_{rocks}^{\#}{}_{lim} = \frac{R^\dagger}{v\left.\frac{\partial p}{\partial T}\right|_v} \tag{2.30}$$

Eq 2.30 can also be rewritten as:

$$\nabla T_{rocks}^{\#}{}_{lim} = -\frac{T}{v}\frac{\left.\frac{\partial p}{\partial T}\right|_v}{\left.\frac{\partial p}{\partial v}\right|_T} \tag{2.31}$$

The limiting values presented in the equations above are consistent with the fact $\nabla T_{rocks}^{\#}{}_{lim} = 0$ for liquids and 1 for ideal gasses (for which $\left.\frac{\partial p}{\partial T}\right|_v = R/v$). The value of $\nabla T_{rocks}^{\#}{}_{lim}$ for a real gas is shown in *Fig 2.10*.

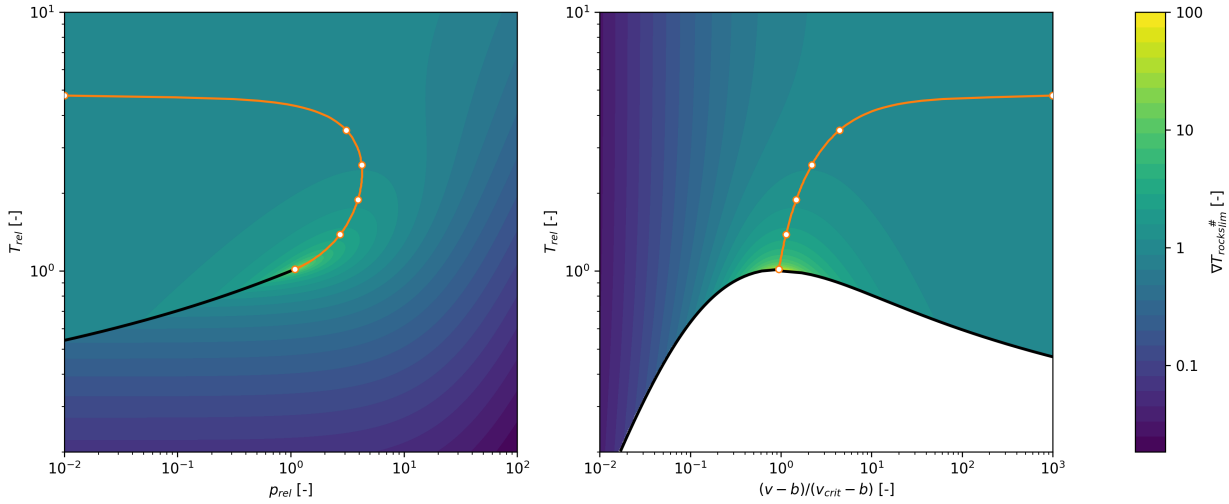

Figure 2.10: Behaviour of $\nabla T_{rocks}^{\#}{}_{lim}$ for $\Delta z^{\#} \to 0$ for a real fluid modeled by the Peng-Robinson EoS with a constant c_p^*. Observe the plateau at $\nabla T_{rocks}^{\#}{}_{lim} = 1$ representing the ideal-gas condition and the limit for $v \to b$ for which the liquid behaviour emerges ($\nabla T_{rocks}^{\#}{}_{lim} \to 0$). The orange lines indicate the locations of maximum $\nabla T_{rocks}^{\#}{}_{lim}$ for each T_{rel}

From the figure, a clear maximum emerges for trans-critical regions in which very high values of $\nabla T_{rocks}^{\#}{}_{lim}$ are observed ($\nabla T_{rocks}^{\#}{}_{lim} \to \infty$ at the critical point). This phenomenon occurs because, in such regions, a small change in pressure caused by an increase in depth results in a significant rise in temperature, driven by the low value of $\left.\frac{\partial p}{\partial T}\right|_v$ in that area. This necessitates a higher geothermal gradient to prevent the outlet temperature from the descending section from exceeding that of the surrounding rocks.

As just said, these results are valid only as long as $\frac{1}{\left.\frac{\partial p}{\partial T}\right|_v}\frac{R^\dagger}{c_p}$ is almost constant along the descending section of the well.

For higher values of $\Delta z^{\#}$, *Eq 2.30* can still be employed using a weighted mean of $\frac{R^{\dagger}}{v \left.\frac{\partial p}{\partial T}\right|_v}$ along the well defined as follows:

$$\nabla T_{rocks}{}^{\#}_{lim} = \left.\frac{R^{\dagger}}{v \left.\frac{\partial p}{\partial T}\right|_v}\right|_{mean} = \left(\int \frac{R^{\dagger}}{v \left.\frac{\partial p}{\partial T}\right|_v} \frac{dz}{c_p}\right) \frac{c_{p_{in}}}{\Delta z} \tag{2.32}$$

Which has to be evaluated numerically during the integration of the descending section of the well.

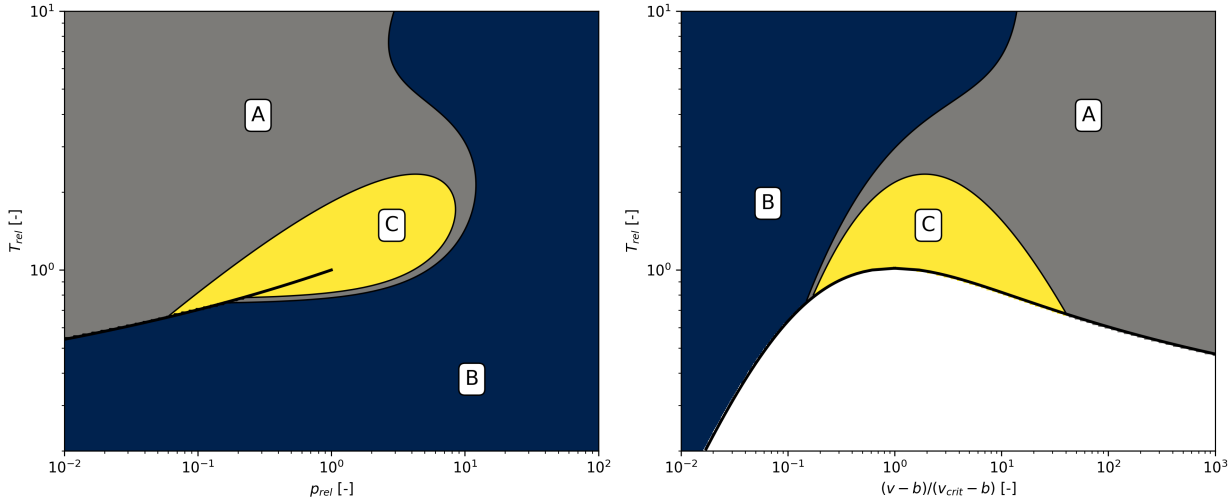

Figure 2.11: Identification of different real gas behaviour regions: A) Ideal Gas Region ($0.98 < \nabla T_{rocks}{}^{\#}_{lim} < 1.2$), B) Liquid and Super-Liquid region ($\nabla T_{rocks}{}^{\#}_{lim} < 0.98$), C) Trans-Critical region $\nabla T_{rocks}{}^{\#}_{lim} > 1.2$

2.4.2 Real Gasses Behaviour for limited $\Delta z^{\#}$ and $\nabla T_{rocks}{}^{\#}_{lim}$

Following the discoveries summarized in the introduction, three distinct regions, depicted in *Fig 2.11*, can be identified. These regions are characterized by different behaviors of the real gas:

A The **Ideal-Gas region** ($\nabla T_{rocks}{}^{\#}_{lim} \approx 1$). , which can be modeled using the analytical relation described in *Paragraph 2.3*.

B The **Liquid and Super-Liquid region** ($\nabla T_{rocks}{}^{\#}_{lim} < 1$), in which gas behavior gradually approaches the analytical solution for liquids.

C The **Trans-Critical region** ($\nabla T_{rocks}{}^{\#}_{lim} > 1$), where higher geothermal gradients are typically required for the system to operate, but high natural circulation effects are expected.

The behavior of the fluid in the last two regions will be described in the following paragraphs.

Liquid and Super-Liquid Behaviour

As already said, in the Liquid and Super-Liquid regions, the fluid behaviour gradually approaches the analytic result derived in the previous section for an ideal liquid. The way in which this shift happens is detailed in *Fig 2.12*. Moreover, in *Fig 2.13* the same behaviour has been shown with respect to $\nabla T_{rocks}{}^{\#\#}$.

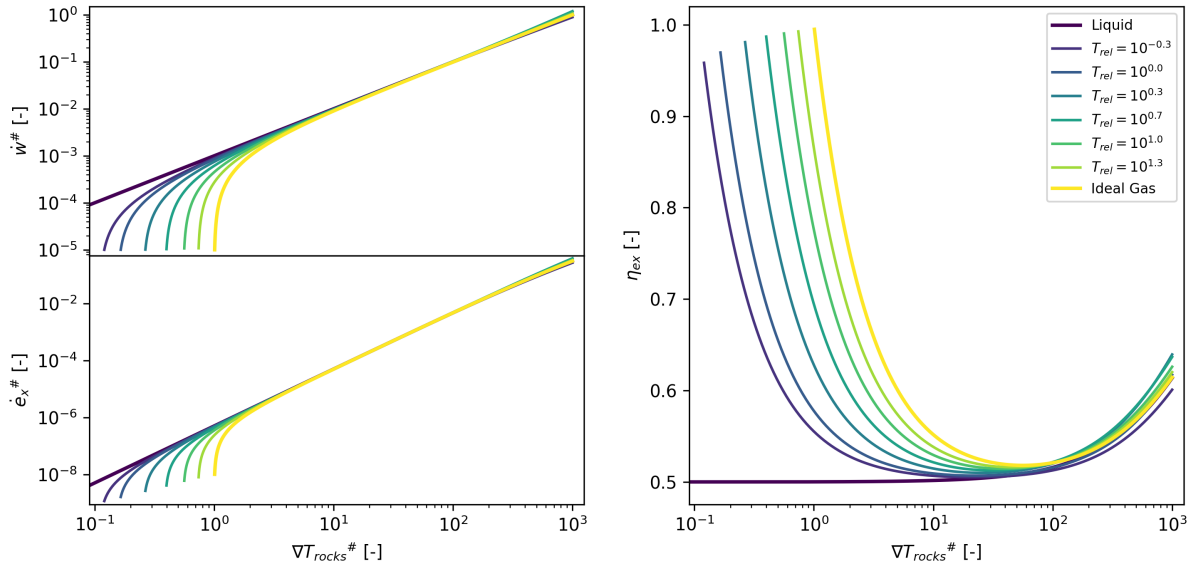

Figure 2.12: Super-Liquid real gas behaviour compared with analytical solution for ideal gas and liquid. *(Peng-Robinson EoS, $p_{rel} = 10^2$, $\Delta z^{\#} = 10^{-3}$)*

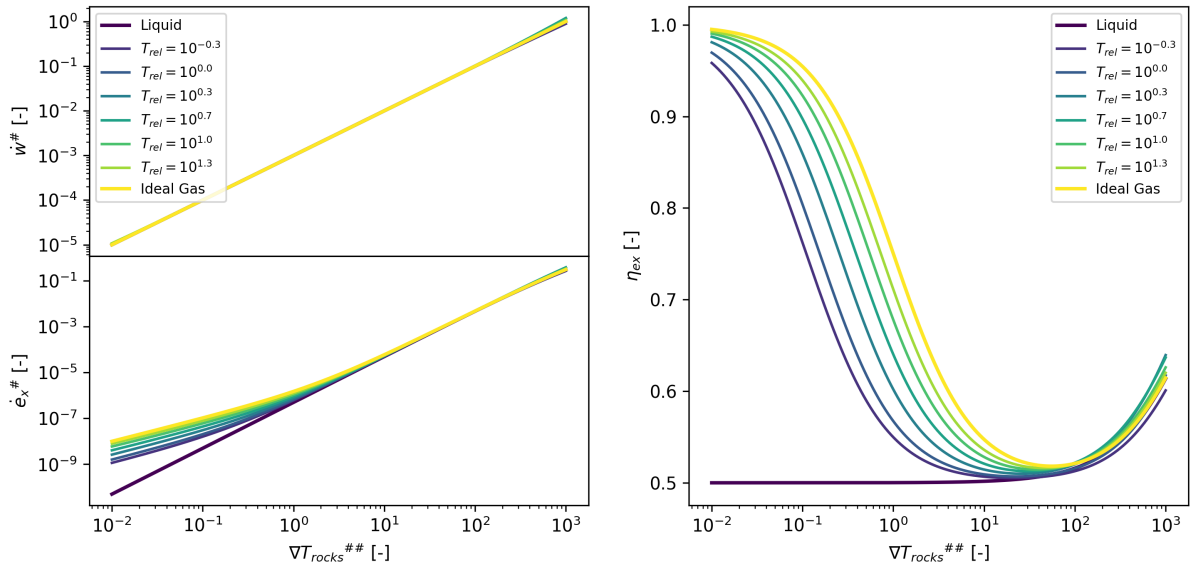

Figure 2.13: Same condition as *Fig 2.12* plotted against $\nabla T_{rocks}{}^{\#\#}$

From the figures, it is clear that for cooler (and hence less compressible) input states, not only does the limiting $\nabla T_{rocks}{}^{\#}$ get closer to 0 (hence approaching the ideal liquid condition), but also the extension of the range of gradients around the limiting point for which compressibility plays a significant role becomes narrower and narrower. This shift is evident in the efficiency plot in *Fig 2.13*, where it is shown that for cooler temperatures, the value of $\nabla T_{rocks}{}^{\#\#}$ at which the gradient starts to increase decreases.

Trans-Critical Behaviour

The exact same behaviour described for the Liquid and Super-Liquid regions is reversed for the supercritical conditions (as shown in *Fig 2.14* and in *Fig 2.15*). For state closer to the critical

condition, $\nabla T_{rocks}{}^{\#}_{lim}$ increase (peaking for specific volumes around the critical one) and the region influenced by the compressibility effect is extended.

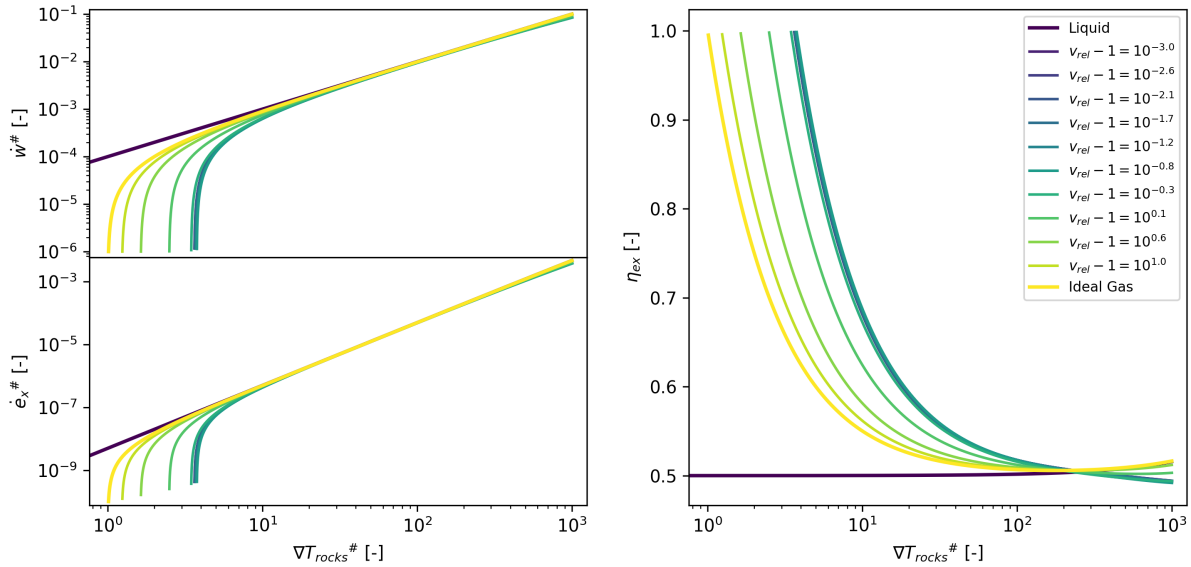

Figure 2.14: Trans-critical real gas behaviour compared with analytical solution for ideal gas and liquid. *(Peng-Robinson EoS, $T_{rel} = 10^2$, $\Delta z^{\#} = 10^{-3}$)*

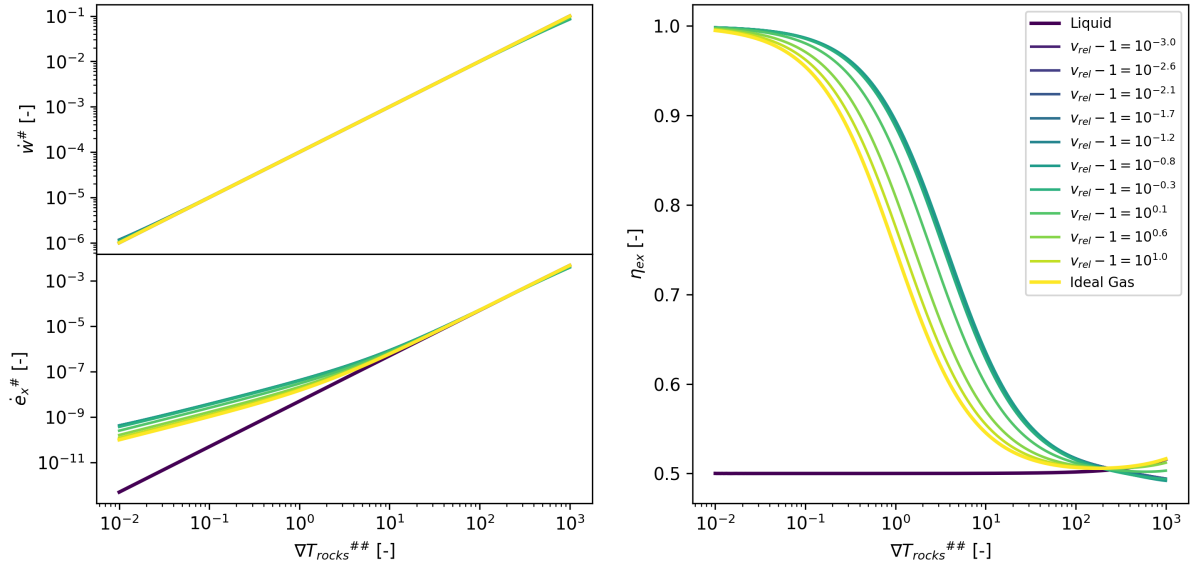

Figure 2.15: Same condition as *Fig 2.14* plotted against $\nabla T_{rocks}{}^{\#\#}$

2.4.3 Real Gasses Behaviour for higher $\Delta z^{\#}$ and $\nabla T_{rocks}{}^{\#}$

Thermosyphon effect in Super-liquid Condition

When either $\Delta z^{\#}$ or $\nabla T_{rocks}{}^{\#}$ started to increase, the conditions in the ascending and descending well will become non uniform. Moreover the difference between densities in the two wells can drive a significant natural circulation or pressurization. This is evident by looking at *Fig 2.16*, where, in

the region highlighted by the square, the predicted power output from the well become much higher that the base case represented by ideal gasses and liquid behaviour.

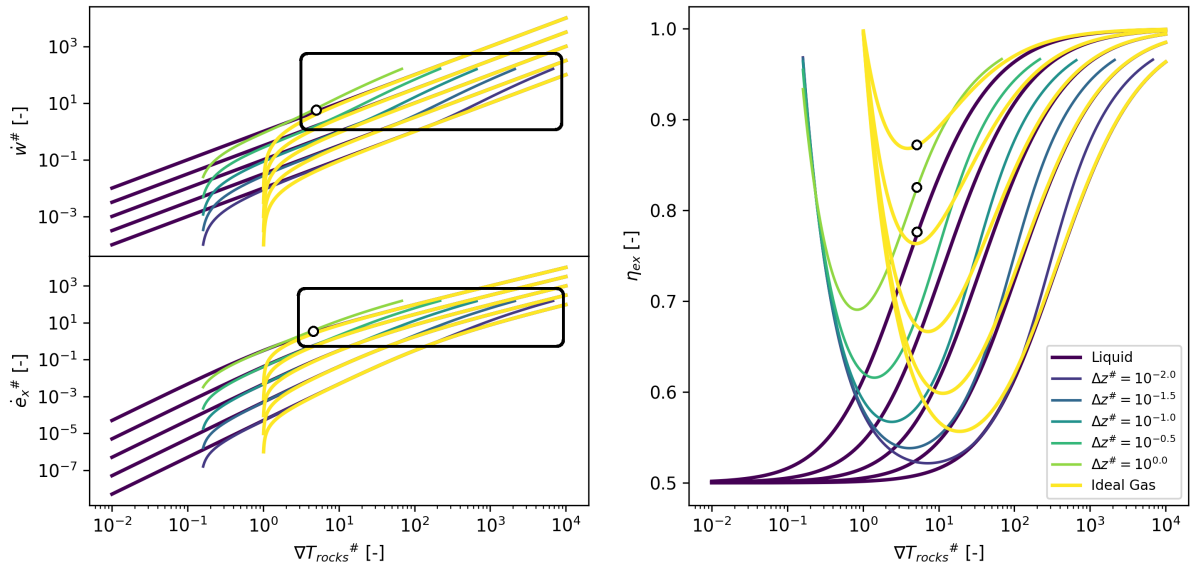

Figure 2.16: Non-dimensional power extraction from a well *(input condition: $T_{rel} = 0.5$ and $p_{rel} = 20$)* for different $\nabla T_{rocks}{}^{\#}$ and $\Delta z^{\#}$. The region displaying enhanced pressurization is highlighted in the box, and can be identified looking at the departure of real fluid behavior from both liquid and ideal gas predictions. The dots marks the calculation conditions for the points shown in *Tab 2.3*

To gain a better understanding of the phenomenon, we can compare the properties liquid and ideal and real gases at a specific condition marked with a circle in *Fig 2.16*. The properties are shown in *Tab 2.3*.

Table 2.3: Properties change inside the well for different fluid models in the condition marked in *Fig 2.16* ($T_{rel} = 0.5$, $p_{rel} = 20$, $\nabla T_{rocks}{}^{\#} = 7.57$, $\Delta z^{\#} = 1$)

Point	***Real Gas***			***Ideal Gas***			***Liquid***		
	p/p_0	T/T_0	ρ/ρ_0	p/p_0	T/T_0	ρ/ρ_0	p/p_0	T/T_0	ρ/ρ_0
0	1,00	1,00	1,00	1,00	1,00	1,00	1,00	1,00	1,00
1	3,27	1,16	1,07	11,3	2,00	5,66	3,19	1,00	1,00
2	3,27	8,58	0,58	11,3	8,58	1,32	3,19	8,58	1,00
3	**2,10**	**8,32**	0,48	**7,33**	**7,58**	0,97	**1,00**	**8,58**	1,00

Note: *Underlined values are fixed inputs (same for each fluid),* ***Bold*** *values are output of interest (pressure and temperature). In yellow is highlighted the change in density in the heating section. In red is highlighted the temperature at the outlet of the descending section. Points numbering refers to Fig 2.1*

From the table, it becomes evident that the specific work increase for real gasses is due to the fact that it combines the behaviour of liquid and ideal gasses.

The notable pressure rise observed at the outlet predominantly arises from the expansion occurring in the heating section (highlighted in yellow in the table). Consequently, in the vertical segments, the compressibility of the fluid has a reduced effect, resulting in only a marginal change of temperature in them. This means that, in these conditions, the gas will emerge from the well hotter for a real gas than for an ideal gas, but more importantly that the inlet of the heating section (highlighted in

red in the table) will be cooler allowing more heat to be extracted.

Thermosyphon effect Localization

But where does this effect actually start? To have a clearer picture is possible to plot the difference in specific energy extraction between liquid behaviour an real gas. In this new perspective, shown in *Fig 2.17*, the moment in which the value of $\dot{w}^{\#}$ started to rise for a real gas is much easier to identify. Moreover, the graph on the right shows that $\dot{w}^{\#}$ started to rise almost for the same value of $\nabla {T_{rocks}}^{\#} \Delta z^{\#}$

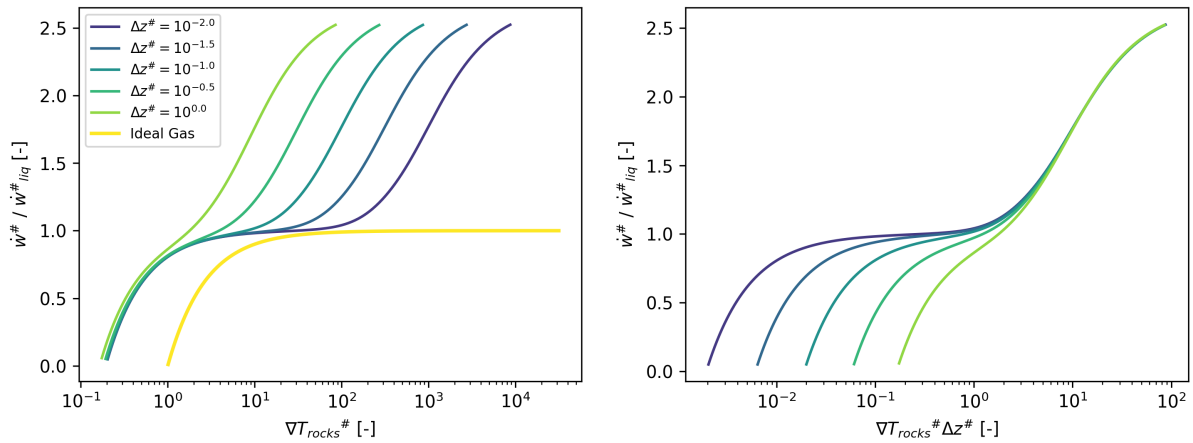

Figure 2.17: Ration between the predicted non-dimensional power extraction for a real-gas and a liquid *(input condition:* $T_{rel} = 0.5$ *and* $p_{rel} = 20$*)* for different $\nabla {T_{rocks}}^{\#}$ and $\Delta z^{\#}$. On the right the ration is plotted against $\nabla {T_{rocks}}^{\#} \Delta z^{\#}$ showing that, regardless of the depth, the increased natural circulation effect begins for $\nabla {T_{rocks}}^{\#} \Delta z^{\#} \approx 2$.

This can be explained considering that $\nabla {T_{rocks}}^{\#} \Delta z^{\#} = \frac{\nabla T_{rocks} \Delta z}{T_{amb}} = \frac{T_2 - T_{amb}}{T_{amb}}$. Hence, saying that the specific work increase happens at a specific $\nabla {T_{rocks}}^{\#} \Delta z^{\#}$ regardless of the well depth, means that the system has to reach a specific temperature at the outlet of the reservoir regardless of the down-hole pressure. This is reasonable considering the behaviour of super-liquid fluids shown in *Fig 2.8*, for which real gas behaviour tends to behaves like ideal gasses for higher temperatures regardless of the pressure.

Unfortunately a very high temperature is needed for reaching this super-liquid condition. For example $\nabla {T_{rocks}}^{\#} \Delta z^{\#} \approx 2$, the condition for which in *Fig 2.17* the real fluid behaviour barely starts to detach from the liquid, means that the temperature reached at the outlet of the heating section is twice (in K) the inlet temperature. Hence if the inlet temperature is 20°C (293.15K) the temperature of the fluid at the outlet of the reservoir must be at least 313°C (586.30K) for this effect to start playing a role. A temperature that is quite difficult to find in real geothermal conditions, though not impossible especially condition that there are almost no depth limitation.

Thermosyphon effect in Trans-Critical Condition

By lowering the inlet pressure to a sub-critical level is possible to make the fluid to exchange heat with the reservoir rocks in trans-critical, or even phase-changing conditions. This result in a steeper density increase in the *heating section* that can be achieved even with lower temperatures.

This effect can be spotted from *Fig 2.18* but is more evident when considering the ratio between the extracted work by a real gas and a liquid (*Fig 2.19*).

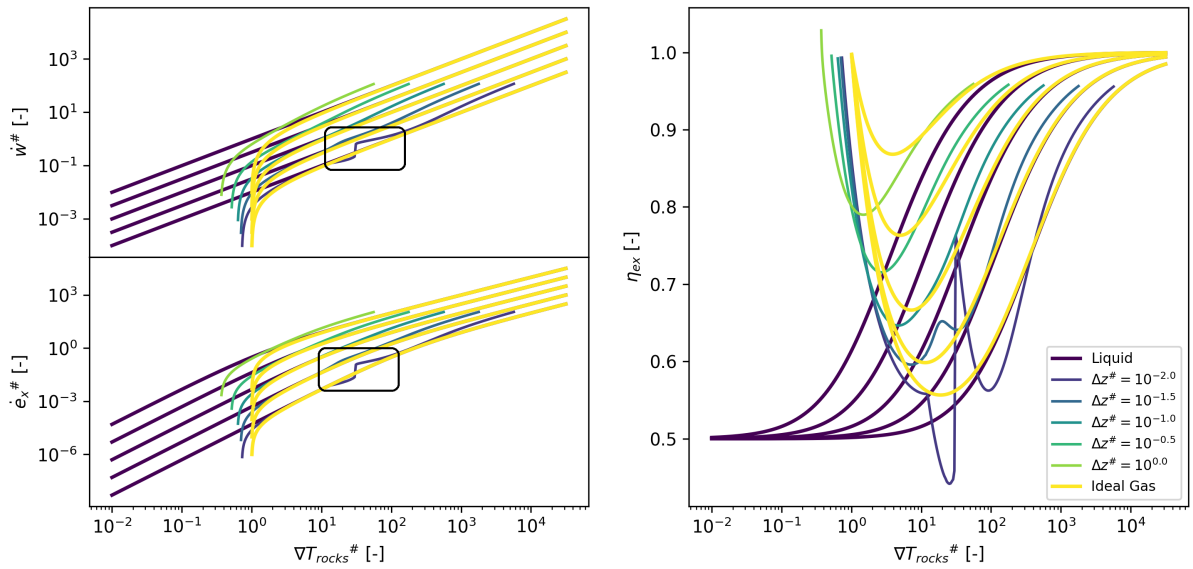

Figure 2.18: Non-dimensional power extraction from a well *(input condition:* $T_{rel} = 0.5$ *and* $p_{rel} = 0.25$*)* for different $\nabla T_{rocks}{}^{\#}$ and $\Delta z^{\#}$. The region displaying enhanced pressurization because of the trans-critical density increase is highlighted in the box.

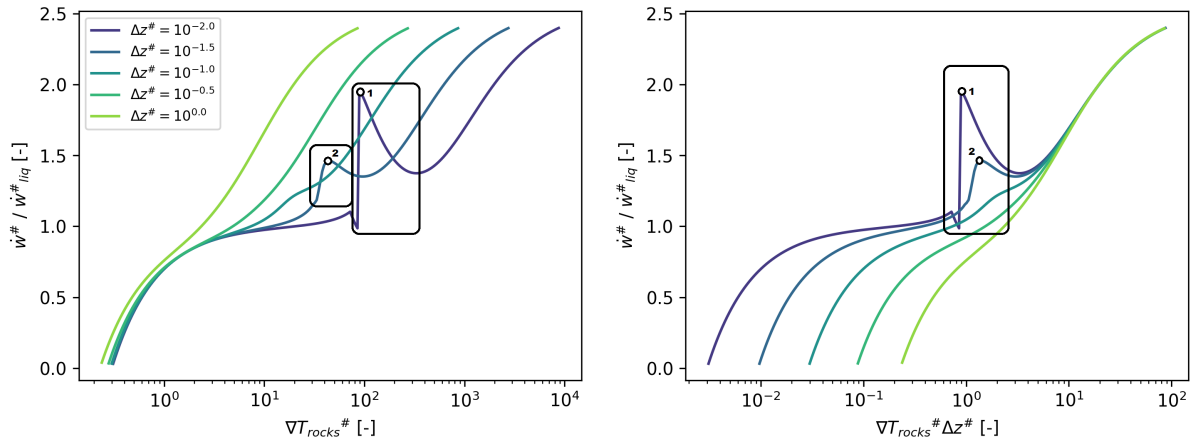

Figure 2.19: Ration between the predicted non-dimensional power extraction for a real-gas and a liquid *(input condition:* $T_{rel} = 0.5$ *and* $p_{rel} = 20$*)* for different $\nabla T_{rocks}{}^{\#}$ and $\Delta z^{\#}$. On the right the ration is plotted against $\nabla T_{rocks}{}^{\#}\Delta z^{\#}$.

From *Fig 2.19* is also evident that the power output increase for the shallower condition ($\Delta z^{\#}$=0.01) is much steeper than the others. This can be explained by the fact that for such shallow depth the pressure reached down-hole does not reach the critical pressure, hence the fluid evaporate in the heating section if the surrounding rocks temperature is high enough suddenly changing its density.
In *Fig 2.20* the profile of pressure and temperature change inside the well in the condition highlighted before is superimposed to the $R^{\dagger}/c_p$ plot of *Fig 2.9*.
From the plot is clear that injecting at higher pressure (*pink* curve - marked point in *Fig 2.16*) means that an higher temperature rise is needed to reach the region with higher density change.

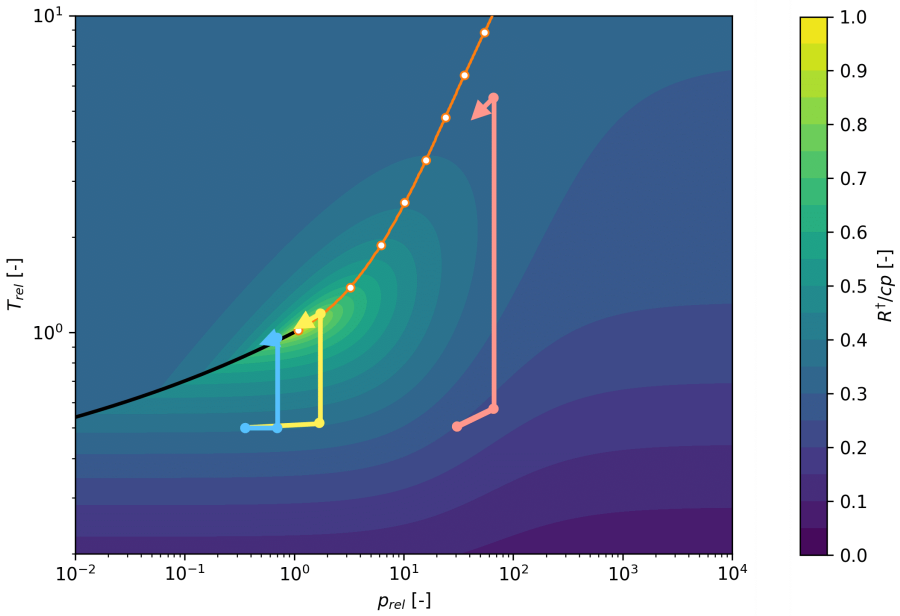

Figure 2.20: Pressure and Temperature change inside the well for real gas given different conditions. Superimposed on the $R^\dagger/c_p$ plot. *In blue*: Point 1 in *Fig 2.19*, $T_{rel} = 0.5$, $p_{rel} = 0.25$, $\nabla {T_{rocks}}^{\#} = 81.80$, $\Delta z^{\#} = 0.01$. *In yellow*: Point 2 in *Fig 2.19*, $T_{rel} = 0.5$, $p_{rel} = 0.25$, $\nabla {T_{rocks}}^{\#} = 34,87$, $\Delta z^{\#} = 10^{-1.5}$. *In orange*: Point marked in *Fig 2.16*, $T_{rel} = 0.5$, $p_{rel} = 20$, $\nabla {T_{rocks}}^{\#} = 7.57$, $\Delta z^{\#} = 1$

On the other hand, the other two curves (*blue* curve - point 1 in *Fig 2.20*, *yellow* curve - point 2) shows that, if a sub-critical inlet pressure is imposed, a much lower reservoir temperature is required to reach a low-density state down-hole.

Another interesting thing to notice is that, for trans-critical conditions, the optimal condition at the outlet of the *heating section* is the one that maximize $R^\dagger/c_p$, which helps the identification of the optimal gradient.

2.5 Conclusion

The following conclusions can be retrieved from the results just presented:

- There is a **minimum geothermal gradient**, different from each fluid condition, below which no power can be extracted from the well. The local formulation of this limit for real fluids is the following:

$$\nabla T_{rocks}{}^{\#}_{lim} = \frac{R^{\dagger}}{v \left.\frac{\partial p}{\partial T}\right|_v} \tag{2.33}$$

  $\nabla T_{rocks}{}^{\#}_{lim} = 1$ for ideal gassed and 0 for liquids. For deep wells, for which the condition of the fluid change significantly while descending, a mean value of the limit should be considered:

$$\nabla T_{rocks}{}^{\#}_{lim} = \left.\frac{R^{\dagger}}{v \left.\frac{\partial p}{\partial T}\right|_v}\right|_{mean} = \left(\int \frac{R^{\dagger}}{v \left.\frac{\partial p}{\partial T}\right|_v} \frac{dz}{c_p}\right) \frac{c_{p_{in}}}{\Delta z} \tag{2.34}$$

- For low gradients, close to $\nabla T_{rocks}{}^{\#}_{lim}$, the specific power extraction drops. Despite of this, for compressible fluids the exergy efficiency of the power extraction process increases approaching 1, as, in relative therms more thermal power is converted in pressure increase at the outlet. On the other hand for completely uncompressible fluids efficiency approaches 0.5 as power production decrease.

- For high geothermal gradients the behaviour of compressible and uncompressible fluids becomes similar as the compression effect due to the descent in the geothermal well becomes negligible compared with the great increase in temperature.

- In some specific condition real-fluids injected with liquid-like density can undergo a significant density decrease in the reservoir allowing much more specific power to be produced, up to 2.5 times more if compared with liquid in the same condition. This is because most of the power is extracted in form of *latent heat* caused by the density decrease. The optimal condition to obtain these effect is the ones in which the fluid is injected as fluid at relatively low pressure so that it will not be much higher that the critical pressure after the natural compression that occurs while reaching the reservoir.

References

[1] P. Thomsen, "Geothermal selection in California resource planning: Preliminary results from the CPUC's IRP tools and recommendations for future development and analysis," Tech. Rep., 2018. [Online]. Available: http://www.cpuc.ca.gov/sb350/..

[2] D. Brown, "A Hot Dry Rock Geothermal Energy Concept Utilizing Supercritical CO2 Instead of Water," *Twenty-Fifth Workshop on Geothermal Resevoir Engineering*, 2000, ISSN: 2195-9706.

[3] K. Pruess, "Enhanced geothermal systems (EGS) using CO2 as working fluid - A novel approach for generating renewable energy with simultaneous sequestration of carbon," *Geothermics*, vol. 35, no. 4, pp. 351–367, Aug. 2006, ISSN: 03756505. DOI: 10.1016/j.geothermics.2006.08.002.

[4] T. Xu and K. Pruess, "Reactive Transport Modeling to Study Fluid-Rock Interactions in Enhanced Geothermal Systems (EGS) with CO2 as Working Fluid," in *Proceedings World Geothermal Congress*, Bali, Indonesia, Apr. 2010.

[5] J. Apps and K. Pruess, "Modeling geochemical processes in enhanced geothermal systems with CO2 as heat transfer fluid," in *Thirty-Sixth Workshop on Geothermal Reservoir Engineering*, Stanford, California, Jan. 2011. [Online]. Available: https://www.researchgate.net/publication/228707224.

[6] K. Pruess and N. Spycher, "Enhanced Geothermal Systems (EGS) with CO2 as Heat Transmission Fluid - A Scheme for Combining Recovery of Renewable Energy with Geologic Storage of CO2," Lawrence Berkeley National Laboratory, Tech. Rep., 2009.

[7] Y. Zhang, C. Yu, G. Li, *et al.*, "Performance analysis of a downhole coaxial heat exchanger geothermal system with various working fluids," *Applied Thermal Engineering*, vol. 163, Dec. 2019, ISSN: 13594311. DOI: 10.1016/j.applthermaleng.2019.114317.

[8] A. E. Malek, B. M. Adams, E. Rossi, H. O. Schiegg, and M. O. Saar, "Techno-economic analysis of Advanced Geothermal Systems (AGS)," *Renewable Energy*, vol. 186, pp. 927–943, 2022, ISSN: 09601481. DOI: 10.1016/j.renene.2022.01.012.

[9] A. D. Atrens, H. Gurgenci, and V. Rudolph, "CO2 Thermosiphon for Competitive Geothermal Power Generation," *Energy & Fuels*, vol. 23, no. 1, pp. 553–557, Jan. 2009, ISSN: 0887-0624. DOI: 10.1021/ef800601z.

[10] B. Janke and T. Kuehn, "Geothermal Power Cycle Analysis for Commercial Applicability using Sequestrated Supercritical CO2 as a Heat Transfer or Working Fluid," in *Proceedings of the ASME 2011 5th International Conference on Energy Sustainability*, 2011. [Online]. Available: http://asme.org/terms.

[11] B. M. Adams, T. H. Kuehn, J. M. Bielicki, J. B. Randolph, and M. O. Saar, "A comparison of electric power output of CO2 Plume Geothermal (CPG) and brine geothermal systems for varying reservoir conditions," *Applied Energy*, vol. 140, pp. 365–377, Feb. 2015, ISSN: 03062619. DOI: 10.1016/j.apenergy.2014.11.043.

[12] X. Wang, "Investigation of Geothermal Heat Extraction Using Supercritical Carbon Dioxide (sCO2) and Its Utilization in sCO2-based Power Cycles and Organic Rankine Cycles - A Thermodynamic & Economic Perspective," Tech. Rep., 2018.

[13] M. Tagliaferri, P. Gładysz, P. Ungar, *et al.*, "Techno-Economic Assessment of the Supercritical Carbon Dioxide Enhanced Geothermal Systems," *Sustainability*, vol. 14, no. 24, p. 16 580, Dec. 2022, ISSN: 2071-1050. DOI: 10.3390/su142416580.

[14] B. M. Adams, T. H. Kuehn, J. M. Bielicki, J. B. Randolph, and M. O. Saar, "On the importance of the thermosiphon effect in CPG (CO2 plume geothermal) power systems," *Energy*, vol. 69, pp. 409–418, May 2014, ISSN: 03605442. DOI: 10.1016/j.energy.2014.03.032.

[15] E. W. Lemmon, I. H. Bell, M. L. Huber, and M. O. McLinden, *NIST Standard Reference Database 23: Reference Fluid Thermodynamic and Transport Properties-REFPROP, Version 10.0, National Institute of Standards and Technology*, 2018.

[16] J. Dormand and P. Prince, "A family of embedded Runge-Kutta formulae," *Journal of Computational and Applied Mathematics*, vol. 6, no. 1, pp. 19–26, Mar. 1980, ISSN: 03770427. DOI: 10.1016/0771-050X(80)90013-3.

[17] P. Virtanen, R. Gommers, T. E. Oliphant, *et al.*, "SciPy 1.0: fundamental algorithms for scientific computing in Python," *Nature Methods*, vol. 17, no. 3, pp. 261–272, Mar. 2020, ISSN: 1548-7091. DOI: 10.1038/s41592-019-0686-2.

Appendices

2.A Liquid and Ideal Gasses Analytic Derivation

2.A.1 Liquids

For liquids ($\rho = const.$), the analytical solution of the equations of the system is straightforward. For the ascending and descending sections, integrating *Eq 2.1* and *Eq 2.2* results in:

$$\Delta p = \rho g \Delta z \tag{2.35}$$

$$\Delta T = 0 \tag{2.36}$$

which, together with the heating section's conditions (*Tab 2.1*), simplifies in:

$$\Delta p_{3\to 0} = 0. \tag{2.37}$$

$$\Delta h_{3\to 0} = c_p \left(T_3 - T_0\right) = c_p \nabla T_{rocks} \Delta z \tag{2.38}$$

It is interesting to notice that, because of *Eq 2.36*, $T_1 = T_{amb}$, hence the limiting equation (*Eq 2.3*) reduces to:

$$\nabla T_{rocks} > 0 \tag{2.39}$$

Overall System

From the relations described above, system performances can be retrieved:

$$\dot{w} = \Delta h_{3\to 0} = c_p \nabla T_{rocks} \Delta z \tag{2.40}$$

$$\dot{e}_x = \Delta h_{3\to 0} - T_{amb} \Delta s_{3\to 0} = c_p T_{amb} \left[\frac{\nabla T_{rocks} \Delta z}{T_{amb}} - ln\left(1 + \frac{\nabla T_{rocks} \Delta z}{T_{amb}}\right)\right] \tag{2.41}$$

$$\eta_{e_x} = \frac{\dot{e}_x}{c_f \ \dot{w}} = \frac{\cancel{c_p T_{amb}} \left[\frac{\nabla T_{rocks} \Delta z}{T_{amb}} - ln\left(1 + \frac{\nabla T_{rocks} \Delta z}{T_{amb}}\right)\right]}{c_f \ \cancel{c_p T_{amb}} \frac{\nabla T_{rocks} \Delta z}{T_{amb}}} = \left[1 - \frac{ln\left(1 + \frac{\nabla T_{rocks} \Delta z}{T_{amb}}\right)}{\frac{\nabla T_{rocks} \Delta z}{T_{amb}}}\right] / c_f \tag{2.42}$$

Because of the absence of pressurization, the amount of exergy that can be extracted trough direct expansion is zero:

$$[\dot{w}_{dex_{min}},\ \dot{w}_{dex_{max}}] = [0.,\ 0.] \tag{2.43}$$

2.A.2 Ideal Gasses

Ascending/Descending Section

For ideal gasses, the vertical sections can be evaluated considering the adiabatic compression relations:

$$\frac{p_{out}}{p_{in}} = \left(\frac{T_{out}}{T_{in}}\right)^{\frac{\gamma}{\gamma-1}} \tag{2.44}$$

$$\Delta h = c_p \left(T_{out} - T_{in}\right) \tag{2.45}$$

Where γ is the heat capacity ratio. Combining *Eq 2.2* and *Eq 2.45* results in:

$$\Delta h = g\Delta z = c_p T_{in} \left(\frac{T_{out}}{T_{in}} - 1\right) \tag{2.46}$$

Rearranging:

$$\tau_{in\to out} = \frac{T_{out}}{T_{in}} = 1 + \frac{g\Delta z}{c_p T_{in}} \tag{2.47}$$

Which is correct for the descending section (the outlet temperature is higher than the inlet). For the ascending section, the formula can be reversed as:

$$\tau_{in\to out} = \frac{T_{out}}{T_{in}} = 1 - \frac{g\Delta z}{c_p T_{in}} \tag{2.48}$$

Two different formulation are needed as Δz has been considered positive in both formulas.
The compression ratio can be evaluated from the temperature ratio:

$$\beta_{in\to out} = \frac{p_{out}}{p_{in}} = {\tau_{in\to out}}^{\frac{\gamma}{\gamma-1}} \tag{2.49}$$

Heating Section

The heating section can be modelled using the relations presented in *Tab 2.1.* Moreover, because of *Eq 2.47*, *Eq 2.3* can be rewritten as:

$$T_{amb} + \nabla T_{rocks}\Delta z > \left(1 + \frac{g\Delta z}{c_p T_{amb}}\right) T_{amb} \tag{2.50}$$

Which can be simplified in:

$$\frac{c_p \nabla T_{rocks}}{g} > 1 \tag{2.51}$$

This means that the geothermal gradient has a lower limit below which the system cannot operate with an ideal gas as working fluid, for example, considering a system which employs air ($c_p = 1$ kJ/(kg K)), the minimum heat flux is $\nabla T_{rocks_{min}} = 9.81$ °C/km. Which is not negligible, meaning that **geothermal systems based on compressible fluids** are usually more suitable for **regions with high heat flux**.

Overall System

To assess the influence of direct expansion on the overall power production, it is essential to evaluate the pressure and temperature ratios across the expansion process.

Given that pressure remains constant in the heating section ($p_1 = p_2$) and in the surface plant heat exchangers ($p_3 = p_{3'}$ and $p_{3''} = p_0$), the pressure ratio is unaffected by the placement of the expansion within the surface equipment. Therefore, it can be determined by considering the pressure ratios of the ascending and descending sections.

$$\beta_{exp} = \beta_{3\to0} = \frac{p_3}{p_2}\frac{p_2}{p_0} = \beta_{2\to3}\beta_{0\to1} = \left[\left(1 - \frac{g\Delta z}{c_p^* T_2}\right)\left(1 + \frac{g\Delta z}{c_p^* T_{amb}}\right)\right]^{\frac{\gamma}{\gamma-1}} \tag{2.52}$$

Because of this, for ideal gasses, the temperature ratio is constant as well:

$$\tau_{exp} = {\beta_{exp}}^{\frac{\gamma-1}{\gamma}} = \left(1 - \frac{g\Delta z}{c_p^* T_2}\right)\left(1 + \frac{g\Delta z}{c_p^* T_{amb}}\right) \tag{2.53}$$

The specific energy extraction can be easily identified evaluating the enthalpy variation between the inlet and the outlet:

$$\dot{w} = \Delta h_{3\to0} = c_p^* \left(T_3 - T_{amb}\right) = c_p^* T_{amb} \left(\tau_{3\to0} - 1\right) \tag{2.54}$$

with:

$$\tau_{3\to0} = \frac{T_3}{T_{amb}} = \frac{\tau_{2\to3} T_2}{T_{amb}} = \left(1 - \frac{g\Delta z}{c_p^* T_2}\right)\frac{T_2}{T_{amb}} \tag{2.55}$$

Is important to notice that while $\beta_{exp} = \beta_{3\to0}$, $\tau_{exp} \neq \tau_{3\to0}$, this is because both in the heating section and in the surface plant heat exchangers the temperature will not remain fixed.
This play an important role for the specific exergy calculation:

$$\dot{e}_x = \Delta h_{3\to0} - T_{amb}\Delta s_{3\to0} = c_p^* T_{amb}\left[\left(\tau_{3\to0} - 1\right) - \left(ln\left(\tau_{3\to0}\right) - \frac{R_{spc}}{c_p^*} ln\left(\beta_{3\to0}\right)\right)\right] \tag{2.56}$$

by substituting $\beta_{exp} = {\tau_{exp}}^{\frac{\gamma}{\gamma-1}}$:

$$\dot{e}_x = c_p^* T_{amb}\left[\left(\tau_{3\to0} - 1\right) - \left(ln\left(\tau_{3\to0}\right) - \frac{R_{spc}}{c_p^*} ln\left({\tau_{exp}}^{\frac{\gamma}{\gamma-1}}\right)\right)\right] \tag{2.57}$$

Resulting in:

$$\dot{e}_x = c_p^* T_{amb}\left[\left(\tau_{3\to0} - 1\right) - ln\left(\frac{\tau_{3\to0}}{\tau_{exp}}\right)\right] \tag{2.58}$$

Or, expliciting:

$$\dot{e}_x = c_p^* T_{amb}\left[\left(1 - \frac{g\Delta z}{c_p^* T_2}\right)\frac{T_2}{T_{amb}} - 1 - ln\left(\frac{\frac{T_2}{T_{amb}}}{1 + \frac{g\Delta z}{c_p^* T_{amb}}}\right)\right] \tag{2.59}$$

The exergy efficiency follow from *Eq 2.58* and *Eq 2.54*:

$$\eta_{e_x} = \frac{\dot{e}_x}{c_f\ \dot{w}} = \frac{\cancel{c_p^* T_{amb}}\left[\left(\tau_{3\to0} - 1\right) - ln\left(\frac{\tau_{3\to0}}{\tau_{exp}}\right)\right]}{c_f\ \cancel{c_p^* T_{amb}}\left(\tau_{3\to0} - 1\right)} = \left[1 - \frac{ln\left(\frac{\tau_{3\to0}}{\tau_{exp}}\right)}{\tau_{3\to0} - 1}\right]/c_f \tag{2.60}$$

The relative impact of the direct expansion on power production can be evaluated starting from *Eq*

2.8, considering that:

$$\Delta h_{3'\to 0} = c_p^* T_{amb}\left(\frac{T_{3'}}{T_{amb}} - 1\right) = c_p^* T_{amb}\left(\tau_{3'\to 0} - 1\right) \tag{2.61}$$

$$\Delta h_{3\to 3''} = c_p^* T_3\left(1 - \frac{T_{3''}}{T_3}\right) = c_p^* T_{amb}\left(1 - \frac{1}{\tau_{3\to 3''}}\right) \tag{2.62}$$

Anyway, as τ_{exp} is independent on the location of the expansion in the surface cycle, it can be noticed that:

$$\tau_{3'\to 0} = \tau_{3\to 3''} = \tau_{exp} \tag{2.63}$$

resulting in:

$$[\dot{w}_{dex_{min}},\ \dot{w}_{dex_{max}}] = \frac{\cancel{c_p^* T_{amb}}\left[\tau_{exp} - 1,\ \frac{\tau_{exp}-1}{\tau_{exp}}\right]}{\cancel{c_p^* T_{amb}}\left(\tau_{3\to 0} - 1\right)} \tag{2.64}$$

2.A.3 Adimensionalization

Some interesting non dimensional parameter have emerged form the analysis above:

$$\Delta z^{\#} = \frac{g\Delta z}{c_p T_{amb}} \tag{2.65}$$

$$\nabla T_{rocks}{}^{\#} = \frac{c_p \nabla T_{rocks}}{g} \tag{2.66}$$

From which it results:

$$\frac{\nabla T_{rocks}\Delta z}{T_{amb}} = \Delta z^{\#}\nabla T_{rocks}{}^{\#} \tag{2.67}$$

Moreover, the specific energy and exergy can be adimensionalized as follows:

$$\dot{w}^{\#} = \frac{\dot{w}}{c_p T_{amb}} \tag{2.68}$$

$$\dot{e}_x^{\#} = \frac{\dot{e}_x}{c_p T_{amb}} \tag{2.69}$$

Finally, temperatures can be adimensionalized with respect to the ambient temperature:

$$T_x{}^{\#} = \frac{T_x}{T_{amb}} \tag{2.70}$$

Hence:

$$T_2{}^{\#} = \frac{T_2}{T_{amb}} = 1 + \frac{\nabla T_{rocks}\Delta z}{T_{amb}} = 1 + \Delta z^{\#}\nabla T_{rocks}{}^{\#} \tag{2.71}$$

Given these adimensional parameter the results for liquid and ideal gasses can be rewritten as:

A - Liquids

$$\dot{w}^{\#} = \Delta z^{\#}\nabla T_{rocks}{}^{\#} \tag{2.72}$$

$$\dot{e}_x^{\#} = \left(\Delta z^{\#}\nabla T_{rocks}{}^{\#} - ln\left(1 + \Delta z^{\#}\nabla T_{rocks}{}^{\#}\right)\right) \tag{2.73}$$

$$\eta_{e_x} = \left[1 - \frac{ln\left(1 + \Delta z^{\#} \nabla {T_{rocks}}^{\#}\right)}{\Delta z^{\#} \nabla {T_{rocks}}^{\#}}\right] / c_f \tag{2.74}$$

B - Ideal Gasses

$$\dot{w}^{\#} = (\tau_{3\to 0} - 1) \tag{2.75}$$

$$\dot{e}_x^{\#} = \left[(\tau_{3\to 0} - 1) - ln\left(\frac{\tau_{3\to 0}}{\tau_{exp}}\right)\right] \tag{2.76}$$

$$[\dot{w}_{dex_{min}},\ \dot{w}_{dex_{max}}] = \frac{\tau_{exp} - 1}{\tau_{3\to 0} - 1}\left[1,\ \frac{1}{\tau_{exp}}\right] \tag{2.77}$$

With:

$$\tau_{3\to 0} = \left(1 - \frac{\Delta z^{\#}}{{T_2}^{\#}}\right){T_2}^{\#} = 1 + \Delta z^{\#} \nabla {T_{rocks}}^{\#} - \Delta z^{\#} \tag{2.78}$$

$$\tau_{exp} = \left(1 - \frac{\Delta z^{\#}}{{T_2}^{\#}}\right)\left(1 + \Delta z^{\#}\right) = \left(1 + \Delta z^{\#} \nabla {T_{rocks}}^{\#} - \Delta z^{\#}\right)\frac{1 + \Delta z^{\#}}{1 + \Delta z^{\#} \nabla {T_{rocks}}^{\#}} \tag{2.79}$$

Substituting the latter two equations in the previous ones results in the final formulation:

$$\dot{w}^{\#} = \Delta z^{\#}\left(\nabla {T_{rocks}}^{\#} - 1\right) \tag{2.80}$$

$$\dot{e}_x^{\#} = \dot{w}^{\#} - ln\left(\frac{1 + \Delta z^{\#} \nabla {T_{rocks}}^{\#}}{1 + \Delta z^{\#}}\right) \tag{2.81}$$

$$\eta_{e_x} = \frac{\dot{e}_x}{c_f\ \dot{w}} = \left[1 - \frac{ln\left(\frac{1+\Delta z^{\#} \nabla {T_{rocks}}^{\#}}{1+\Delta z^{\#}}\right)}{\Delta z^{\#}\left(\nabla {T_{rocks}}^{\#} - 1\right)}\right] / c_f \tag{2.82}$$

$$[\dot{w}_{dex_{min}},\ \dot{w}_{dex_{max}}] = \frac{\Delta z^{\#}}{1 + \Delta z^{\#} \nabla {T_{rocks}}^{\#}}\left[1,\ \frac{1}{\tau_{exp}}\right] \tag{2.83}$$

Where the specific energy ratios has been simplified considering:

$$\frac{\tau_{exp} - 1}{\tau_{3\to 0} - 1} = \frac{\left({T_2}^{\#} - \Delta z^{\#}\right)\frac{1+\Delta z^{\#}}{{T_2}^{\#}} - 1}{{T_2}^{\#} - \Delta z^{\#} - 1} = \frac{\left({T_2}^{\#} - \Delta z^{\#}\right)\left(1 + \Delta z^{\#}\right) - {T_2}^{\#}}{{T_2}^{\#}\left({T_2}^{\#} - \Delta z^{\#} - 1\right)} \tag{2.84}$$

Which, with some analytic manipulations, results in:

$$\frac{\tau_{exp} - 1}{\tau_{3\to 0} - 1} = \frac{\cancel{{T_2}^{\#}} - \Delta z^{\#} + {T_2}^{\#}\Delta z^{\#} - {\Delta z^{\#}}^2 - \cancel{{T_2}^{\#}}}{{T_2}^{\#}\left({T_2}^{\#} - \Delta z^{\#} - 1\right)} = \frac{\Delta z^{\#}\cancel{\left({T_2}^{\#} - \Delta z^{\#} - 1\right)}}{{T_2}^{\#}\cancel{\left({T_2}^{\#} - \Delta z^{\#} - 1\right)}} \tag{2.85}$$

2.A.4 Liquid and Ideal Gas Prediction Validation

To assess the consistency of real gas behavior with ideal gas and liquid predictions, two different simulations were conducted. Ideal gas behavior has been checked setting real gas properties to those of nitrogen at ambient conditions ($c_p = 1.039$ kJ/(kg K), $T_{rel} = 2.298$, $p_{rel} = 0.03$), while for liquid-based predictions, the real gas model was integrated using the properties of water again at ambient conditions ($c_p = 4.184$ kJ/(kg K), $T_{rel} = 0.448$, $p_{rel} = 0.0046$). In both cases the calculation have been performed using REFPROP to check the consistency even of the most complex form of real gas behaviour.

The results are presented in *Fig 2.A.1* and *Fig 2.A.2*. In the case of ideal gases, there is nearly perfect agreement between the two models. In contrast, the liquid case exhibits some disagreements. This discrepancy primarily arises from the fact that no liquid is perfectly incompressible, and for smaller values of $\nabla T_{rocks}{}^{\#}$, the effect of the residual compressibility become more evident.

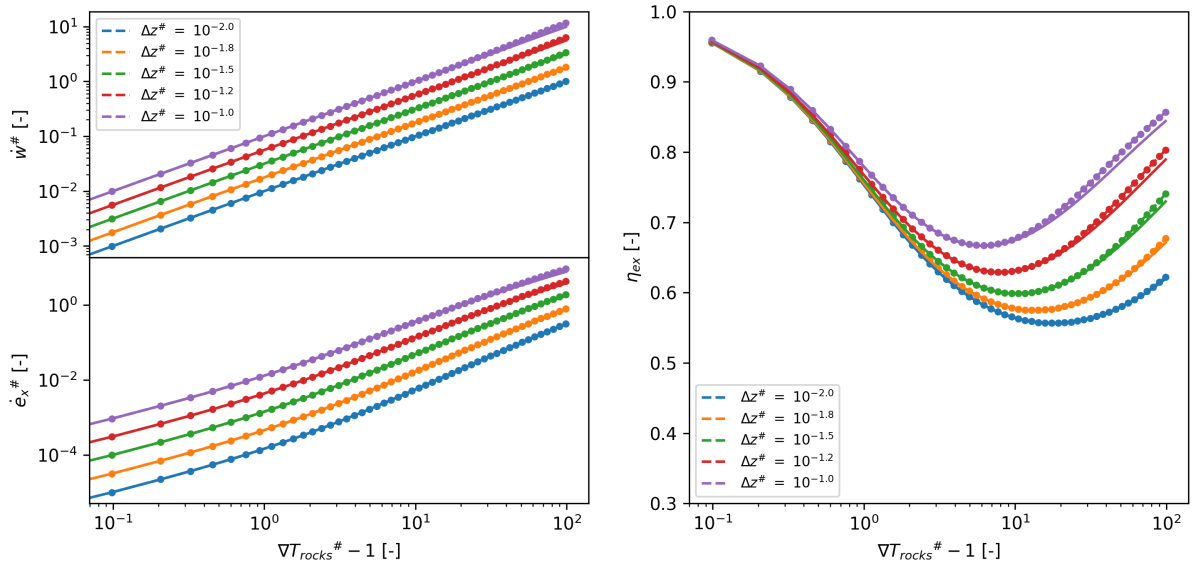

Figure 2.A.1: Comparison of nitrogen behavior, modelled with REFPROP under ambient conditions (T_{amb} = 20°C, p_0 = 1.01 bar → T_{rel} = 2.298, p_{rel} = 0.03) with ideal gas prediction. Nitrogen behavior is denoted by dots, while ideal gas behavior is represented by lines.

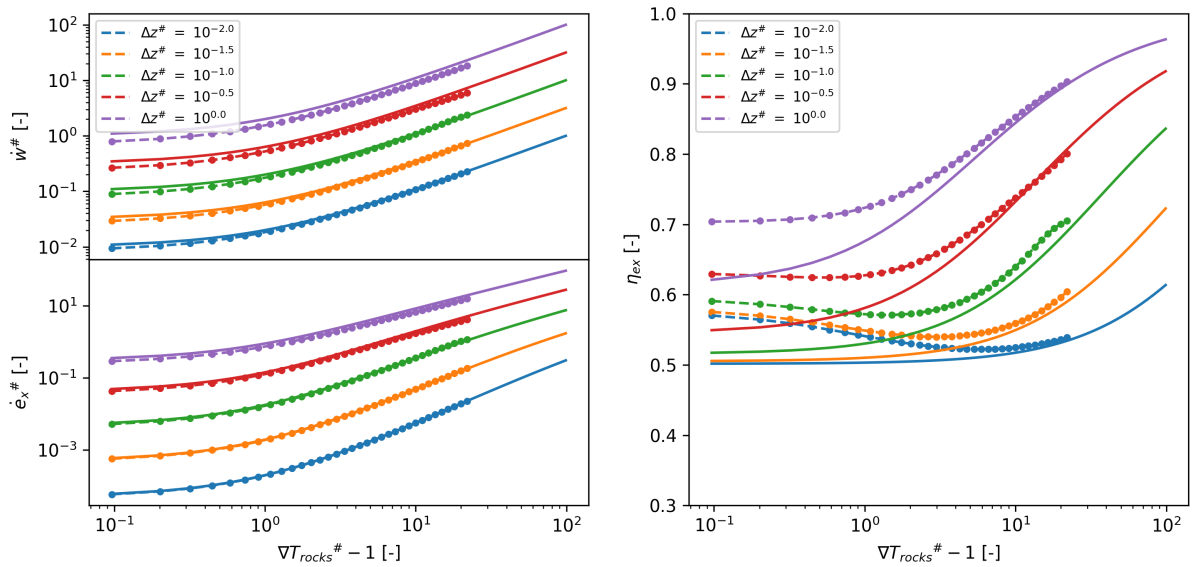

Figure 2.A.2: Comparison of water behaviour, modelled with REFPROP under ambient conditions (T_{amb} = 20°C, p_0 = 1.01 bar → T_{rel} = 0.448, p_{rel} = 0.0046) with liquid prediction. Water behavior is denoted by dots, while ideal gas behavior is represented by lines. Note that the two behaviours diverges for lower values of $\nabla T_{rocks}{}^{\#}$. REFPROP was not able to compute the results for higher values of $\nabla T_{rocks}{}^{\#}$

2.B Integration Systems Derivation

2.B.1 Ascending/Descending Section

Enthalpy and Density Relation

To properly integrate the system defined by *Eq 2.1* and *Eq 2.2* the relation between enthalpy and density has to be made explicit.
This can be done considering that:

$$dh = \left.\frac{\partial h}{\partial T}\right|_p dT + \left.\frac{\partial h}{\partial p}\right|_T dp \tag{2.86}$$

By substituting equations *Eq 2.1* and *Eq 2.2* in *Eq 2.86* and rearranging:

$$dT = -\frac{v - \left.\frac{\partial h}{\partial p}\right|_T}{\left.\frac{\partial h}{\partial T}\right|_p} \frac{g}{v} dz \tag{2.87}$$

Specific volume derivative with depth can be calculated using *Eq 2.87* starting from:

$$dv = \left.\frac{\partial v}{\partial T}\right|_p dT + \left.\frac{\partial v}{\partial p}\right|_T dp \tag{2.88}$$

Resulting in:

$$dv = -\left(\left.\frac{\partial v}{\partial T}\right|_p \frac{v - \left.\frac{\partial h}{\partial p}\right|_T}{\left.\frac{\partial h}{\partial T}\right|_p} + \left.\frac{\partial v}{\partial p}\right|_T \right) \frac{g}{v} dz \tag{2.89}$$

Specific Volume Derivative Evaluation Pressure partial derivatives are easier to compute than other ones as a generic EoS can be usually written in the form $p = f(T, v)$. For this reason is better to rewrite the specific volume partial derivatives that appears in the previous equations ($\left.\frac{\partial v}{\partial p}\right|_T$ and $\left.\frac{\partial v}{\partial T}\right|_p$) in terms of pressure partial derivatives.
For $\left.\frac{\partial v}{\partial p}\right|_T$ the substitution is straightforward as:

$$\left.\frac{\partial v}{\partial p}\right|_T = 1 / \left.\frac{\partial p}{\partial v}\right|_T \tag{2.90}$$

On the other hand, $\left.\frac{\partial v}{\partial T}\right|_p$ can be evaluate starting from:

$$dp = \left.\frac{\partial p}{\partial T}\right|_v dT + \left.\frac{\partial p}{\partial v}\right|_T dv \tag{2.91}$$

For a fixed pressure transformation $dp = 0$ and, from *Eq 2.91*:

$$\left.\frac{\partial v}{\partial T}\right|_p = -\left.\frac{\partial p}{\partial T}\right|_v / \left.\frac{\partial p}{\partial v}\right|_T \tag{2.92}$$

Reassembling *Eq 2.89*:

$$dv = \frac{1}{\left.\frac{\partial p}{\partial v}\right|_T} \left(\left.\frac{\partial p}{\partial T}\right|_v \frac{v - \left.\frac{\partial h}{\partial p}\right|_T}{\left.\frac{\partial h}{\partial T}\right|_p} - 1 \right) \frac{g}{v} dz \tag{2.93}$$

Enthalpy Derivative Evaluation

Remarks on Enthalpy definition Enthalpy derivative with pressure and temperature can be evaluated considering that, for a generic EoS, enthalpy is composed of an ideal contribute and a *departure* function [1]:

$$h = h^* + h^{dep} \tag{2.94}$$

The ideal enthalpy is function of the temperature only and can be evaluated knowing the ideal gas c_p (called c_p^*).

$$h^* = \int_{T_0}^{T} c_p^*(T)\, dT \tag{2.95}$$

Where T_0 is the reference state temperature.
On the other hand, the departure function can be evaluated through some thermodynamic consideration integrating the generic EoS from a zero-density state (where any fluid is an ideal gas) to the desired condition. [2, Chapter 4]:

$$h^{dep} = pv - R_{spc}T + \int_{\infty}^{v} \left(T \left.\frac{\partial p}{\partial T}\right|_v - p \right) dv \tag{2.96}$$

Where $R_{spc} = R/M_{molar}$ is the specific gas constant and the integral in *Eq 2.96* represent the difference in the expansion work between the ideal and real gas.

Partial derivative with respect to T and v The partial derivative of the enthalpy departure can be calculated with respect to T and v.

$$dh^{dep} = \left.\frac{\partial h^{dep}}{\partial T}\right|_v dT + \left.\frac{\partial h^{dep}}{\partial v}\right|_T dv \tag{2.97}$$

$$\left.\frac{\partial h^{dep}}{\partial T}\right|_v = v \left.\frac{\partial p}{\partial T}\right|_v - R_{spc} + \int_{\infty}^{v} T \left.\frac{\partial^2 p}{\partial T^2}\right|_v dv \tag{2.98}$$

$$\left.\frac{\partial h^{dep}}{\partial v}\right|_T = v \left.\frac{\partial p}{\partial v}\right|_T + p + \left(T \left.\frac{\partial p}{\partial T}\right|_v - p \right) = v \left.\frac{\partial p}{\partial v}\right|_T + T \left.\frac{\partial p}{\partial T}\right|_v \tag{2.99}$$

Partial derivative with respect to T and p By rewriting *Eq 2.97* using *Eq 2.88* is possible to obtain the partial derivative with respect to p and T:

$$dh^{dep} = \left.\frac{\partial h^{dep}}{\partial T}\right|_v dT + \left.\frac{\partial h^{dep}}{\partial v}\right|_T \left(\left.\frac{\partial v}{\partial T}\right|_p dT + \left.\frac{\partial v}{\partial p}\right|_T dp \right) \tag{2.100}$$

Rearranging:

$$dh^{dep} = \left(\left.\frac{\partial h^{dep}}{\partial T}\right|_v + \left.\frac{\partial h^{dep}}{\partial v}\right|_T \left.\frac{\partial v}{\partial T}\right|_p \right) dT + \left.\frac{\partial h^{dep}}{\partial v}\right|_T \left.\frac{\partial v}{\partial p}\right|_T dp \tag{2.101}$$

Resulting in:

$$\left.\frac{\partial h^{dep}}{\partial T}\right|_p = \left.\frac{\partial h^{dep}}{\partial T}\right|_v + \left.\frac{\partial h^{dep}}{\partial v}\right|_T \left.\frac{\partial v}{\partial T}\right|_p \tag{2.102}$$

$$\left.\frac{\partial h^{dep}}{\partial p}\right|_T = \left.\frac{\partial h^{dep}}{\partial v}\right|_T \left.\frac{\partial v}{\partial p}\right|_T \tag{2.103}$$

Finally, assembling together *Eq 2.94*, *Eq 2.95*, *Eq 2.98*, *Eq 2.99*, *Eq 2.102* and *Eq 2.103* is possible to obtain the final derivation for the enthalpy derivative:

$$\left.\frac{\partial h}{\partial T}\right|_p = c_p^*(T) - R_{spc} + \left(v + T \left.\frac{\partial v}{\partial T}\right|_p\right) \left.\frac{\partial p}{\partial T}\right|_v + v \left.\frac{\partial p}{\partial v}\right|_T \left.\frac{\partial v}{\partial T}\right|_p + \int_\infty^v T \left.\frac{\partial^2 p}{\partial T^2}\right|_v dv \tag{2.104}$$

$$\left.\frac{\partial h}{\partial p}\right|_T = v + T \left.\frac{\partial p}{\partial T}\right|_v \left.\frac{\partial v}{\partial p}\right|_T \tag{2.105}$$

Finally, replacing specific volume derivatives using *Eq 2.90* and *Eq 2.92*:

$$\left.\frac{\partial h}{\partial T}\right|_p = c_p^*(T) + R^\dagger - R_{spc} + \int_\infty^v T \left.\frac{\partial^2 p}{\partial T^2}\right|_v dv \tag{2.106}$$

$$\left.\frac{\partial h}{\partial p}\right|_T = v - v^\dagger \tag{2.107}$$

with $R^\dagger = v^\dagger \left.\frac{\partial p}{\partial T}\right|_v$ and $v^\dagger = -T \left.\frac{\partial p}{\partial T}\right|_v / \left.\frac{\partial p}{\partial v}\right|_T$

Final Equation

The equation presented in section 2.2.1 is found substituting *Eq 2.106* and *Eq 2.107* in *Eq 2.93*.

$$dv = \frac{1}{\left.\frac{\partial p}{\partial v}\right|_T} \left(1 - \frac{R^\dagger}{c_p}\right) dp \tag{2.108}$$

With:

$$c_p = c_p^* + R^\dagger - R_{spc} + \int_\infty^v T \left.\frac{\partial^2 p}{\partial T^2}\right|_v dv \tag{2.109}$$

And:

$$R^\dagger = -T \left(\left.\frac{\partial p}{\partial T}\right|_v\right)^2 / \left.\frac{\partial p}{\partial v}\right|_T \tag{2.110}$$

2.B.2 Iso-entropic Expansion

Once the fluid has reached the surface, the amount of work that can be extracted trough a direct expansion can be evaluate considering an iso-entropic expansion. *Eq 2.108* can be used for this purpose as and adiabatic compression is also iso-entropic.

2.B.3 Analytic relation check

To check the correctness of the analytic derivation presented here, *Eq 2.17* and *Eq 2.18* have been integrated retrieving the fluid properties with REFPROP [3]. The result have been compared with the direct integration of equations *Eq 2.1* and *Eq 2.2* which is possible using REFPROP (but not

using a generic EoS). The integration has been performed with both water and CO_2. The results, shown in *Fig 2.B.1*, prove the correctness of the derivation.

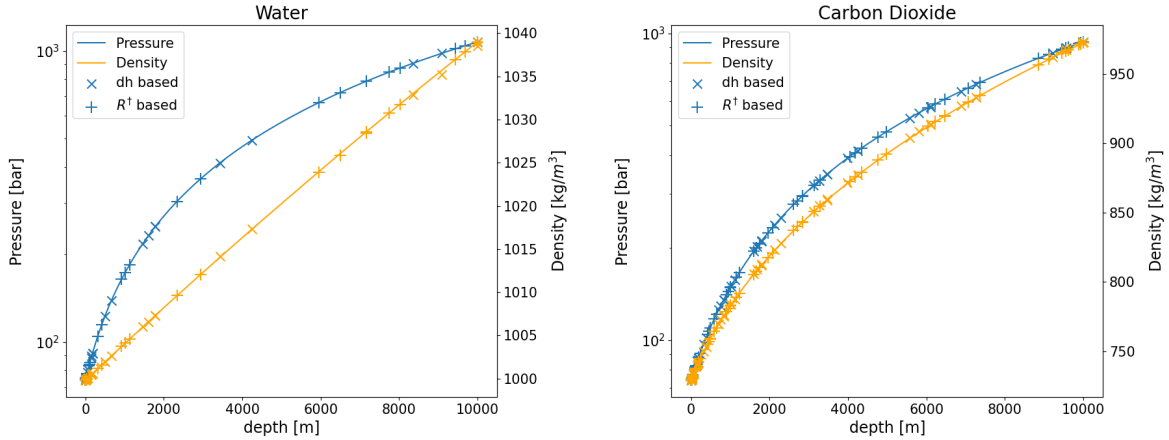

Figure 2.B.1: Analytic Relation Check: marks are calculation points for the RK integration process (x: integration based on *Eq 2.17*, +: integration based in *Eq 2.18*). lines represent the integration based directly on *Eq 2.1* and *Eq 2.2*

2.B.4 Final Remarks

Remarks on $R^\dagger$

The $R^\dagger$ presented in *Eq 2.110* is the real gas equivalent, in terms of c_p and c_v relation, of the specific gas constant R_{spc}:

$$R_{spc} = c_p^* - c_v^*; \quad R^\dagger = c_p - c_v \tag{2.111}$$

To prove this we can directly evaluate $c_p - c_v$ using the equations derived before:

$$c_p = \left.\frac{\partial h}{\partial T}\right|_p = c_p^* + R^\dagger - R_{spc} + \int_\infty^v T \left.\frac{\partial^2 p}{\partial T^2}\right|_v dv \tag{2.112}$$

Where *Eq 2.106* has been used. c_v also can be calculated from its definition:

$$c_v = \left.\frac{\partial u}{\partial T}\right|_v = \left.\frac{\partial h - pv}{\partial T}\right|_v = \left.\frac{\partial h}{\partial T}\right|_v - \left.\frac{\partial pv}{\partial T}\right|_v = \left.\frac{\partial h}{\partial T}\right|_v - v \left.\frac{\partial p}{\partial T}\right|_v \tag{2.113}$$

Which, remembering that $h = h^* + h^{dep}$ and substituting *Eq 2.99* result in:

$$c_v = \left.\frac{\partial h^*}{\partial T}\right|_v + \left.\frac{\partial h^{dep}}{\partial T}\right|_v - v \left.\frac{\partial p}{\partial T}\right|_v = c_p^* - R_{spc} + \int_\infty^v T \left.\frac{\partial^2 p}{\partial T^2}\right|_v dv \tag{2.114}$$

By combining the equations for c_p and c_v:

$$c_p - c_v = c_p^* + R^\dagger - R_{spc} + \int_\infty^v T \left.\frac{\partial^2 p}{\partial T^2}\right|_v dv - \left(c_p^* - R_{spc} + \int_\infty^v T \left.\frac{\partial^2 p}{\partial T^2}\right|_v dv\right) = R^\dagger \tag{2.115}$$

To conclude, two interesting aspects about $R^\dagger$ can be highlighted starting from its definition:

$$R^\dagger = -T \left(\left.\frac{\partial p}{\partial T}\right|_v \right)^2 / \left.\frac{\partial p}{\partial v}\right|_T \tag{2.116}$$

First of all, by substituting the **ideal gas EoS** $\left(p = \frac{R_{spc}T}{v}\right)$ in the above equation:

$$R^\dagger = -T \left(\frac{R_{spc}}{v}\right)^2 \left(-\frac{v^2}{R_{spc}T}\right) = R_{spc} \tag{2.117}$$

Hence, as expected, as long as the fluid behave like an ideal gas, $R^\dagger = R_{spc}$.
Moreover, for **incompressible fluids** $\left.\frac{\partial p}{\partial v}\right|_T \to \infty$ hence $R^\dagger \to 0$ and, again as expected, $c_p \to c_v$

Remarks on $\gamma^\dagger$

Eq 2.108 can be rewritten as:

$$dp = \left.\frac{\partial p}{\partial v}\right|_T \gamma^\dagger dv \tag{2.118}$$

Where:

$$\gamma^\dagger = \frac{1}{1 - \frac{R^\dagger}{c_p}} = \frac{c_p}{c_p - (c_p - c_v)} = \frac{c_p}{c_v} \tag{2.119}$$

Hence, as for $R^\dagger$, $\gamma^\dagger$ is the real gas equivalent of the ideal heat capacity ratio $\gamma = c_p^*/c_v^*$

2.C Equation of State Analysis

2.C.1 Introduction

In order to limit the number of parameters to be optimized a simple two or three parameters cubic EoS has been considered.
The general form of such equation of state can be summarize as [2]:

$$p = \frac{RT}{v-b} - \frac{a(T)}{(v-r_1 b)(v-r_2 b)} \tag{2.120}$$

Where $a(T)$, r_1 and r_2 depend on the selected equation of state as specified in the table below:

Table 2.C.1: Parameters for Different Cubic EoS *(adapted from [1] and [2])*

EoS	**Paremeters**	**Year**	**a(T)**	$\mathbf{r_1}$	$\mathbf{r_2}$
Van der Waals	2: a, b	1890	a	0	0
Redlich-Kwong [4]	2: a, b	1949	$a/\sqrt{T}$	0	-1
Soave	3: a, b, ω	1972	$a[1+f(\omega)(1-\sqrt{T/T_c})]^2$	0	-1
Peng-Robinson	3: a, b, ω	1976	$a[1+g(\omega)(1-\sqrt{T/T_c})]^2$	-$\sqrt{2}$-1	$\sqrt{2}$-1

Note: $f(\omega) = 0.48 + 1.574\omega - 0.176\omega^2$ — $g(\omega) = 0.37464 + 1.54226\omega - 0.26992\omega^2$.

From *Eq 2.120* is possible to evaluate the pressure derivatives and the integrals used for the evaluation of different state parameters:

Derivatives

$$\left.\frac{\partial p}{\partial T}\right|_v = \frac{R}{v-b} - \frac{1}{(v-r_1 b)(v-r_2 b)}\frac{da(T)}{dT} \tag{2.121}$$

$$\left.\frac{\partial p}{\partial v}\right|_T = -\frac{RT}{(v-b)^2} - \frac{b(r_1+r_2)-2v}{(v-r_1 b)^2(v-r_2 b)^2}a(T) \tag{2.122}$$

$$\left.\frac{\partial^2 p}{\partial T^2}\right|_v = -\frac{1}{(v-r_1 b)(v-r_2 b)}\frac{d^2 a(T)}{dT^2} \tag{2.123}$$

$$\left.\frac{\partial^2 p}{\partial v^2}\right|_T = \frac{2RT}{(v-b)^3} - \frac{(2v-b(r_1+r_2))^2 - (v-r_1 b)(v-r_2 b)}{(v-r_1 b)^3(v-r_2 b)^3}2a(T) \tag{2.124}$$

Integrals

$$\int_\infty^v \left(T\left.\frac{\partial p}{\partial T}\right|_v - p\right) dv = \left(a(T) - T\frac{da(T)}{dT}\right)\frac{ln\left(\frac{v-br_1}{v-br_2}\right)}{b(r_1-r_2)} \tag{2.125}$$

$$\int_\infty^v \left(\frac{R}{v} - \left.\frac{\partial p}{\partial T}\right|_v\right) dv = Rln\left(\frac{RT/p}{v-b}\right) + \frac{da(T)}{dT}\frac{ln\left(\frac{v-br_1}{v-br_2}\right)}{b(r_1-r_2)} \tag{2.126}$$

$$\int_\infty^v \left(\frac{RT}{v} - p\right) dv = RTln\left(\frac{RT/p}{v-b}\right) + a(T)\frac{ln\left(\frac{v-br_1}{v-br_2}\right)}{b(r_1-r_2)} \tag{2.127}$$

$$\int_{\infty}^{v} T \left.\frac{\partial^2 p}{\partial T^2}\right|_{v} dv = -T\frac{d^2 a(T)}{dT^2}\ \frac{ln\left(\frac{v-br_1}{v-br_2}\right)}{b(r_1-r_2)} \tag{2.128}$$

State Variables

From the equation above the departure function from the real gas case can be evaluate for each state variable, they have been summarized in the table below:

Table 2.C.2: State Variables for Generic Cubic EoS

State Variable	**Departure Contribution** *general formula*	*Cubic EoS Evaluation*
Internal Energy (u)	$\int_{\infty}^{v}\left(T\left.\frac{\partial p}{\partial T}\right\|_{v} - p\right) dv$	$a^{unl}(T)f(v)$
Enthalpy (h)	$u_{dep} + pv - RT$	$a^{unl}(T)f(v) + pv - RT$
Entropy (s)	$\int_{\infty}^{v}\left(\left.\frac{\partial p}{\partial T}\right\|_{v} - \frac{R}{v}\right) dv$	- $g(v) - \frac{da(T)}{dT}f(v)$
Helmholtz Energy (a)	$\int_{\infty}^{v}\left(\frac{RT}{v} - p\right) dv$	$Tg(v) + a(T)f(v)$
Gibbs Free Energy (g)	$a_{dep} - RTln\left(\frac{pv}{RT}\right) + pv - RT$	$RT\left(ln\left(\frac{RT}{p(v-b)}\right) - 1\right) + a(T)f(v) + pv$
Fugacity ($ln\varphi$)	g_{dep} / RT	$ln\left(\frac{RT}{p(v-b)}\right) + Z - 1 + \frac{a(T)}{RT}f(v)$

Note: $a^{unl}(T) = a(T) - T\frac{da(T)}{dT}$; $f(v) = ln\left(\frac{v-br_1}{v-br_2}\right)$ / $b(r_1-r_2)$; $g(v) = Rln\left(\frac{RT/p}{v-b}\right)$.

2.C.2 State Evaluation

The EoS as defined in *Eq 2.120* can be rewritten as a cubic when pressure and temperature are provided to evaluate the specific volume:

$$\boldsymbol{v^3} - \boldsymbol{v^2}\frac{b}{\beta}A_1 + \boldsymbol{v}\frac{b^2}{\beta^2}A_2 - \frac{b^3}{\beta^3}A_3 = 0 \tag{2.129}$$

Where:

$$A_1 = \beta\left(r_1 + r_2 + 1\right) + 1 \tag{2.130}$$

$$A_2 = \beta\left[\beta r_1 r_2 + \alpha + \left(r_1 + r_2\right)\left(\beta + 1\right)\right] \tag{2.131}$$

$$A_3 = \beta^2\left[r_1 r_2\left(\beta + 1\right) + \alpha\right] \tag{2.132}$$

And:

$$\alpha = \frac{a(T)}{bRT} \tag{2.133}$$

$$\beta = \frac{bP}{RT} \tag{2.134}$$

Eq 2.129 can be rewritten in terms of the compressibility factor (Z) given the relation between v and Z ($v = Z\ b/\beta$):

$$\boldsymbol{Z^3} - \boldsymbol{Z^2}A_1 + \boldsymbol{Z}A_2 - A_3 = 0 \tag{2.135}$$

Depending on the condition, *Eq 2.129* can have either one or three real roots. In case of multiple roots, the smallest and largest solution correspond to the specific volume of a liquid and a vapour state respectively, while the third root, with an intermediate specific volume, is related to an unstable state. Of the two possible stable states the one with lower Gibbs free energy (or fugacity) is the one on which the physical system will settle. If they both have the same fugacity the system is in the saturation state and the two states can coexist.

2.C.3 Saturation Condition Evaluation

Because of this, to identify the saturation pressure for a given sub-critical isotherm an iterative process is needed. The iteration process is represented in Fig. 2.C.1. To speed up the calculations a bisection method has been implemented exploiting the fact that the value of $p_r = p \ / \ p_{crit}$ is bounded between 0 and 1 for saturation pressures.

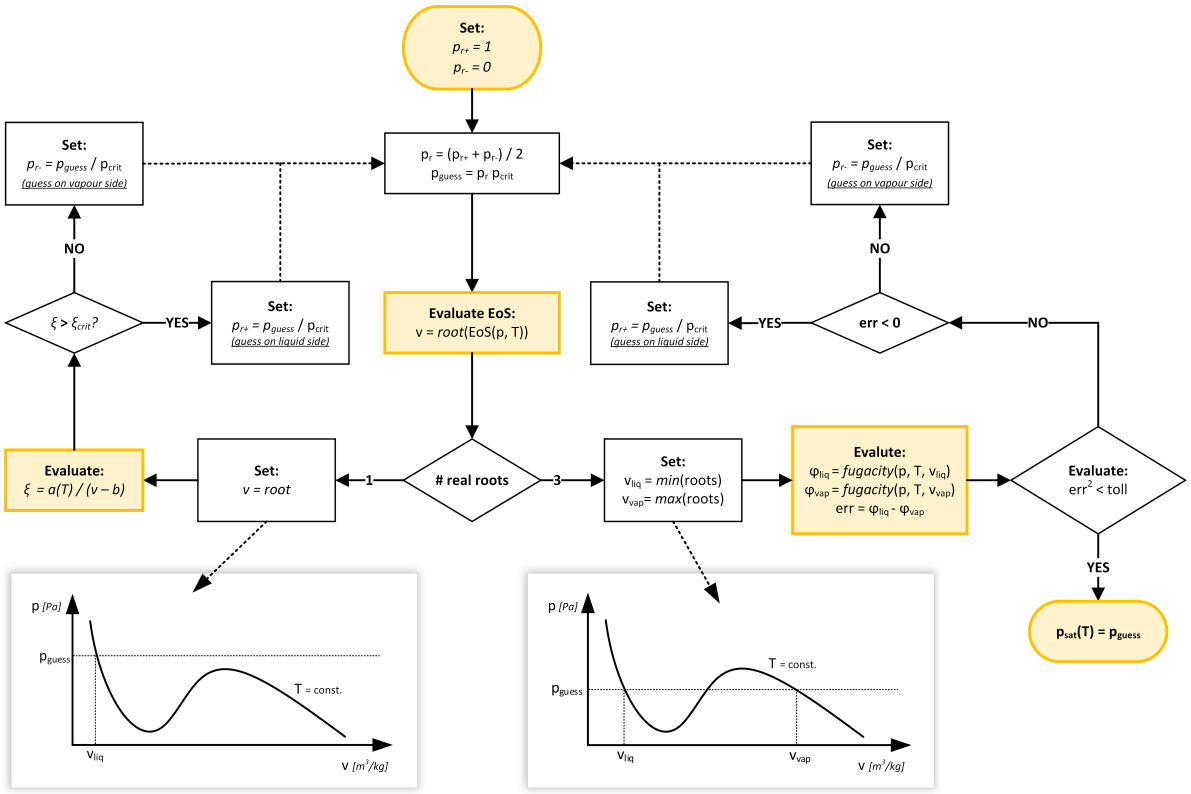

Figure 2.C.1: p_{sat} calculation procedure

As presented in *Fig 2.C.1*, if for a specific guess pressure the EoS has only one root, the parameter $\xi = a(T) \ / \ (v - b)$ has been used to discern between the liquid and the vapour phase. In fact, ξ can be seen as the relative strength of the attraction and repulsion molecular forces in the EoS. In liquid phase the repulsion forces dominates, hence ξ will reach very high values, while in vapour phase ξ will tends to zero. The critical condition is the one in which the two molecular forces balance out and hence it has been used as a reference.

The identification of the saturation condition is needed for the estimation of pressure or temperature given the specific volume and is one of the slowest process in the state evaluation. To further speed up the calculation, a polynomial interpolation has been used to predict the saturation condition without the need of an iterative process. The iteration is then repeated only for states whose volume

is within the interval $[0.98v_{liq}, 1.02v_{vap}]$ that consider a 2% tolerance to account for the accuracy of the polynomial interpolation.

2.C.4 Comparison with REFPROP

To assess the error associated with the application of a cubic EoS in the system integration, the EoS-derived results were compared to the state variables obtained from REFPROP [3], a widely recognized benchmark in the literature, for two simple fluids (CO_2 and methane). The results of the comparison is shown in the following figures. From them, it is possible to derive the following takeaways:

- A two-parameter EoS can not precisely predict the saturation pressure of different substances, while, for simple fluids, three parameter EoS appears to be accurate enough. *(reference to Fig 2.C.2)*
- Three parameter EoS appears to be accurate enough also in the prediction of other variable of state (enthalpy and entropy). *(reference to Fig 2.C.3)*
- All of the selected EoS fail to accurately replicate the profile of $R^\dagger/c_p$, particularly in the high-density supercritical regions. This presents a concern as this parameter plays a crucial role in the integration of the vertical sections (refer to *Eq 2.18*). Nevertheless, each EoS considered is able to capture the general trend of $R^\dagger/c_p$. This implies that while they may not provide precise evaluations, they can still be employed for a *qualitative* analysis of the system's behavior with real fluids. *(reference to Fig 2.C.4)*

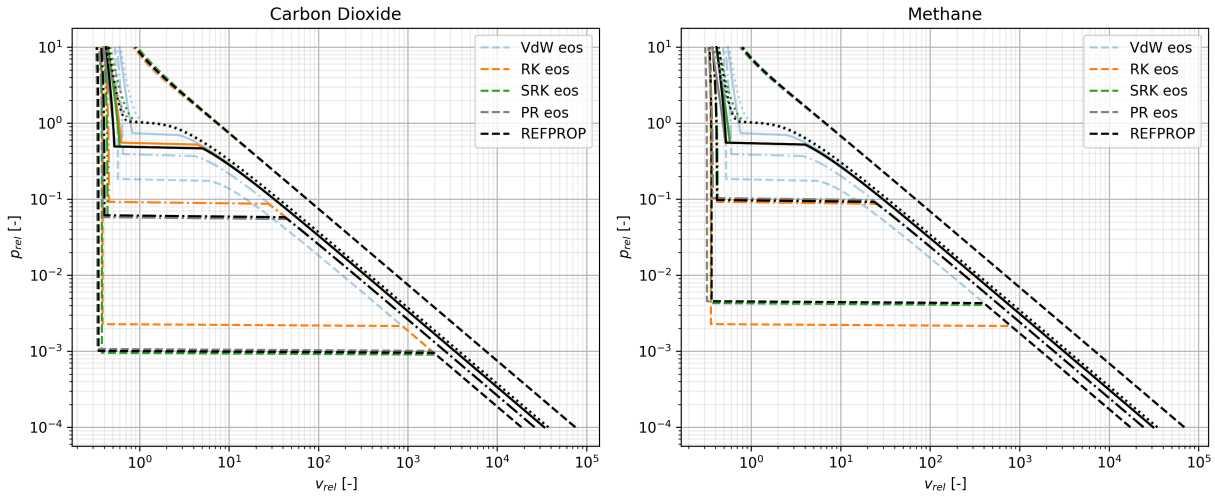

Figure 2.C.2: $p-v$ relationship prediction for different EoS, *Observe that two-parameter EoS are unable to precisely predict the saturation pressure, as it varies among different substances. The Redlich-Kwong EoS, for instance, tends to provide an approximation close to the mean value. The introduction of the acentric factor (ω) enables the assignment of distinct saturation pressures to different fluids.*

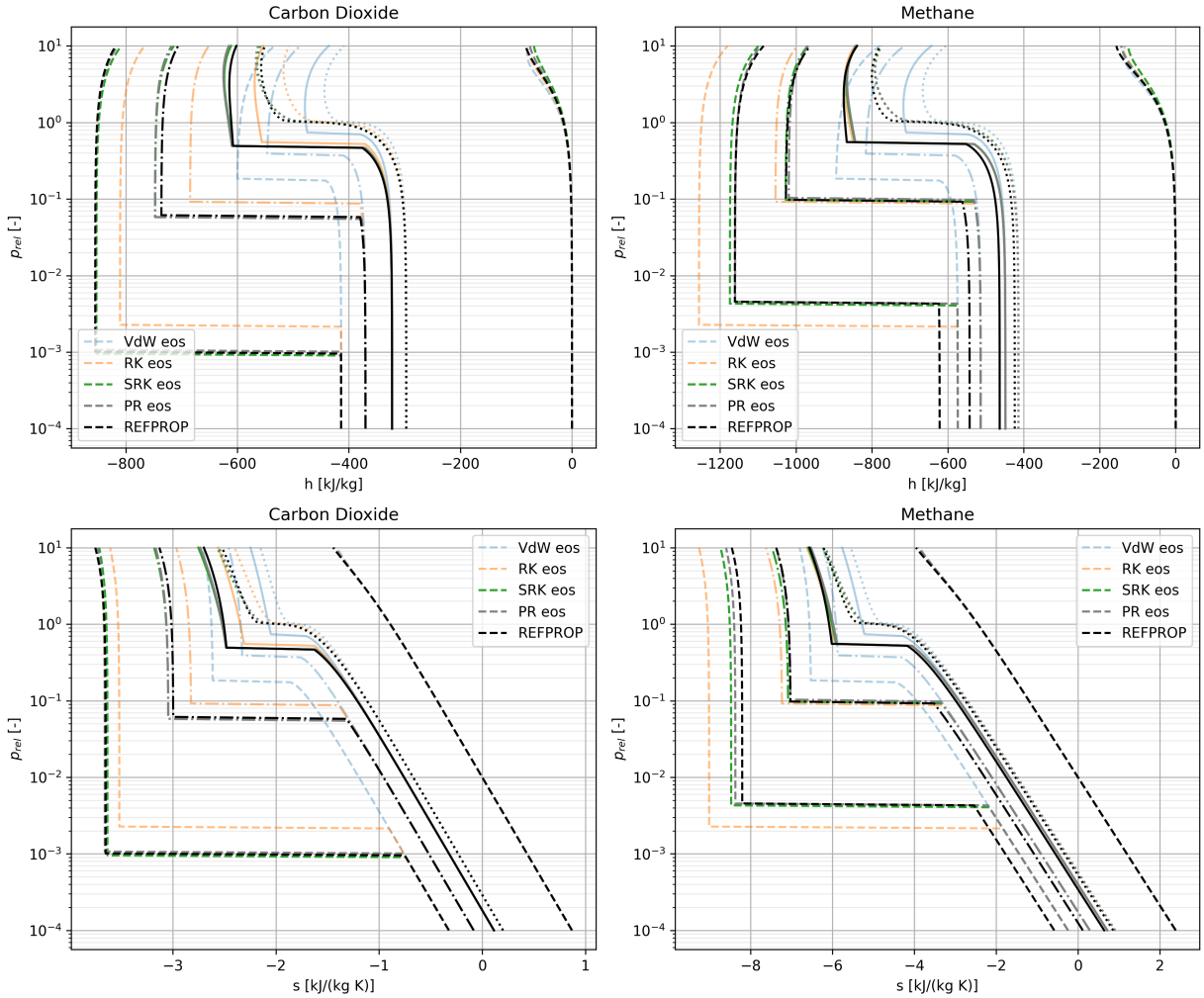

Figure 2.C.3: $p-h$ and $p-s$ relationship prediction for different EoS

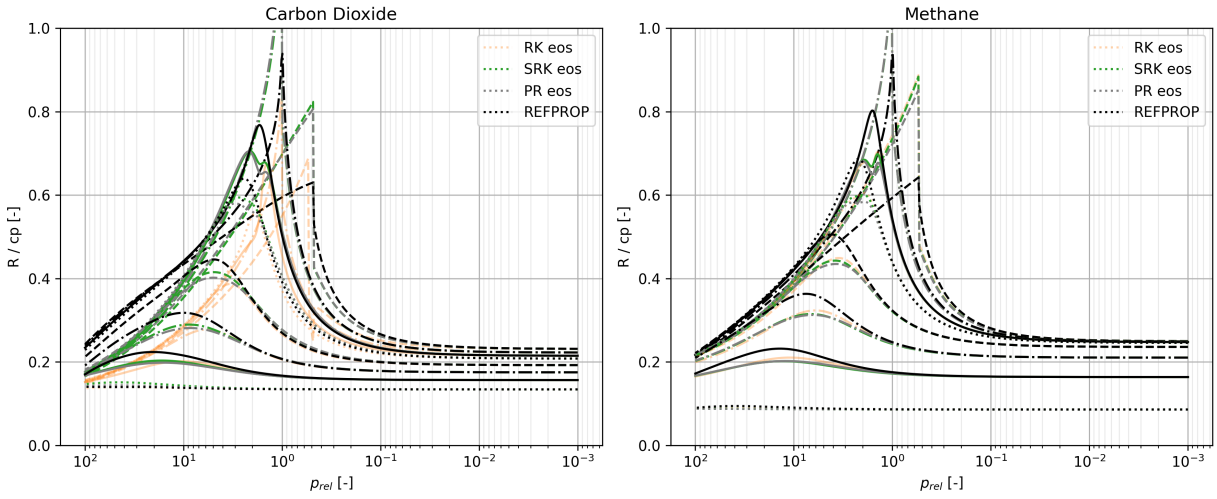

Figure 2.C.4: $R^{\dagger}/c_p$ profile prediction for different EoS: *Note that, once again, the Redlich-Kwong EoS cannot adapt to different fluids due to the absence of an additional parameter. However, as evident from the methane case, it is still capable of capturing the general trend of $R^{\dagger}/c_p$ indicating its utility in retrieving general characteristics. Meanwhile, the Peng-Robinson EoS can be employed to investigate the impact of the acentric factor.*

2.C.5 Final Remarks on c_p modelling

As for any other thermodynamic variables c_p can be evaluated as composed of an ideal part c_p^* and a departure function $c_{p_{dep}}$. The departure function can be easily evaluated from the real fluid EoS, starting from *Eq 2.109*:

$$c_{p_{dep}} = R^\dagger - R + \int_\infty^v T \left.\frac{\partial^2 p}{\partial T^2}\right|_v dv = R^\dagger - R + \left(a(T) - T\frac{da(T)}{dT}\right) ln\left(\frac{v - br_1}{v - br_2}\right) \tag{2.136}$$

On the other hand c_p^* in general depends on temperature but this dependence arise from the quantistic behaviour of the molecules composing the fluid. In fact, as the temperature increase more and more vibrational states can be excited increasing c_p^*. Unfortunately this behaviour cannot be linked with other thermodynamic properties, such as the critical pressure and temperature, as these properties arise from the forces of interaction between molecules not from the behaviour of the molecules themself.
All in all this means that no general trend can be identified that is suitable for any fluid, but fluid-specific parameters must be considered in the correlation for c_p^*. In literature empirical polynomial interpolation is often used for evaluating c_p^* [1], [2]:

$$c_p^* = a + bT + cT^2 + dT^3 + eT^4 + ... \tag{2.137}$$

The formula above with the coefficients retrieved from [1], has been used for the validation process (*Fig 2.C.3* and *Fig 2.C.4*) while during the evaluation of the behaviour of the well c_p^* has been considered as constant in order to prevent fluid dependent behaviour from emerging.

References

[1] B. E. Poling, J. M. Prausnitz, and J. P. O'Connell, *Properties of Gases and Liquids*, en, 5th Editio. New York: McGraw-Hill Education, 2001, ISBN: 9780070116825.

[2] J. Vidal, *Thermodynamics: Applications in Chemical Engineering and the Petroleum Industry* (Institut français du pétrole publications). Editions Technip, 2003, ISBN: 9782710808008.

[3] E. W. Lemmon, I. H. Bell, M. L. Huber, and M. O. McLinden, *NIST Standard Reference Database 23: Reference Fluid Thermodynamic and Transport Properties-REFPROP, Version 10.0, National Institute of Standards and Technology*, 2018.

[4] O. Redlich and J. N. S. Kwong, "On the Thermodynamics of Solutions. V. An Equation of State. Fugacities of Gaseous Solutions.," *Chemical Reviews*, vol. 44, no. 1, pp. 233–244, Feb. 1949, ISSN: 0009-2665. DOI: 10.1021/cr60137a013.

Chapter 3

Detailed Well Model

3.1 Introduction

In order to conduct a more in-depth analysis of the behavior exhibited by CO_2 based geothermal systems, a more comprehensive model, capable of predicting the behaviour of system with different configurations and geometries, has been developed.
Numerous models of various systems involving both water and CO_2 can be found in literature. They can be divided according to the geothermal system type as different system configuration implies different modelling challenges.

3.1.1 Open Systems (Traditional Geothermal Systems, CPG or EGS)

In a traditional geothermal system the working fluid is circulated in the reservoir in direct contact with the hot rocks to increase the heat transfer capabilities. For this reason the most complex element of the system, from a modelling perspective, is the reservoir.

Reservoir Modelling

A detailed reservoir modelling, requires a deep knowledge of the geology of the selected location (permeability, fractures pattern and orientation, etc.) which in many case is unknown. Such analysis are usually performed with dedicated software (such as TOUGH [1] or other in-house developed tools [2], [3]). The use of these software tools enables the analysis of intricate problems such as the effect of CO_2 dissolution in the reservoir water for CPG systems [4] or the forecasting of reservoir evolution based on chemical interaction between the rocks and the brine [5].
For analysis that does not requires this level of details simple analytical correlation are implemented to obtain an approximation of the behaviour of the reservoir with a fraction of the computational time. In most of the cases, an equation describing the flow of a fluid in a porous media (such as the Darcy or the Peaceman [6] equation, depending on the geometry) is used to evaluate the pressure drop [7]–[10]. The outlet temperature is usually fixed (considered to be equal to the undisturbed rock temperature) [7], [10], or evaluated together with the pressure drop considering a simple correlation for the heat transfer between the fluid and the rocks [8].

Injection and Production wells

The flow in the well is usually solved considering using a 1D incompressible Navier-Stokes equation for the dynamics fluid inside the well [1], [7]–[10]. Only under specific circumstances, specifically in vapor-dominated traditional geothermal systems, does the fluid within the well have the potential to reach a choking condition. This implies the necessity to reject the hypothesis of incompressibility. Some researchers in the 70s and the 80s have developed detailed models for this condition [11]–[13]. These models have been abandoned in recent years because vapor-dominated geothermal reservoirs are very rare and those that exist have already been exploited limiting the need for well modeling in those conditions.

3.1.2 Closed Systems (BHE Systems)

Because of the absence of a direct interaction between the fluid and the rocks, closed systems are usually easier to model. The fluid inside the well is again solved with a 1D approach as for the open systems [14]–[16]. The main modelling difficulties reside in the prediction of the temperature distribution around the well. Some researcher directly couples the fluid flow solution with a 2D finite difference evaluation of the heat transfer in the rock formation [15], while others have used some correlations [14], [16].
Multiple correlation for the heat transfer in rock formation has been developed trough-out the years [17]–[19]. Moreover, Zang et al. have proposed a time convolution approach for the evaluation of heat transfer in unsteady flow condition [20].

3.1.3 Economic Considerations

Multiple correlation has been developed for the estimation of the drilling cost of a geothermal well. In recent year, Adamns et al. have conducted a systematic literature analysis and proposed revised correlation in the scope of the genGEO tool that they have developed [21].

3.2 Models Description

The detailed model is an extension of the base theoretical model described in *Chapter 2* and it maintains the same 3 sections structure described in *Paragraph 2.2.1* and shown in *Fig 3.1.*

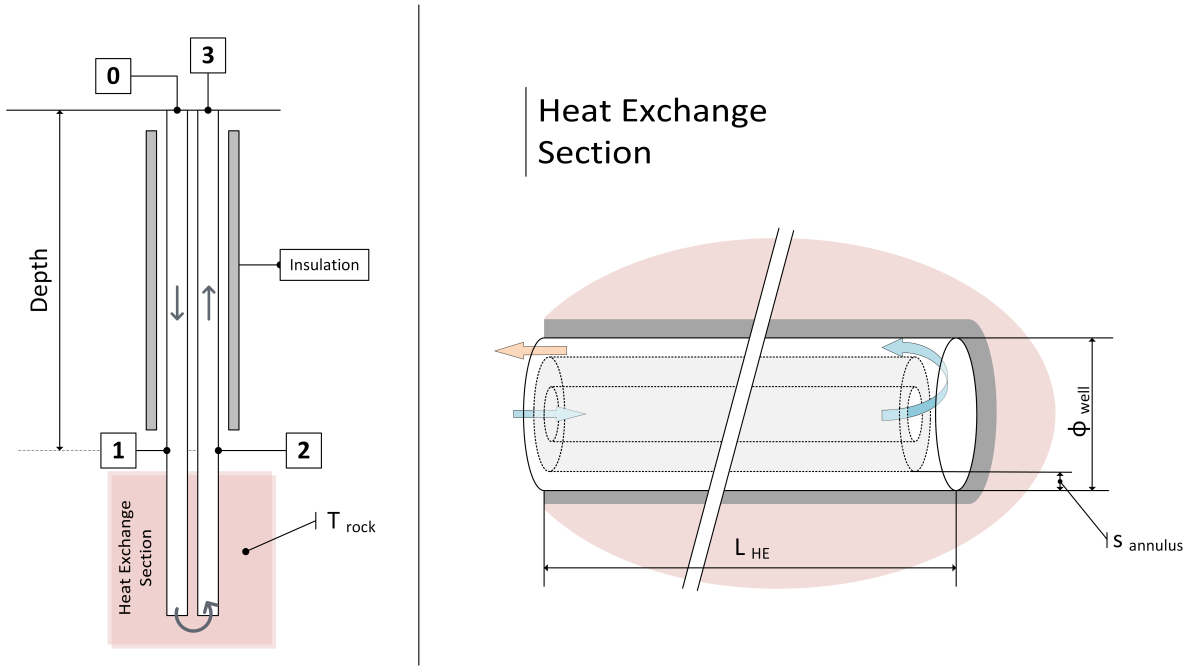

Figure 3.1: General Model Scheme, on the right an example of a possible heat exchange section for a concentric *BHE*

The base model has been extended in order to reproduce the behaviour of the different system configurations and well geometries with various level of details.
In describing the new model. The discussion will start by introducing correlations that apply to all geometries (*Paragraph 3.2.1*) and describing the base solution algorithm (*Paragraph 3.2.2*), providing a foundational basis for our analysis. After that, the detailed modeling of specific system configurations will be presented.

3.2.1 General Correlations

Unlike the simplified model, the fluid properties and derivatives have been **directly retrieved with REFPROP** [22]. Moreover, the momentum and energy balance equations for the vertical sections have been extended as follows to account for the pressure losses (dp_{loss}), the non adiabaticity of the flow ($d\dot{q}_{tot}$), and the inclination (θ) of the well:

$$\frac{dp}{dl} = -\left(\rho g cos\theta \ + dp_{loss}\right) \tag{3.1}$$

$$\frac{dh}{dl} = -\left(g cos\theta \ - d\dot{q}_{tot}/\dot{m}_{well}\right) \tag{3.2}$$

Again, as already explained in *Chapter 2*, density has been used in the integration process instead of enthalpy:

$$d\rho = \left(\left.\frac{\partial \rho}{\partial p}\right|_T + \left.\frac{\partial \rho}{\partial T}\right|_p \frac{\frac{dh}{dp} - \left.\frac{\partial h}{\partial p}\right|_T}{\left.\frac{\partial h}{\partial T}\right|_p} \right) \frac{dp}{dl} \tag{3.3}$$

Where $\frac{\partial \rho}{\partial p}\Big|_T$, $\frac{\partial \rho}{\partial T}\Big|_p$, $\frac{\partial h}{\partial p}\Big|_T$ and $\frac{\partial h}{\partial T}\Big|_p$ can be directly evaluated using REFPROP and $\frac{dh}{dp} = \frac{dh}{dl} \ / \ \frac{dp}{dl}$. The need for this substitution emerged because of a numerical issue showing up in some specific condition and related to the fact that, because of the Jules-Thomson effect, enthalpy and pressure may not be enough to uniquely identify the state of the fluid (two different states with the same enthalpy and temperature may exist).
The system composed of *Eq 3.1* and of *Eq 3.3* has been integrated in python using a explicit 5th order Runge-Kutta method [23] as implemented in the SciPy python package [24].

Pressure Losses

The pressure losses are evaluated using the Churchill correlation [25] for the friction factor:

$$dp_{loss} = f \frac{1}{2\rho d_h} \left(\frac{\dot{m}_{well}}{A_{flow}} \right)^2 \tag{3.4}$$

Where A_{flow} is the cross-sectional area of the flow, and d_h is the hydraulic diameter of the considered pipe section. The friction factor f is calculated as follow as function of the Reynolds Number (Re), the surface roughness of the pipe (ε), and the hydraulic diameter:

$$f = 8 \left(\left(\frac{8}{Re} \right)^{12} + \left(\frac{1}{A^\star + B^\star} \right)^{3/2} \right)^{1/12} \tag{3.5}$$

$$A^\star = \left(2.457 ln \left(\frac{1}{\left(\frac{7}{Re}\right)^{9/10} + 0.27 \frac{\varepsilon}{d_h}} \right) \right)^{16} \tag{3.6}$$

$$B^\star = \left(\frac{37530}{Re} \right)^{16} \tag{3.7}$$

Heat Transfer

The evaluation of $d\dot{q}_{tot}$ is much more dependent on the geometry of the well. Two specific correlation have been used more frequently:

Fluid Convection In general, when needed, a simple correlation for Nusselt Number (Nu) is applied for convection heat transfer evaluation:

$$Nu = 0.023 Re^{0.8} Pr^{0.4} \tag{3.8}$$

Eq 3.8 can lead to important error in the estimation of the heat transfer coefficient when dealing with particular condition such as the heat transfer of trans-critical CO_2 .
Anyway the impact of this error is usually marginal because conductive resistance (such as the one inside the rocks formation around the well) within these systems is often of prevailing.

Conduction in Rocks To account for heat transfer in rocks formation around the well without having to solve a finite difference model of the temperature distribution in the surrounding, a semi-

analytical correlation has been implemented as defined in a paper autored by Zhang et al. [20]:

$$R_{rocks} = \frac{d_{well}}{2k_{rocks}f(t_d)} \tag{3.9}$$

with:

$$f(t_d)_{base} = \begin{cases} \frac{1}{2} + (\pi t_d)^{-\frac{1}{2}} - \frac{1}{4}\left(\frac{t_d}{\pi}\right)^{\frac{1}{2}} + \frac{1}{8}t_d, & \text{if } t_d < 2.8 \\ \frac{2}{ln(4t_d)-2\gamma} - \frac{2\gamma}{(ln(4t_d)-2\gamma)^2}, & \text{if } t_d \geq 2.8 \end{cases} \tag{3.10}$$

Where, in *Eq 3.10*:

- $t_d = 4\alpha_{rocks}t/d_{well}^2$ is a dimensionless time (t in seconds)
- $\alpha_{rocks} = k_{rocks}/\rho_{rocks}C_{p_{rocks}}$ is the thermal diffusivity of the rocks
- γ is Euler's constant
- d_{well} is the external diameter of the well

In the scope of this thesis, *Eq 3.9* has been validated and expanded to account for the impact of the geothermal gradient and the presence of a fluid circulating within the reservoir's porosity, moving around the well. The validation process involved conducting Finite Element Method (FEM) simulations, the detailed procedure of which is outlined in Appendix 3.A. The effects of the geothermal gradient and fluid flow are integrated using two dimensionless modifiers, as follows:

$$f(t_d) = max(f(t_d)_{base} + df_{grad}, f_s) \tag{3.11}$$

With:

$$df_{grad} = 1.396\ 10^{-3}\ \nabla T_{rocksd} \tag{3.12}$$

And:

$$log_{10}(f_s) = 0.35(log_{10}(Pe))^2 + 0.081log_{10}(Pe) - 0.302 \tag{3.13}$$

Where $\nabla T_{rocksd} = d_{well}\nabla T_{rocks}/\Delta T_\infty$ is an adimensionalization of the geothermal gradient and $Pe = d_{well} \mid \vec{v} \mid /\alpha_{rocks}$ is the *Peclet number* associated with the fluid flowing around the well.
Eq 3.11 can be directly used to retrieve thermal resistance in case of stationary flow. On the other hand, if a significant fluctuation of the flow rate in the well is expected, a convolution approach can be used to estimate the evolution over time of the temperatures around the well [20]:

$$\dot{q}_{tot} = \sum_{t=1}^{d-1} \frac{2k_{rocks}}{d_{well}} f(t_d - t_i)\Delta T_\infty(t_i) \tag{3.14}$$

Where t_i and $\Delta T_\infty(t_i)$ are the dimensionless time after i time steps. *Eq 3.14* has to be used carefully because it has been developed in the scope of the modelling of geothermal storage systems, meaning that in usual operation the system is recharged injecting hot water in the well, or, from a mathematical perspective, changing the sign of $\Delta T_\infty(t_i)$. This means that *Eq 3.14* will model correctly only situations in which the flux from the reservoir fluctuate but never stops.

3.2.2 General Solution Procedure

Two possible solution procedures can be implemented depending on weather the system is pressurized by an external reservoir (referred to as *Open Systems*) or if its insulated by the environment (*Closed System*). Refer to the previous chapter of a more detailed explanation (*Paragraph 2.2.1*). The two solution methods are described in *Fig 3.2*.

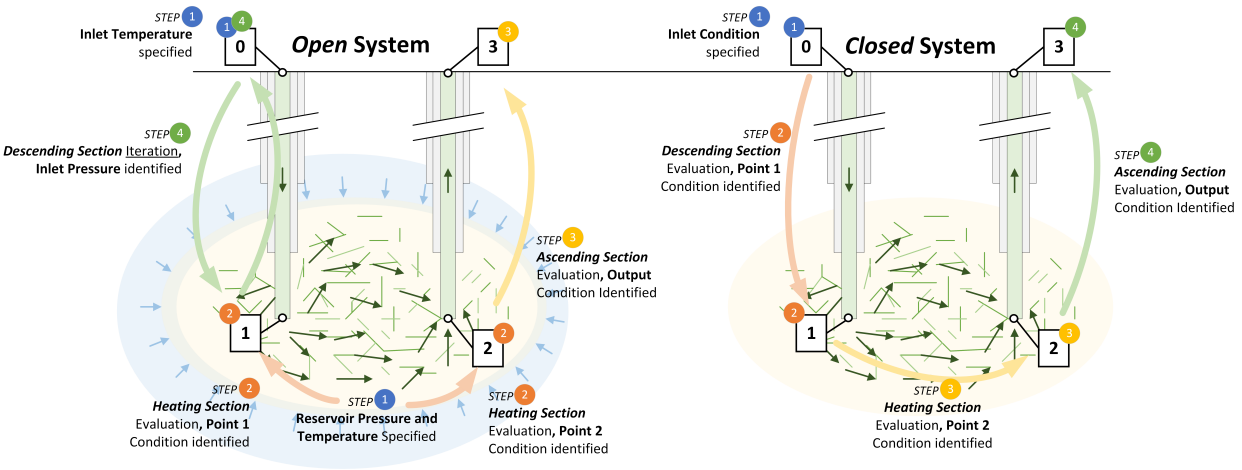

Figure 3.2: Solution procedure description: On the *left*, algorithm for externally pressurized systems (i.e. traditional geothermal systems or CPG). On the *right*, solution algorithm for systems not externally pressurized (such as EGS, BHE).

As shown in the figure, for *Closed Systems* the solution is straight-forward as the inlet condition are known and the system can be integrated solving the various sections in sequence.
On the other hand, for *Open Systems*, one between the inlet pressure or flow rate must be evaluated starting from the external pressure compressing the CO_2 enriched area. In order to do so the *descending section* evaluation has to be iterated until a solution is reached. After that, the *ascending section* can be integrated in order to evaluate the outlet condition.

3.2.3 Detailed Model for Different Geometries

No Geometry

As already explained in *Chapter 2* the simplest well model can be drafted with only two geometrical parameter, the reservoir depth (Δz_{well}) and temperature (T_{rocks}), which can be evaluated from the geothermal gradient (∇T_{rocks}). With these two parameters the model of the well can be drafted considering that the no pressure losses will be present in the heating section and that the temperature at the inlet of the production well will be equal to the rocks temperature.

Traditional Systems Reservoir

In modelling the *heating section* of traditional systems, in which the fluid is in direct contact with the hot rocks, a 1D Darcy flow has been considered as proposed by many researcher in literature [26], [27]:

$$\begin{aligned} p_1 &= p_{res} - \dot{m}\frac{\mu}{\rho}\left[\frac{L}{\kappa A}\right]_{res} \\ p_2 &= p_{res} \end{aligned} \tag{3.15}$$

Where $\left[\frac{L}{\kappa A}\right]_{res}$ is a parameter depending on the reservoir dimensions (L and A) and permeability (κ), and $p_{res} = g\Delta z_{well}\rho_{H_2O}$ is the undisturbed reservoir pressure.
As suggested by Adams et al. [28] the *average specific inverse mobility* $M = \frac{\mu}{\rho}\left[\frac{L}{\kappa A}\right]_{res}$ can be used to simplify reservoir pressure losses evaluation.
If water or CO_2 are used as working fluid, is possible to directly use the value of M that they have retrieved from some TOUGH2 simulations based on standard Five-spot geometry presented by Pruess [1].
In water based reservoir, the mobility is strongly influenced by reservoir temperature due to the significant influence that temperature has on water viscosity. Because of this, a simple power correlation can be inferred from the data presented in [28]:

$$M = 4600\ {T_{rocks}}^{-0.77} \tag{3.16}$$

On the other hand, for CO_2 based system the mobility is almost constant and can be approximated as $M = 23.5$ (kPa s)/kg.

BHE wells

In literature there are mainly two different geometries of BHE wells, shown in *Fig 3.3*.

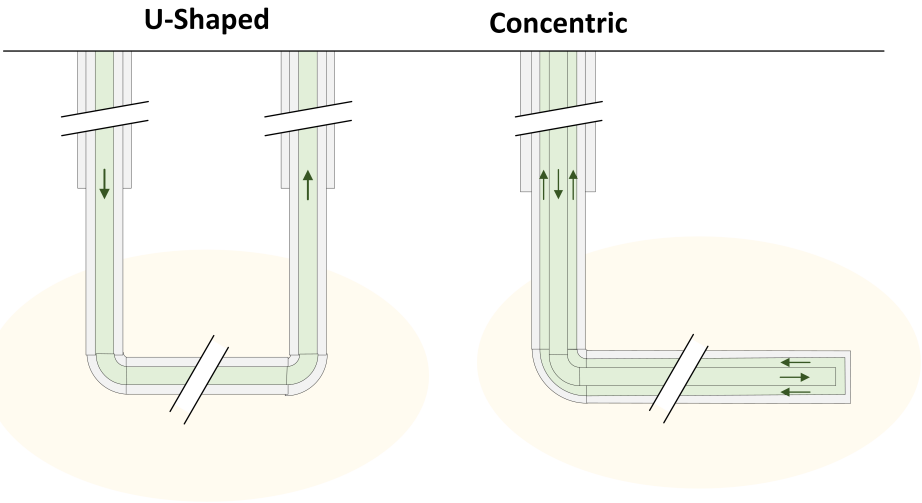

Figure 3.3: Different geometries for BHE wells

A - *U-shaped* well

The U-shape geometry make its modeling relatively simple: *Eq 3.1* and *Eq 3.3* can be integrated trough-out the entire length of the well using *Eq 3.4* and *Eq 3.9* for the evaluation of pressure losses and rocks heat transfer. Even more complex geometries, such as the one described by Adams et al. [16], can be modelled with these set of relations.

B - *Concentric* well

For concentric BHE geometries, the calculation is made more complex by the need of considering internal heat transfer between the descending and ascending sections.
In general also in this case *Eq 3.1* and *Eq 3.3* can be integrated trough-out the entire length of the well. The only difference with the previous case is in the evaluation of $d\dot{q}_{tot}$:

$$d\dot{q}_{tot} = d\dot{q}_{rocks} + d\dot{q}_{int} \tag{3.17}$$

with:

$$d\dot{q}_{int} = \frac{1}{R_{int}} \Delta T_{int} \tag{3.18}$$

and:

$$R_{int} = \frac{1}{d_{tub_{ext}} h_{ann_{int}}} + \frac{ln\left(\frac{d_{tub_{ext}}}{d_{tub_{int}}}\right)}{2\pi k_{ins}} + \frac{1}{d_{tub_{int}} h_{tub}} \tag{3.19}$$

where $d_{tub_{int}}$ and $d_{tub_{ext}}$ are the inner an outer diameter of the internal tubing, k_{ins} it the thermal conductivity of the tubing itself and $h_{ann_{int}}$ and h_{tub} are the convective heat transfer coefficient for the flow in the annulus and in the tubing respectively, evaluated form *Eq 3.8*. Unfortunately, the temperature distribution in both the annulus and the tubing is needed to evaluate ΔT_{int} and hence *Eq 3.18*. For this reason an iterative approach has been developed.
To solve the system, the code will store in memory the pressure and density profile of the fluid along the well for each iteration. $d\dot{q}_{int}$ is then evaluated using the old profiles as follows:

$$d\dot{q}_{int} = \frac{\sum_{i=0}^{n_{old}} {\alpha_{old}}^i d\dot{q}_{int}(i)}{\sum_{i=0}^{n_{old}} {\alpha_{old}}^i} = \frac{1-\alpha_{old}}{1-{\alpha_{old}}^{(n_{old}+1)}} \sum_{i=0}^{n_{old}} {\alpha_{old}}^i d\dot{q}_{int}(i) \tag{3.20}$$

Where $d\dot{q}_{int}(i)$ is the internal heat transfer evaluated considering the condition of the well as evaluated i iteration before.
n_{old} and α_{old} are two parameter which can be used for speeding up the iteration process. n_{old} controls how many old profiles will be stored in memory and used for evaluating $d\dot{q}_{int}$, while α_{old} controls how much the influence of old profile decline as new iteration are evaluated. In our calculation $n_{old} = 5$ and $\alpha_{old} = 0.5$ has been used.
The iteration is automatically initialize by setting up the code so that it considers $d\dot{q}_{int}(i) = 0$ if the code has not reached the *i-th* iteration. This means that in the first iteration $d\dot{q}_{int} = 0$, hence the internal heat transfer is neglected. In the following iterations the effect of the internal heat transfer gradually kicks in as more and more $d\dot{q}_{int}(i)$ can be calculated as the number of stored profiles increase. The iteration continues until the *pressure*, *density* and *temperature* profiles in the well stabilize. The stabilization is checked in 100 points equally distributed along the well.

3.2.4 Remarks on cost correlations

For drilling cost estimation, the correlation developed by Adams et. al. for the *GenGEO tool* [21] has been used:

$$c_{well} = X_{IC-well} X_{PC-well} PPI_{O\&G} \left(0.105 L_{well}^2 + 1776 L_{well} d_{well} + 2.753 * 10^5\right) \tag{3.21}$$

Where $L_{well}$is the overall length of the well and d_{well} is the outer diameter of the well (both in m). The value of the other parameters is fixed and reported in the table below:

Table 3.1: Well drilling cost correlation parameters

Parameter	Description	Value
$X_{PC-well}$	Contingency cost increase (supposed 15%)	1,15
$X_{IC-well}$	Indirect cost increase (supposed 5%)	1,05
$PPI_{O\&G}$	Inflation adjustment based on the oil and gas Producer Price Index [29] (reference is 2002 – the value shown is the correction factor for January 2022)	2,86

The proposed correlation considers also a cost increase for wells that are designed to be used with sCO_2 due to the characteristic of the fluid itself (usage of corrosion resistance materials, higher pressure requirements, etc.):

$$\Delta c_{CO2} = X_{IC-well} X_{PC-well} PPI_{O\&G} \left(133 L_{well} + 256 L_{well} d_{well}\right) \tag{3.22}$$

The overall cost will be then computed as:

$$c_{welltot} = \frac{c_{well}}{s_{well}} + \Delta c_{CO2} \tag{3.23}$$

s_{well}, that shows up in *Eq 3.23*, is the success rate of the well drilling. It considers the possibility that the well does not meet the expected performances after the drilling is completed or that something goes wrong in the drilling process and the well has to be abandoned. This is a critical parameter for traditional geothermal system for which, according to some studies [21], the success rate should be around 75%. For BHE and EGS systems this value is expected to be much higher as the behaviour of the well is less dependent on the physical properties of the reservoir. For that reason, in this initial analysis an arbitrary value of 0.90 has been selected.
To conclude is important to point out that the correlation just described has been developed considering high depth and high temperature well drilling for power generation purpose. Such well are usually drilled with heavy rig derived from the oil and gas industry. For our application could not be necessary to reach such high temperature and depth hence it can be possible in some cases to use lighter drilling equipment reducing the drilling costs consequently (*Fig 3.4* should clarify this concept).

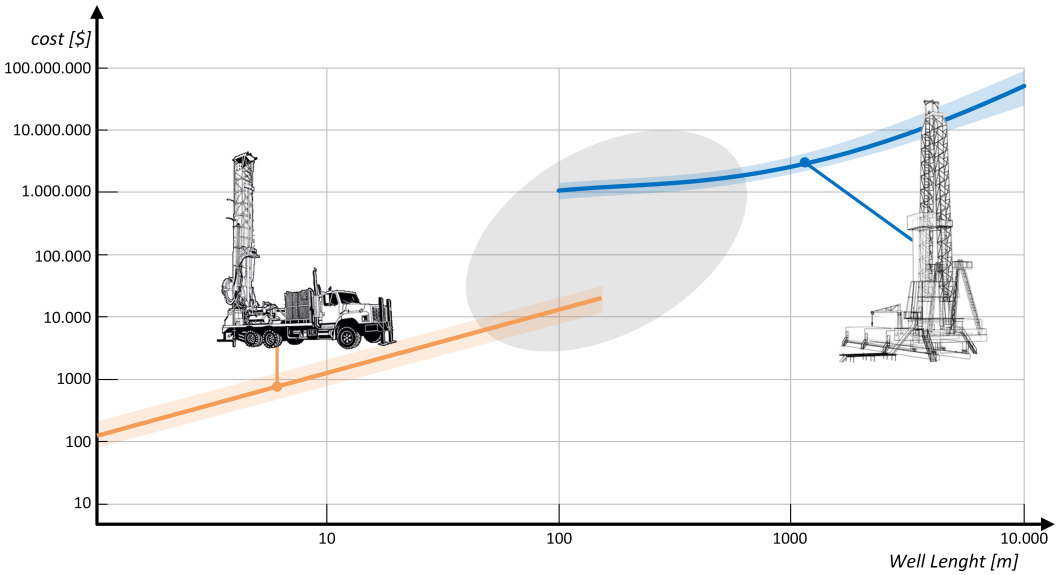

Figure 3.4: Cost correlation for different well drilling technology, a diameter of 8' has been considered for both correlation in order to make the results comparable. The blue curve represents the cost correlation for deep geothermal wells for which an oil and gas derived drilling rig is required (*Eq 3.23*). On the other hand, the orange curve represents the typical cost correlation for residential heat pump wells which requires much simpler devices for the drilling process (40$/feet). The grey area represents a transition zone between the two technologies for which hopefully it can be possible to reduce the drilling cost using simpler technologies.

3.3 Models Validation

The CPG model has been validated with result published by Adams et Al. [7], following the approach described by Schifflechner et Al. [27]. Validation results are presented in *Fig 3.1* showing a good accordance between the two predictions.

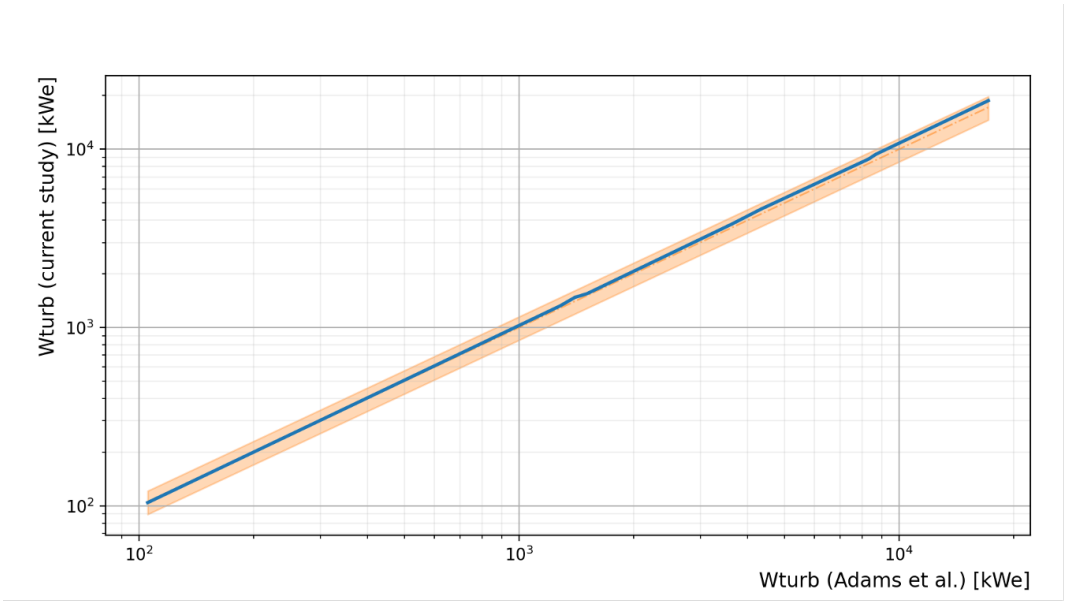

Figure 3.1: Model Validation: comparison of current study model result with result published by Adams et al. [7]. Orange area represent a 10% error band.

A more detailed validation has been performed in the scope of the HOCLOOP project [30], which aims at the development of a concentric BHE system. In the validation, presented in details in Deliverable 2.2, the model described in this chapter has been compared with the models developed

by two other partner of the project, showing again a good accordance, as can be seen in *Fig 3.2*.

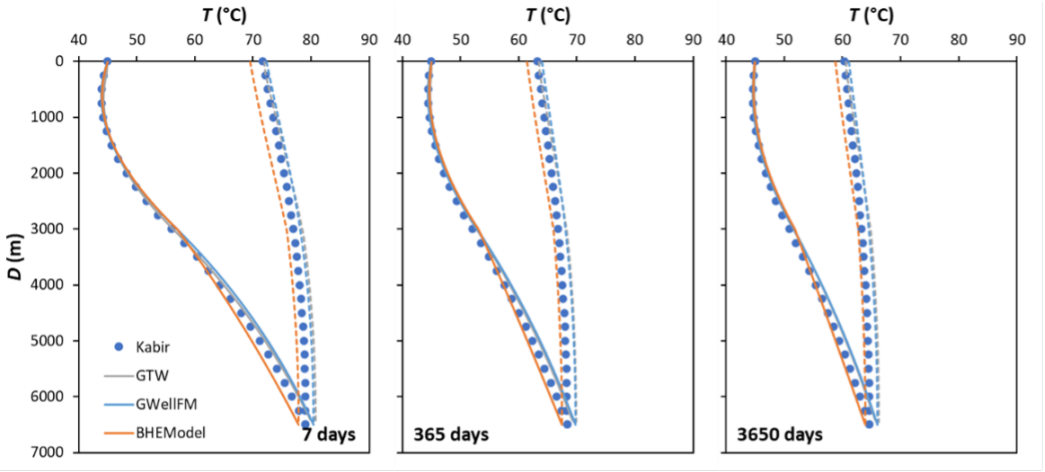

Figure 3.2: Model Validation: comparison of temperature profile along the well for models developed by different partners of the *HOCLOOP* project. The model described in this chapter is labeled *BHEModel*. *(Image from: Deliverable2.2 of the HOCLOOP project [31])*

References

[1] K. Pruess, "Enhanced geothermal systems (EGS) using CO2 as working fluid - A novel approach for generating renewable energy with simultaneous sequestration of carbon," *Geothermics*, vol. 35, no. 4, pp. 351–367, Aug. 2006, ISSN: 03756505. DOI: 10.1016/j.geothermics.2006.08.002.

[2] F. Jiang, J. Chen, W. Huang, and L. Luo, "A three-dimensional transient model for EGS subsurface thermo-hydraulic process," *Energy*, vol. 72, pp. 300–310, Aug. 2014, ISSN: 03605442. DOI: 10.1016/j.energy.2014.05.038.

[3] J. Chen and F. Jiang, "Designing multi-well layout for enhanced geothermal system to better exploit hot dry rock geothermal energy," *Renewable Energy*, vol. 74, pp. 37–48, 2015, ISSN: 09601481. DOI: 10.1016/j.renene.2014.07.056.

[4] T. Xu and K. Pruess, "Reactive Transport Modeling to Study Fluid-Rock Interactions in Enhanced Geothermal Systems (EGS) with CO2 as Working Fluid," in *Proceedings World Geothermal Congress*, Bali, Indonesia, Apr. 2010.

[5] L. André, N. Spycher, T. Xu, K. Pruess, and F.-D. Vuataz, "Comparing FRACHEM and TOUGHREACT for reactive transport modeling of brine-rock interactions in enhanced geothermal systems (EGS)," 2008.

[6] D. W. Peaceman, "Interpretation of Well-Block Pressures in Numerical Reservoir Simulation," *Soc Pet Eng AIME J*, vol. 18, no. 3, pp. 183–194, 1978.

[7] B. M. Adams, T. H. Kuehn, J. M. Bielicki, J. B. Randolph, and M. O. Saar, "A comparison of electric power output of CO2 Plume Geothermal (CPG) and brine geothermal systems for varying reservoir conditions," *Applied Energy*, vol. 140, pp. 365–377, Feb. 2015, ISSN: 03062619. DOI: 10.1016/j.apenergy.2014.11.043.

[8] A. D. Atrens, H. Gurgenci, and V. Rudolph, "CO2 Thermosiphon for Competitive Geothermal Power Generation," *Energy & Fuels*, vol. 23, no. 1, pp. 553–557, Jan. 2009, ISSN: 0887-0624. DOI: 10.1021/ef800601z.

[9] A. D. Atrens, H. Gurgenci, and V. Rudolph, "Electricity generation using a carbon-dioxide thermosiphon," *Geothermics*, vol. 39, no. 2, pp. 161–169, Jun. 2010, ISSN: 03756505. DOI: 10.1016/j.geothermics.2010.03.001.

[10] M. Tagliaferri, P. Gładysz, P. Ungar, *et al.*, "Techno-Economic Assessment of the Supercritical Carbon Dioxide Enhanced Geothermal Systems," *Sustainability*, vol. 14, no. 24, p. 16 580, Dec. 2022, ISSN: 2071-1050. DOI: 10.3390/su142416580.

[11] A. Truesdell and D. White, "Production of superheated steam from vapor-dominated geothermal reservoirs," *Geothermics*, vol. 2, no. 3-4, pp. 154–173, Sep. 1973, ISSN: 03756505. DOI: 10.1016/0375-6505(73)90022-9.

[12] G. Schubert, J. M. Straus, and M. A. Grant, "A problem posed by vapour-dominated geothermal systems," *Nature*, vol. 287, no. 5781, pp. 423–425, Oct. 1980, ISSN: 0028-0836. DOI: 10.1038/287423a0.

[13] J. M. Straus and G. Schubert, "One-dimensional model of vapor-dominated geothermal systems," *Journal of Geophysical Research: Solid Earth*, vol. 86, no. B10, pp. 9433–9438, Oct. 1981, ISSN: 01480227. DOI: 10.1029/JB086iB10p09433.

[14] R. Mastrullo, A. W. Mauro, L. Menna, and G. P. Vanoli, "A Model for a Borehole Heat Exchanger Working with CO2," *Energy Procedia*, vol. 45, pp. 635–644, 2014, ISSN: 18766102. DOI: 10.1016/j.egypro.2014.01.068.

[15] G. Galoppi, D. Biliotti, G. Ferrara, E. Carnevale, and L. Ferrari, "Feasibility Study of a Geothermal Power Plant with a Double-pipe Heat Exchanger," *Energy Procedia*, vol. 81, pp. 193–204, Dec. 2015, ISSN: 18766102. DOI: 10.1016/j.egypro.2015.12.074.

[16] A. E. Malek, B. M. Adams, E. Rossi, H. O. Schiegg, and M. O. Saar, "Techno-economic analysis of Advanced Geothermal Systems (AGS)," *Renewable Energy*, vol. 186, pp. 927–943, 2022, ISSN: 09601481. DOI: 10.1016/j.renene.2022.01.012.

[17] H. Carslaw and J. Jaeger, *Conduction of Heat in Solids*. Oxford, UK: Oxford University Press, 1959, pp. 334–339.

[18] S. Mishra and D. Guyonnet, "Analysis of Observation-Well Response During Constant-Head Testing," *Ground Water*, vol. 30, no. 4, pp. 523–528, Jul. 1992, ISSN: 0017-467X. DOI: 10.1111/j.1745-6584.1992.tb01528.x.

[19] J. A. Shonder and J. V. Beck, "Determining effective soil formation thermal properties from field data using a parameter estimation technique," Tech. Rep., 1998.

[20] Y. Zhang, L. Pan, K. Pruess, and S. Finsterle, "A time-convolution approach for modeling heat exchange between a wellbore and surrounding formation," *Geothermics*, vol. 40, no. 4, pp. 261–266, 2011, ISSN: 03756505. DOI: 10.1016/j.geothermics.2011.08.003.

[21] B. M. Adams, J. Ogland-Hand, J. Bielicki, P. Schädle, and M. Saar, "Estimating the Geothermal Electricity Generation Potential of Sedimentary Basins Using genGEO (the generalizable GEOthermal techno-economic simulator)," *ChemRxiv Preprint*, 2021.

[22] E. W. Lemmon, I. H. Bell, M. L. Huber, and M. O. McLinden, *NIST Standard Reference Database 23: Reference Fluid Thermodynamic and Transport Properties-REFPROP, Version 10.0, National Institute of Standards and Technology*, 2018.

[23] J. Dormand and P. Prince, "A family of embedded Runge-Kutta formulae," *Journal of Computational and Applied Mathematics*, vol. 6, no. 1, pp. 19–26, Mar. 1980, ISSN: 03770427. DOI: 10.1016/0771-050X(80)90013-3.

[24] P. Virtanen, R. Gommers, T. E. Oliphant, *et al.*, "SciPy 1.0: fundamental algorithms for scientific computing in Python," *Nature Methods*, vol. 17, no. 3, pp. 261–272, Mar. 2020, ISSN: 1548-7091. DOI: 10.1038/s41592-019-0686-2.

[25] S. W. Churchill, "Friction-factor equatin spans over all fluid-flow regimes," *Chemical Engineering*, vol. 84, pp. 91–92, 1977.

[26] P. Gładysz, A. Sowiżdżał, M. Miecznik, and L. Pajak, "Carbon dioxide-enhanced geothermal systems for heat and electricity production: Energy and economic analyses for central Poland," *Energy Conversion and Management*, vol. 220, Sep. 2020, ISSN: 01968904. DOI: 10.1016/j.enconman.2020.113142.

[27] C. Schifflechner, F. Dawo, S. Eyerer, C. Wieland, and H. Spliethoff, "Thermodynamic comparison of direct supercritical CO2 and indirect brine-ORC concepts for geothermal combined heat and power generation," *Renewable Energy*, vol. 161, pp. 1292–1302, 2020, ISSN: 18790682. DOI: 10.1016/j.renene.2020.07.044.

[28] B. M. Adams, T. H. Kuehn, J. M. Bielicki, J. B. Randolph, and M. O. Saar, "On the importance of the thermosiphon effect in CPG (CO2 plume geothermal) power systems," *Energy*, vol. 69, pp. 409–418, May 2014, ISSN: 03605442. DOI: 10.1016/j.energy.2014.03.032.

[29] U.S. Bureau of Labor Statistics, *Producer Price Index by Industry: Oil and Gas Extraction.* [Online]. Available: https://fred.stlouisfed.org/series/PCU21112111.

[30] European Project, *A circular by design environmentally friendly geothermal energy solution based on a horizontal closed loop - HOCLOOP*, 2022.

[31] V. Leontidis, M. Wangen, P. Ungar, and D. Fiaschi, " Flow pipe model for fluid circulation D2.2," HOCLOOP Project, Tech. Rep., 2023.

Appendices

3.A Rock Conduction Correlation Validation

3.A.1 Abstract

In this section, a detailed analysis of the behaviour of the heat transfer in the rocks surrounding the well is presented. The analysis has been carried out using FreeFEM, an open source software, and has focused mainly on the possible effect of the **geothermal gradient** and of the **reservoir fluid convection** over the heat transfer properties. Correction factors for *Eq 3.10* have been developed to model these effects.

3.A.2 Introduction

The correlation described in *Eq 3.9* has been validated comparing its results to a FEM analysis to understand the conditions where such correlation can be safely applied. The FEM analysis has been carried out using FreeFEM [1], an open-source, finite element based, partial differential equation solver. The solver is based on C++, and uses, for the problem definition, scripts written in dedicated language (C++ based) and saved as ".edp" files.

3.A.3 Methodology

Model Differential Equation

FreeFEM has been used to integrate the heat equation, defined as follows:

$$\frac{1}{\alpha_{rocks}}\frac{\partial T}{\partial t} = \nabla^2 T + \frac{Pe}{d_{well}}\hat{v}\cdot\nabla T \tag{3.24}$$

Eq 3.24 consider also the presence of a convection term due to a fluid flowing with speed $\vec{v}$ trough the rocks media.
In *Eq 3.24*, α_{rocks} is the thermal diffusivity of the rocks and Pe is the Péclet number modelling the relative impact of the conduction and the convection:

$$Pe = \frac{d_{well} \mid \vec{v} \mid}{\alpha_{rocks}} \tag{3.25}$$

Eq 3.24 can be adimensionalized, replacing time and space coordinates with their dimensionless counterpart:

$$t_d = \frac{\alpha_{rocks} t}{d_{well}^2} \tag{3.26}$$

$$x_d = \frac{x}{d_{well}} \tag{3.27}$$

Resulting in:

$$\frac{\partial}{\partial t_d} = \frac{\partial t}{\partial t_d}\frac{\partial}{\partial t} = \frac{d_{well}^2}{\alpha_{rocks}}\frac{\partial}{\partial t} \tag{3.28}$$

$$\nabla_d = \begin{bmatrix} \frac{\partial}{\partial x_{0_d}} \\ \frac{\partial}{\partial x_{1_d}} \\ \vdots \\ \frac{\partial}{\partial x_{n_d}} \end{bmatrix} = \begin{bmatrix} \frac{\partial x_0}{\partial x_{0_d}}\frac{\partial}{\partial x_0} \\ \frac{\partial x_1}{\partial x_{1_d}}\frac{\partial}{\partial x_1} \\ \vdots \\ \frac{\partial x_n}{\partial x_{n_d}}\frac{\partial}{\partial x_n} \end{bmatrix} = \frac{1}{d_{well}}\nabla \tag{3.29}$$

$$\nabla_d^2 = \frac{1}{d_{well}^2}\nabla^2 \tag{3.30}$$

Moreover, temperature can be adimensionalized considering the temperature difference between the well surface and the undisturbed rocks (ΔT_∞):

$$T_d = \frac{T}{\Delta T_\infty} \tag{3.31}$$

By substituting *Eq 3.26*, *Eq 3.29*, *Eq 3.30* and *Eq 3.31* in *Eq 3.24* the resulting adimensional equation is obtained:

$$\frac{\partial T_d}{\partial t_d} = \nabla_d^2 T_d + Pe\ \hat{v}\cdot\nabla_d T_d \tag{3.32}$$

FreeFem requires the variational form of *Eq 3.32* to perform the simulation which can be obtained as follows [2]:

$$\frac{\partial}{\partial t_d}\int_\Omega T_d\ u\ d\omega = \int_\Omega \nabla_d^2 T_d\ u\ d\omega + Pe\int_\Omega \hat{v}\cdot\nabla_d T_d\ u\ d\omega \tag{3.33}$$

Solving using integration by parts:

$$\frac{\partial}{\partial t_d}\int_\Omega T_d\ u\ d\omega - \int_\Omega \nabla_d T_d\cdot\ \nabla_d u\ d\omega - \int_\Gamma \hat{n}\cdot\nabla_d T_d\ u\ d\gamma - Pe\int_\Omega \hat{v}\cdot\nabla_d T_d\ u\ d\omega = 0 \tag{3.34}$$

Where u is a generic test function, Ω is the calculation domain, and Γ is the domain boundary (oriented following $\hat{n}$). *Eq 3.34* is the equation implemented in FreeFEM.
Both an explicit and an implicit first-order time integration scheme has been implemented and compared to identify the faster method for a given accuracy:

- **Implicit scheme:**

$$\frac{A\left(t_{d_{n+1}}\right) - A\left(t_{d_n}\right)}{\Delta t_d} = B\left(t_{d_{n+1}}\right) \tag{3.35}$$

- **Explicit scheme:**

$$\frac{A\left(t_{d_{n+1}}\right) - A\left(t_{d_n}\right)}{\Delta t_d} = B\left(t_{d_n}\right) \tag{3.36}$$

With:

$$A\left(t_d\right) = \int_{\Omega} T_d \; u \; d\omega \tag{3.37}$$

$$B\left(t_d\right) = \int_{\Omega} \nabla_d T_d \cdot \; \nabla_d u \; d\omega + \int_{\Gamma} \hat{n} \cdot \nabla_d T_d \; u \; d\gamma + Pe \int_{\Omega} \; \hat{v} \cdot \nabla_d T_d \; u \; d\omega \tag{3.38}$$

The implicit formulation has been used for pure conduction analysis ($Pe = 0$). On the other hand, the explicit formulation has been used for mixed conduction - convection problems, where the minimum time step has to be chosen according to the CFL condition.
For same reason, a fixed time steps has been used for the mixed conduction - convection problems while, for the simple conduction problem, the time in which the temperature distribution is evaluated have been spaced evenly on a log10 scale in order to concentrate an higher number of time steps in the initial transient:

$$t_{d_i} = t_{d_{start}} \left(\frac{t_{d_{end}}}{t_{d_{start}}} \right)^{\frac{i}{n_{steps}}} \quad with \;\; i = (1, n_{step}) \tag{3.39}$$

Where n_{steps} is the number of steps to be taken during the integration process.

Domain Geometry

The domain represent a 2D section of reservoir perpendicular to the well. The geometry, described in *Fig 3.A.1*, is composed of a rectangular section with an circular hole in the middle representing the well.

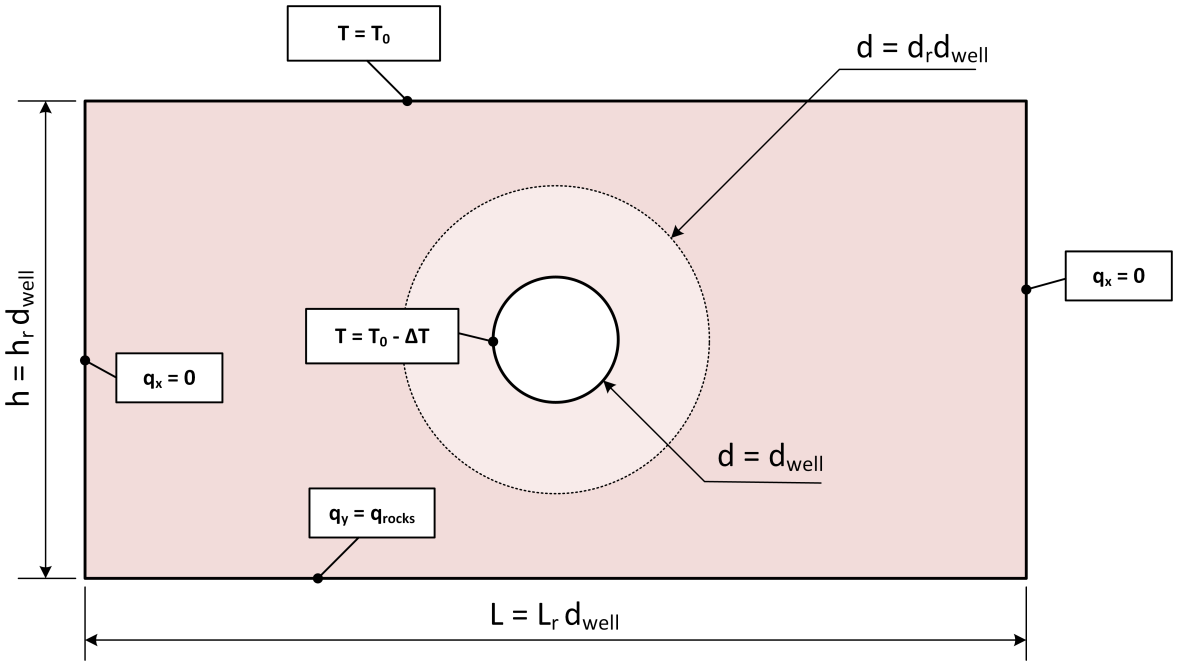

Figure 3.A.1: Scheme of the conduction problem geometry and boundary condition as defined in the FreeFEM software

The domain has been subdivided into two subdomains for increasing mash quality: A circular domain around the well (highlighted in light red in *Fig 3.A.1*) with increased mesh density is meant to make the temperature profile more accurate in the area where the steepest gradient are located. The rest of the domain is devoted to extending the boundary condition as far as possible from the well, hence the mesh density there can be decreased.

The computational domain's size was adjusted in proportion to the well-bore diameter using the parameters summarized in *Fig 3.A.1* the table below:

Table 3.A.1: Design parameters for the FreeFEM computational domain

Parameter	Description
h_r	ratio between the **height** of the domain an the well diameter
L_r	ratio between the **length** of the domain an the well diameter
d_r	ratio between the **diameter of the inner subdomain** and the well diameter

3.A.4 Results

Mesh Sensitivity

In FreeFEM, the mesh density is controlled mainly by imposing the number of points on each boundary element. In our code this was controlled by two parameters n and m. Where, as shown in *Fig 3.A.2*, n controls the overall mesh density while m controls the density differential between the internal and external domain.

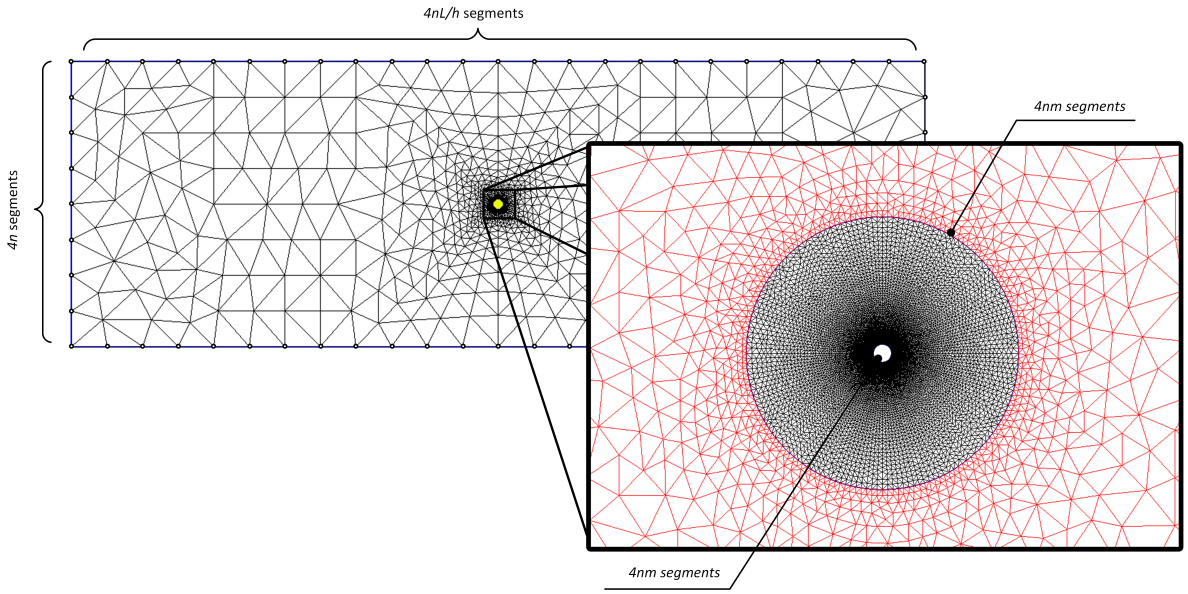

Figure 3.A.2: Example of mesh used for the reservoir heat transfer evaluation ($n = 2$, $m = 20$, $h_r = 500$, $L_r = 1500$, $d_r = 15$)

The number of segments for each domain boundary have been summarized in the table that follows:

Table 3.A.2: Number of segments for each domain boundary

Boundary	Segments
Vertical Boundary (height h)	$4n$
Horizontal Boundary (length L)	$4n\frac{L}{h}$
Well boundary (diameter $= d_{well}$)	$4nm$
Subdomains Interface (diameter $= d_r d_{well}$)	$4nm$

In *Fig 3.A.3* the result of the sensitivity on both the time step size and the mesh dimension are shown.

Regarding the time step size, using the implicit solution method and the time discretization described in *Eq 3.39* it appears evident that $n_{steps} = 50$ is enough for assuring convergence. On the other hand, regarding the mesh dimensions, multiple combinations of n and m can be selected assuring a satisfying accuracy of the results. Moreover, a wider mesh result in a poor description of the initial transient ($t_d < 10^{-1}$ in the wider mesh) due to the incorrect approximation of the temperature gradient around the well. In usual geothermal application, the well is usually operated continuously throughout its lifespan limiting the impact of the inital transient.

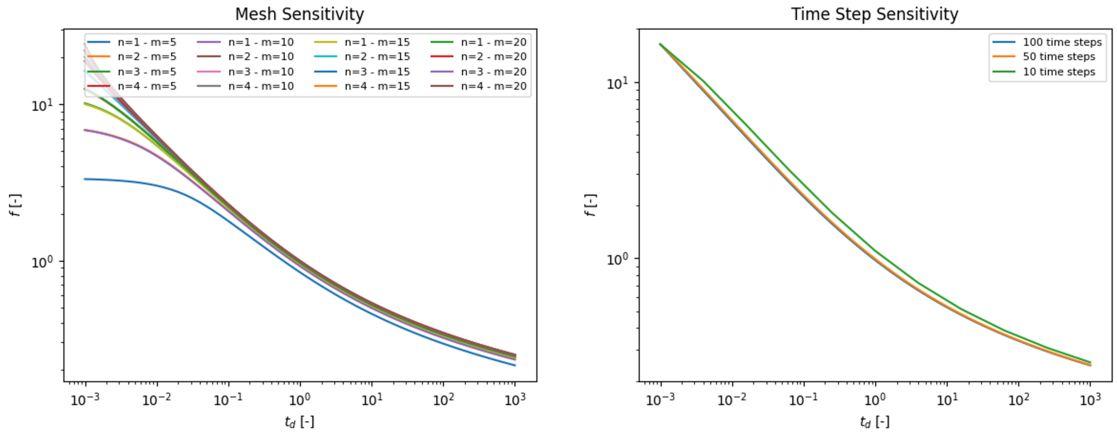

Figure 3.A.3: Mesh size and Time Steps sensitivity

To chose the optimal combination of n and m, the computation time of the different mesh have been compared to identify the most efficient scheme. The accuracy of a specific mesh has been evaluated as the difference between the its results and the result obtained from the most detailed mesh evaluated ($n = 4 - m = 20$). Both the mean error for all the evaluated time steps, and the error of the last time step only, have been computed and are shown in *Fig 3.A.4*. The first one is an index of the accuracy of the overall solution while the latter refers to the near-stationary state where the geothermal well will likely operate.

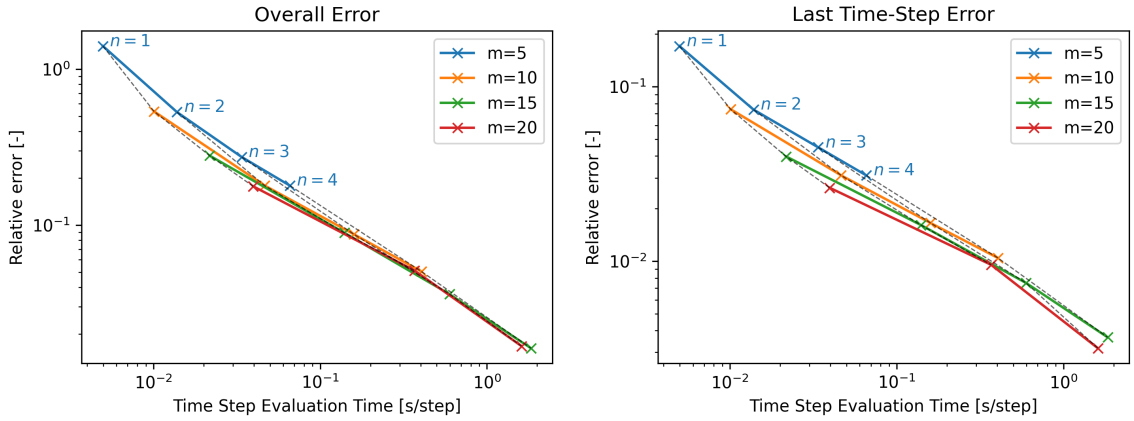

Figure 3.A.4: Run time vs. accuracy for different mesh configurations

As results from the figure, increasing m while decreasing n reduce the computational time while maintaining a fixed accuracy. This is because increasing m will increase the number of nodes in

the near-well region increasing the accuracy of the evaluation in an area with a significant thermal gradient.

Base Conduction Comparison

Initially, the adimensional coefficient $f(t_d)$ (as defined in *Eq 3.10*) has been compared with the result provided by the finite element simulation for a simple case in which both the convection effect and the existence of a geothermal gradient have been neglected ($Pe = 0$, $q_{rocks} = 0$).
For the finite element case, $f(t_d)$ has been evaluated starting from the radial temperature gradient evaluated on the well boundary as follows:

$$f(t_d) = \frac{r_{well}}{2\pi\Delta T_\infty} \int_{\theta=0}^{2\pi} \left.\frac{\partial T}{\partial r}\right|_{r=r_{well}} d\theta \tag{3.40}$$

where the radial temperature gradient ($\partial T/\partial r$) has been adimensionalized using the temperature difference between the well wall and the undisturbed rocks (ΔT_∞) and the well radius (r_{well}).

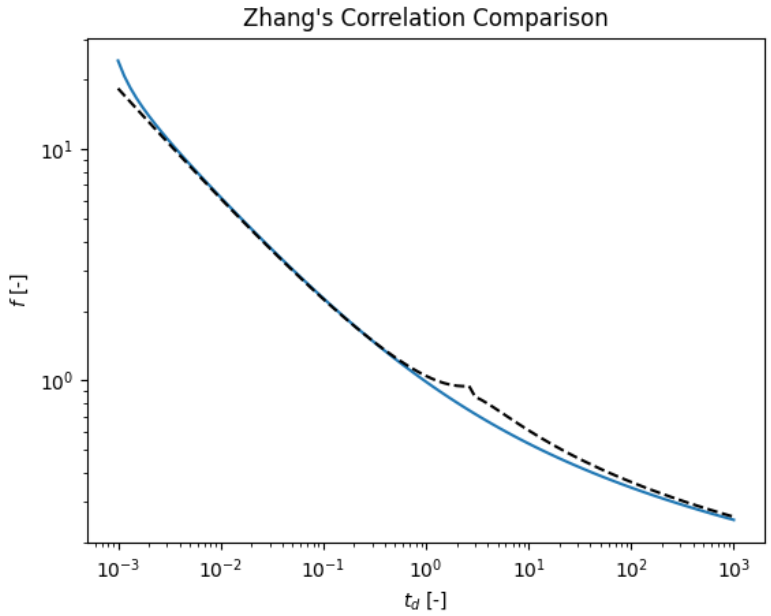

Figure 3.A.5: Comparison between Zhang's correlation [3] and FreeFEM results *(mesh parameters: $n = 4$, $m = 20$, $h_r = 500$, $L_r = 1500$, $d_r = 15$, 100 time steps).*

Result of the comparison are presented in *Fig 3.A.5*, showing a reasonable level of accuracy for the correlation for every t_d except for an interval around $t_d = 2.8$ (i.e. where the two functions that defines the correlation overlaps). Considering a typical thermal diffusivity of rocks being approximately $10^{-6} m^2/s$ [4] and a $0.1m$ well diameter, $t_d = 2.8$ implies $t \approx 2.8 \cdot 10^4 s$ or $t \approx 8h$, which is a very initial stage of the well operation.

Effect of the geothermal gradient

The presence of a geothermal gradient can effect the heat transfer effectiveness between the well and the rocks. To study this effect different simulations have been performed imposing different gradients over the lower boundary of the domain (see *Fig 3.A.1*).

The gradient has been adimensionalized as follows in order to be implemented in the non-dimensional equation *Eq 3.32*:

$$\nabla T_{rocksd} = \frac{d_{well}}{\Delta T_{\infty}} \frac{\partial T}{\partial z} \tag{3.41}$$

In *Fig 3.A.6* are shown the results of the simulations. From the figure, it is clear that the presence of a geothermal gradient slightly decrease the thermal resistance of the rocks in the reservoir.

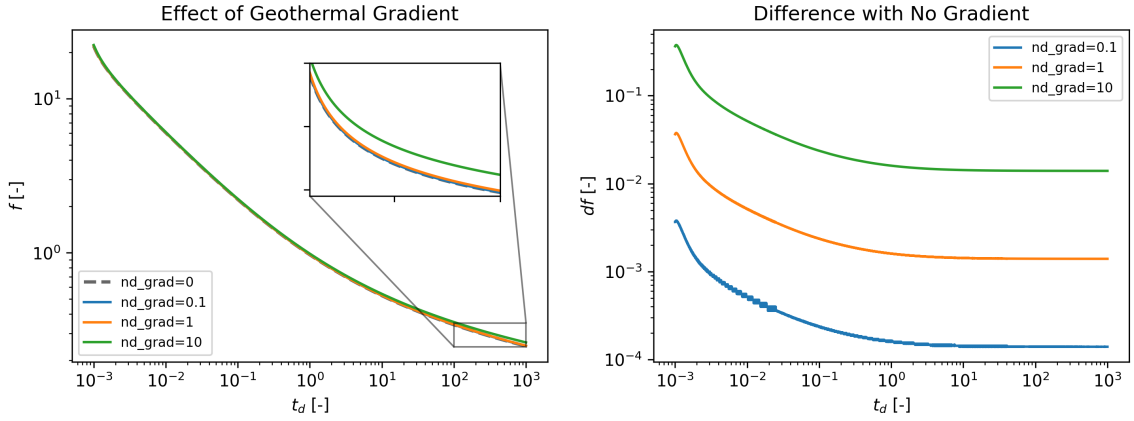

Figure 3.A.6: Effect of the geothermal gradient over time *(mesh parameters:* $n = 3$, $m = 20$, $h_r = 500$, $L_r = 1500$, $d_r = 15$, *10000 time steps).*

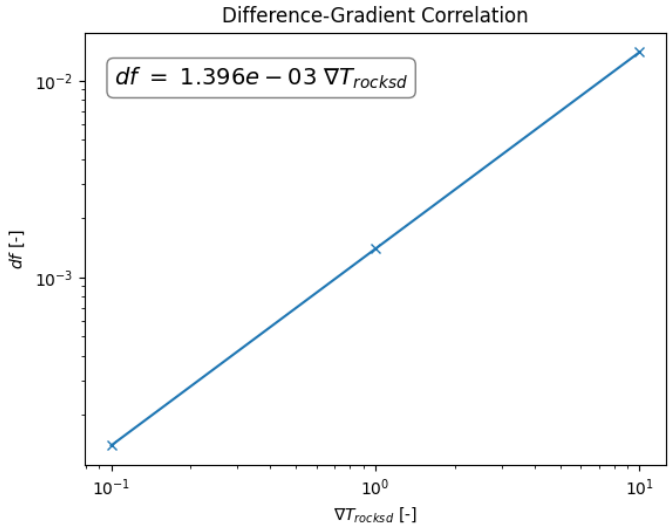

Figure 3.A.7: Linear relation between the change in f and the adimensional gradient after the initial transient: the points shown are the result of the simulation at $t_d = 10^3$

The change in f (evaluated following *Eq 3.40*) relative to the case without any gradient decreases during the initial transient period and stabilizes when $t_d \approx 1$. The difference in f in the final time steps exhibits a linear dependence on the dimensionless gradient, as illustrated in Figure *Fig 3.A.7* Nevertheless, the impact of the temperature gradient remains negligible in geothermal applications. Geothermal gradients typically fall within the range of 10^{-2} to 10^{-1}°C/m. For instance, Alberta, Canada, exhibits an average gradient of 20°C/km [5], the Netherlands displays 31°C/km [6], and a geothermal area in south Tuscany records 100°C/km [7]. Meanwhile, both the well diameter and the

temperature difference remain on the order of tens of centimeters and tens of degrees, respectively. Substituting these values into *Eq 3.41* yields ∇T_{rocksd} within the range of 10^{-4} to 10^{-3} and $df \approx 10^{-6}$ (according to the equation displayed in *Fig 3.A.7*), completely negligible considering that $f > 10^{-1}$.

Effect of the fluid convection

For assessing the effect of the convection on the heat transfer the simulation has been repeated for different values of the Peclet number (Pe). The flow of the fluid around the well has been modelled using the well known formula for a potential flow around a cylinder:

$$\begin{pmatrix} \hat{v}_x \\ \hat{v}_y \end{pmatrix} = \begin{pmatrix} \frac{\partial \phi}{\partial x} \\ \frac{\partial \phi}{\partial y} \end{pmatrix} \tag{3.42}$$

where ϕ is the velocity potential defined as follows:

$$\phi = \left(r - \frac{{r_{well}}^2}{r} \right) cos(\theta) \tag{3.43}$$

where $r = x^2 + y^2$ and θ is the angle position relative to the unobstructed flow. The flow resulting from *Eq 3.43* is shown schematically in *Fig 3.A.8*

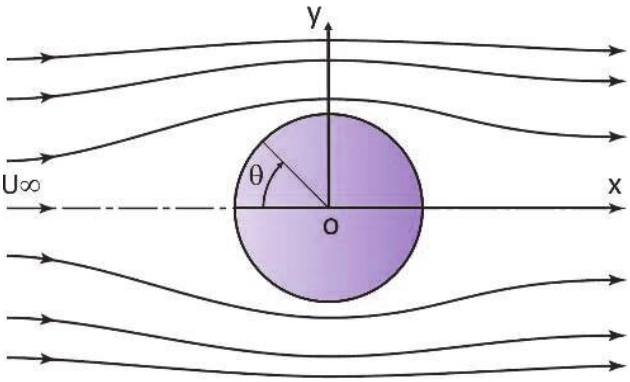

Figure 3.A.8: Pictogram of the potential flow over a cylinder resulting from *Eq 3.43*, *(image from Bardera et Al. [8])*

Eq 3.43 could be a reasonable approximation of the flow for very low velocities and high permeability (meaning that the rocks will not oppose a great resistance to the fluid movement along its streamline) which could be a reasonable assumption in fluid movements in fractures perpendicular to the well path.

The results of the simulations are shown in *Fig 3.A.9*. It is clear that the presence of a convective fluid allow the system to reach a stationary condition after an initial transient due to the fact that the convection will counteract the cooling of the rocks around the well.

The higher the Peclet number, the higher the value of f over which the system will eventually settle. Moreover, as shown by *Fig 3.A.9* on the right, a correlation can be found between the Pe and the steady state f, which can be used for the estimation of the effect for different conditions.

Flow velocities in rocks fractures are usually very low. For example Pasquale et Al. [9] published some data showing velocities ranging from 10^{-8} to 10^{-5} m/s. This will result in a range for Pe between 10^{-3} and 1 (again considering $\alpha \approx 10^{-6} m/s^2$ and $d_{well} \approx 10^{-1} m$). Meaning that a flow

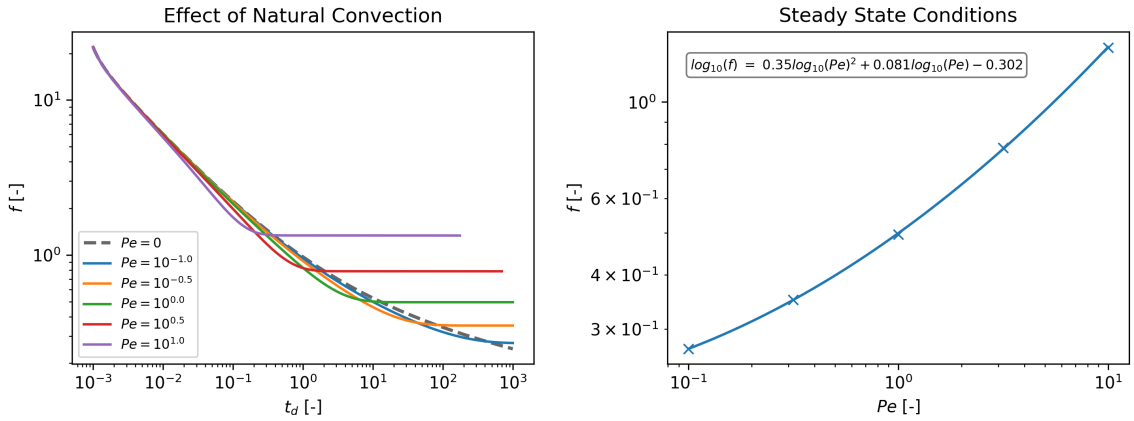

Figure 3.A.9: Effect of fluid convection over time *(mesh parameters:* $n = 3$, $m = 20$, $h_r = 500$, $L_r = 1500$, $d_r = 15$, *10000 time steps).*

stabilization can be achieved in reasonable time (hours according to the result presented in *Fig 3.A.9* for $Pe = 1$) targeting high fluid speed regions of the reservoir.

3.A.5 Conclusions

To conclude the simulations performed with FreeFEM have produced the following results:

- For simple cases (meaning without convection or presence of strong geothermal gradients) the correlation *Eq 3.10* **can be used for the prediction of the rocks thermal resistance around the well**
- Geothermal gradients **has no significant effect on the heat transfer (for typical geothermal condition)**. Anyway, as a general finding, a linear correlation has been identified between deviation of f from *Eq 3.10* and the non dimensional gradient (*Eq 3.41*):

$$df = 1.396\ 10^{-3}\ \nabla T_{rocksd} \tag{3.44}$$

  which can be used to predict the behaviour of the well even in extreme gradient condition.

- Fluid convection **can have a significant impact on the well behaviour**. Their presence will drive the system to a **stationary condition**. A correlation has been found between the stationary value of f and the Peclet number:

$$log_{10}(f_s) = 0.35(log_{10}(Pe))^2 + 0.081log_{10}(Pe) - 0.302 \tag{3.45}$$

  This correlation can be used to predict the system behaviour extending *Eq 3.10* as follows:

$$f(t_d) = max(f(t_d)_{base}, f_s) \tag{3.46}$$

  where $f(t_d)_{base}$ is the result of *Eq 3.10* while f_s is the correlation result. Meaning that the dimensionless time at which the system will reach the stationary state can be identify as:

$$f(t_d)_{base} = f_s \tag{3.47}$$

References

[1] F. Hecht, "New development in freefem++," *Journal of Numerical Mathematics*, vol. 20, no. 3-4, Jan. 2012, ISSN: 1569-3953. DOI: 10.1515/jnum-2012-0013.

[2] H. P. Langtangen and K.-A. Mardal, *Introduction to Numerical Methods for Variational Problems*. Cham: Springer International Publishing, 2019, vol. 21, ISBN: 978-3-030-23787-5. DOI: 10.1007/978-3-030-23788-2.

[3] Y. Zhang, L. Pan, K. Pruess, and S. Finsterle, "A time-convolution approach for modeling heat exchange between a wellbore and surrounding formation," *Geothermics*, vol. 40, no. 4, pp. 261–266, 2011, ISSN: 03756505. DOI: 10.1016/j.geothermics.2011.08.003.

[4] M. M. Miranda, C. R. Matos, N. V. Rodrigues, A. J. S. C. Pereira, and J. J. Costa, "Effect of temperature on the thermal conductivity of a granite with high heat production from Central Portugal," *Journal of Iberian Geology*, vol. 45, no. 1, pp. 147–161, Mar. 2019, ISSN: 1698-6180. DOI: 10.1007/s41513-018-0096-9.

[5] K. Huang, C. Hickson, D. Cotterill, and Y. Champollion, "Geothermal assessment of target formations using recorded temperature measurements for the alberta no. 1 geothermal project," *Applied Sciences (Switzerland)*, vol. 11, no. 2, pp. 1–10, Jan. 2021, ISSN: 20763417. DOI: 10.3390/app11020608.

[6] E. Békési, M. Struijk, D. Bonté, *et al.*, "An updated geothermal model of the Dutch subsurface based on inversion of temperature data," *Geothermics*, vol. 88, p. 101 880, Nov. 2020, ISSN: 03756505. DOI: 10.1016/j.geothermics.2020.101880.

[7] G. Buonasorte, R. Cataldi, A. Ceccarelli, *et al.*, "Ricerca ed esplorazione nell'area geotermica di Torre Alfina (Lazio-Umbria)," *Italian Journal of Geosciences*, vol. 107, no. 2, pp. 265–337, Jan. 1988, ISSN: 2038-1719.

[8] R. Bardera, S. Sor, and A. García-Magariño, "Aerodynamics of Mars 2020 Rover Wind Sensors," in *Mars Exploration - a Step Forward*, IntechOpen, Sep. 2020. DOI: 10.5772/intechopen.90912.

[9] V. Pasquale, M. Verdoya, and P. Chiozzi, "Darcy velocity and Péclet number analysis from underground thermal data," *Bollettino di Geofisica Teorica ed Applicata*, vol. 51, 2010.

Chapter 4

Application Case Study: Industrial Heat Production

The analysis that follows is a revised and expanded version of the paper *Thermodynamic assessment of Geothermal High-Temperature Heat Pumps for Industrial Steam Production* which is currently under review and can be accessed in its pre-print version [1]. In that paper, the performances of a CO_2 based HTHP for industrial steam generation (saturated steam at 12 barg (191.60 °C)) has been compared to some water based configurations in order to asses the advantages of the different solutions.

4.1 Introduction

Efficient production and distribution of renewable energy are key challenges to reaching the net-zero target by 2050. Particularly, in 2021, heat production accounted for half of the total energy consumption in the world [2], 51% of which was required from industrial processes, which commonly need a heat temperature above 80°C [3]. In addition, according to a work published in 2019 by the Oxford Study for Energy Studies, industrial processes requiring heat in the temperature range of 100°C – 500°C represent 30% of the total industrial heat requirements and are connected mainly with paper and print, food, and chemical processes [4]. HTHP are one of the most promising technologies for the decarbonization of industrial heat demand. For this reason, in recent years there has been a growing scientific interest in the field.

High-Temperature Heat Pumps

Arpagaus et al., 2018 [5], did a very extensive review of the actual market and state of art of high-temperature heat pumps, highlighting the need for the progressive development of HTHP with a delivery temperature of over 140°C. A detailed analysis of the possible configurations for those applications has been published by Zühlsdorf et Al. in 2019 [6]. In their paper, they focus on the production of steam for industrial application analyzing two different HTHP configurations which have proven to be competitive, in terms of levelized cost of heat, with other technologies. According to the authors of this study, the most promising cycles for industrial steam production are a steam compression system and a sCO2 reversed Bryton cycle. These cycles, slightly modified for integration with the geothermal system, have been analyzed in this study. As pointed out by

Asparagus [5], the efficiency of an HTHP system is directly related to the source temperature, hence coupling the heat pump with a geothermal system could be extremely beneficial in terms of energy consumption.

Analyzed Configurations

The performance of the CO2-based and the water-based systems, depicted in *Fig 4.1*, have been compared aiming at the production of industrial steam starting from mid-low temperature geothermal resources. The described configurations are adaptation of the schemes described in the work by Zühlsdorf et Al. [6] to a geothermal environment. In particular, for the CO2-based schemes, *Fig 4.1*.a and *Fig 4.1*.b, the sCO2 pressurized and heated by the well can be further compressed to allow high-temperature heat generation and then expanded after the heat exchanger to make the process more efficient. Compression itself can be driven by an electric motor, *Fig 4.1*.a or directly by the expansion of a bleed from the main sCO2 flow, *Fig 4.1*.b. The disadvantage of the second configuration is that a higher flow rate of sCO2 is needed to produce the same amount of heat/vapor.
On the other hand, for water-based systems, the heated water can be either used to feed a High-Temperature ORC Heat Pump which in turn produces steam in a steam generator (ORC condenser/desuperheater), *Fig 4.1*.c, or directly flashed to produce steam that will then be compressed to the desired condition, *Fig 4.1*.d.

4.2 Methodology

Overall optimization of the system

The well model described in *Chapter 3* has been coupled with the models of the different surface plant configurations in order to perform a direct optimization of the overall system. The optimization process aims to maximize two different objectives, highlighted in *Tab 4.1*.

Table 4.1: HTHP Optimization Objectives

Parameter	Comment
$COP = \dot{Q}_{steam}/\dot{W}_{net}$	$\dot{Q}_{steam}$ is the heat provided to the generated steam and $\dot{W}_{net}$ is the net electrical power consumption of the heat pump
$\dot{m}_{ratio} = \mu_{ratio}\dot{m}_{steam}/\dot{m}_{BHE}$	$\dot{m}_{steam}$ and $\dot{m}_{BHE}$ are respectively the flow rate of steam and the flow rate of the fluid circulated in the well. $\mu_{ratio} = \mu_{fluid}/\mu_{H_2O}$ represent the viscosity ratio between the selected fluid and water (for CO_2 , $\mu_{ratio} = 2.45$ [7])

These parameters are of interest as COP is associated with the Operational Expenditure (OPEX) of the plant, whereas $\dot{m}_{ratio}$ will likely affect the Capital Expenditure (CAPEX). This is because, electrical consumption typically represents the most substantial component of the operating costs, while having to circulate an higher flow rate of fluid in the reservoir means drilling larger, or even multiple wells, impacting the capital investment, as usually drilling cost accounts for approximately 60% of the total investment [8]. Note that, in this perspective, the introduction of μ_{ratio} is functional

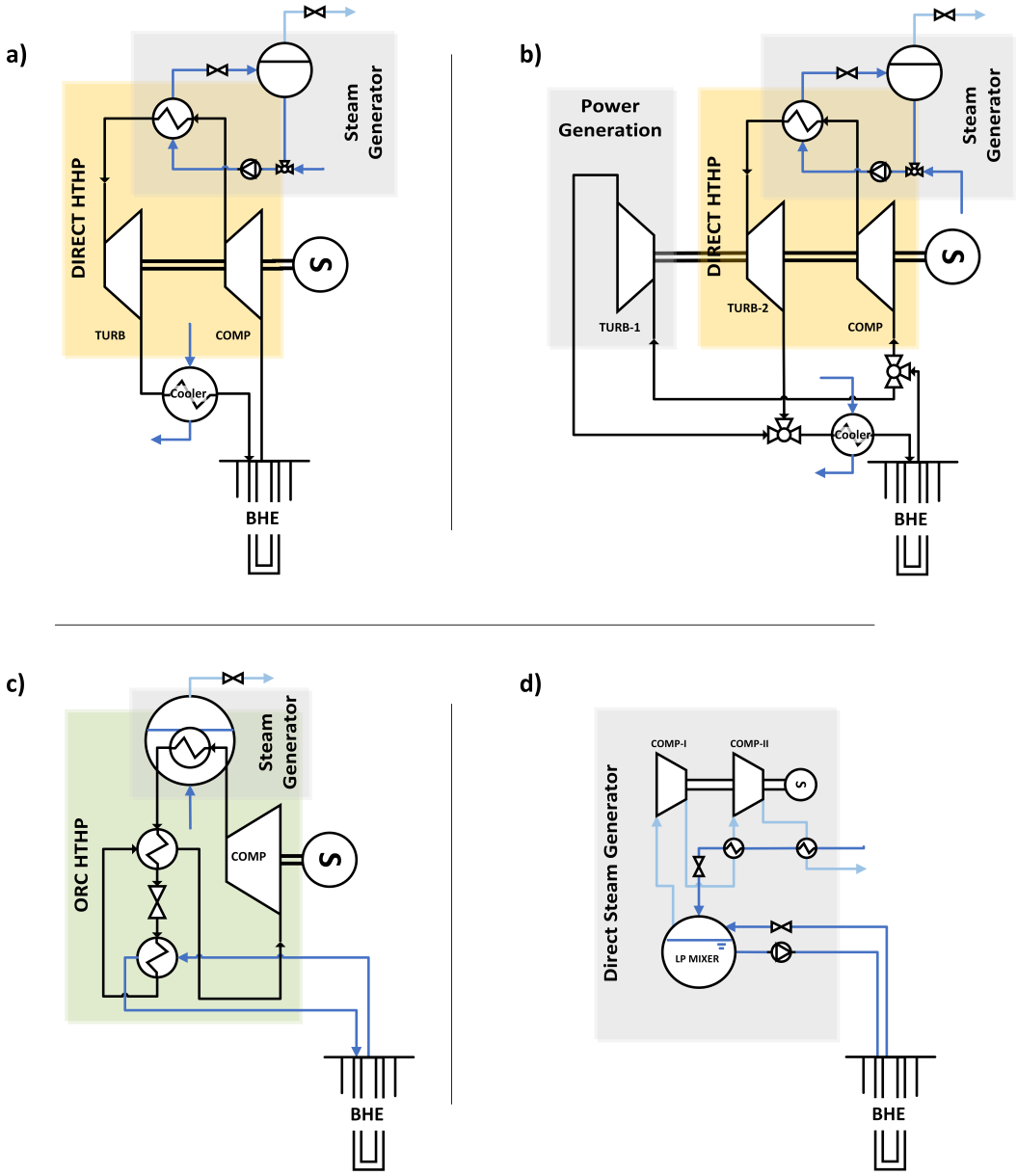

Figure 4.1: Proposed high-temperature high-pressure (HTHP) schemes: a) Direct scheme driven by an electric motor, b) Direct scheme driven by a bleed of the sCO2 stream, c) Indirect organic Rankine cycle (ORC) heat pump fueled by water circulating in the borehole heat exchanger (BHE), and d) direct steam generation.

to re-scale $\dot{m}_{BHE}$ in a way that, with different fluids circulated, the Reynolds number in the well remains constant for the same $\dot{m}_{ratio}$.

For these reasons, both $\dot{m}_{ratio}$ and COP has to be maximised for optimizing the system's thermodynamic performance. To conduct this multi-objective optimization, an additional parameter (x_{min}), defined as follows, has been minimized:

$$x_{min} = \frac{\dot{m}_0}{\dot{m}_{ratio}} + \Omega \frac{COP_0}{COP} \tag{4.1}$$

Where $\dot{m}_0$ and COP_0 are two arbitrarily chosen normalization factors ($\dot{m}_0 = 1/20$; $COP_0 = 3$). The parameter Ω defines the relative weight of $\dot{m}_{ratio}$ and COP, and hence the CAPEX and the

OPEX, in the optimization process. For this reason, the choice of Ω is related to the design condition of the HTHP. For instance, a high cost of electricity and low investment cost (favorable geothermal conditions, easy access to the resource) results in values of Ω higher than 1. On the other hand, Ω will decrease if the investment cost increase.

Remarks on the Pareto-front optimization

The proposed approach (minimising x_{min}) is equivalent to identifying the Pareto frontier and the selecting a specific point on it using Ω as a weighting factor. In fact, the optimal point identified using *Eq 4.1* is guaranteed to be part of the Pareto frontier if Ω>0. This is because, if a point x is not part of the frontier, there should be another point x^* so that:

$$\dot{m}_{ratio}(x) < \dot{m}_{ratio}(x^*) \wedge COP(x) < COP(x^*) \tag{4.2}$$

But if that is the case, considering *Eq 4.1*, $x_{min}(x) > x_{min}(x^*)$, hence x is not a minimum.

Surface Plant Models

The model of all the different surface plant configurations proposed in this article was developed in Python. The steam generation units are designed to provide saturated steam at 12 barg (191.60 °C) - a typical value for paper-mills steam circuits [9]. Each configuration has a specific optimization parameter that will be identified in the description of the system.

a. sCO_2 high temperature heat pump (*Fig 4.1*.a)

A steam drum arrangement, shown in *Fig 4.1*, was selected for the steam generation section. This configuration is more practical than a typical shell and tube heat exchanger considering the significant pressure expected on the sCO_2 side. The mass ratio between sCO_2 and water in the heat exchanger was selected to maximize the heat transfer efficiency by coupling the heat capacity of the fluids:

$$\dot{m}_{H_2O_{ratio}} = \frac{\dot{m}_{sCO_2}}{\dot{m}_{H_2O}} = \frac{c_{p_{sCO_2}}}{c_{p_{H_2O}}} \tag{4.3}$$

After the heat exchanger, the hot water is expanded in a valve to reach the pressure of the steam drum. $\dot{m}_{ratio}$ can be then immediately calculated considering the resulting vapour quality after the expansion (x_{exp}):

$$\dot{m}_{ratio} = \frac{\dot{m}_{steam}}{\dot{m}_{sCO_2}} = \frac{x_{exp}\dot{m}_{H_2O}}{\dot{m}_{sCO_2}} = \frac{x_{exp}}{\dot{m}_{H_2O_{ratio}}} \tag{4.4}$$

After the heat exchanger, the sCO_2 is expanded to recover part of the compressor power and cooled to increase its density and to maximize the thermo-syphon effect generated by the well. Resulting in the following COP:

$$COP = \frac{\dot{Q}_{steam}}{\dot{W}_{net}} = \dot{m}_{ratio}\frac{\Delta h_{vap}}{\Delta h_{comp} - \Delta h_{turb_{HP}}} \tag{4.5}$$

The optimal maximum temperature of the sCO_2 cycle ($T_{CO_2 max}$ - inlet of the heat exchanger), can be identified trough the x_{min} minimization: higher temperatures will increase x_{exp} and consequently $\dot{m}_{ratio}$ but require higher compression work, decreasing the COP. The water-side pressure in the

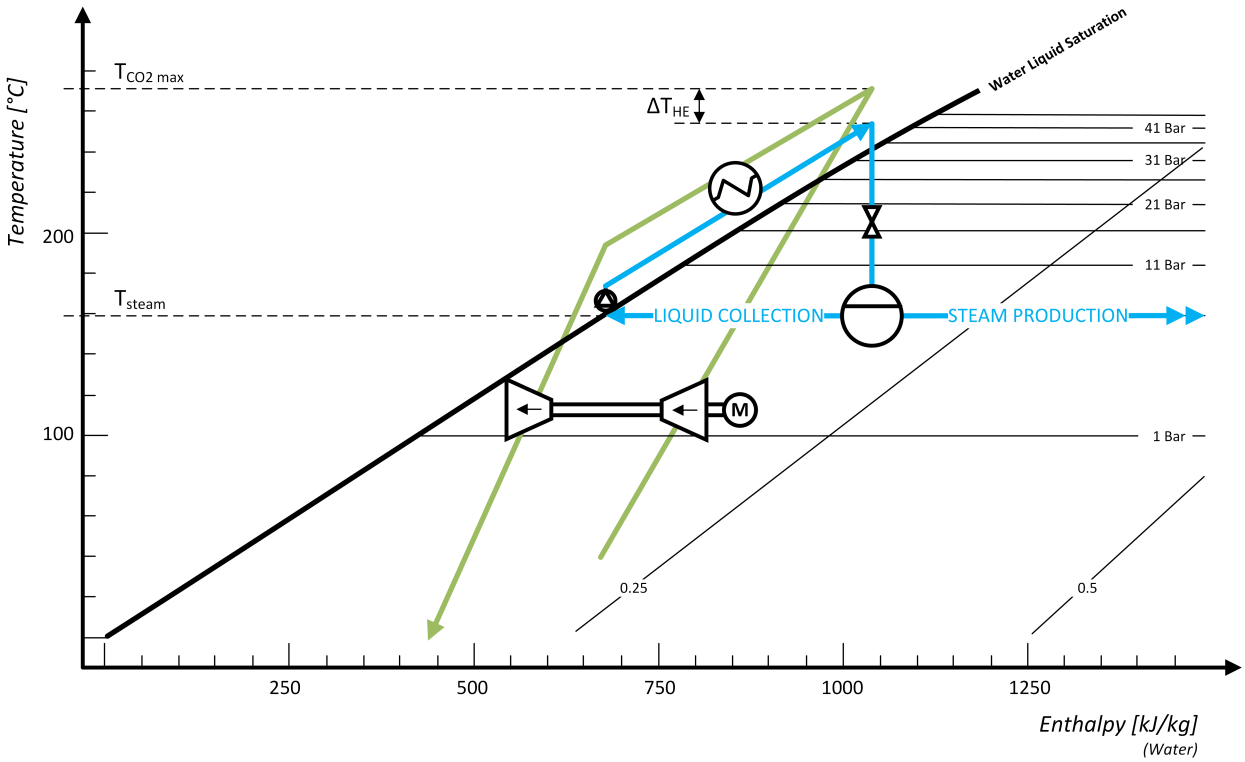

Figure 4.1: Schematic of the HTHP steam generation system on a temperature-enthalpy (T-h) diagram. The sCO_2 transformation is depicted in green, while the water/steam transformation is shown in blue. The enthalpy scale is referenced to water, and the sCO_2 enthalpy scale has been adjusted to match Δh_{H_2O} in the heat exchanger, ensuring clearer visualization.

heat exchanger is selected to avoid two-phase flow conditions in the heat exchanger itself. The sCO_2 re-injection pressure is optimized as well. A lower injection pressure increases the turbine power but results in lower injection density and hence a lower thermosyphon effect.
In order to increase the reliability of the code, the following adimensional parameter (bounded between 0 and 1) has been optimized instead of $T_{CO_2 max}$:

$$T_{SG\%} = \frac{T_{CO_2 max} - T_{lim_-}}{T_{lim_+} - T_{lim_-}} \tag{4.6}$$

T_{lim_+} and T_{lim_-} are the upper and lower limit that $T_{CO_2 max}$ can physically reach, being constrained by the requirements on T_{steam} and by the pressure limits of the cycle:

$$\begin{aligned} T_{lim_-} &= T_{steam} + \Delta T_{HE} \\ T_{lim_+} &= T(P_{max}) \end{aligned} \tag{4.7}$$

Where ΔT_{HE} is the temperature difference between water and sCO_2 in the heat exchanger and $T(P_{max})$ is the temperature that can be reached by compressing the CO_2 to the maximum pressure allowable in the cycle. In this study such pressure has been set to 500 bar, which is twice the current limiting pressure of the industry available heat exchangers [10]. This has been done in order not to limit excessively the scope of the analysis as heat exchangers with higer operating temperatures can become available in future years.

b. Standalone sCO_2 high temperature heat pump (*Fig 4.1*.b)

The model just described applies also to the system depicted in *Fig 4.1*.b. The only difference is the addition of a low-pressure turbine that provides the work required from the HTHP. The ratio between the flow rates in the LP and the HP sections can be calculated considering the energy balance:

$$\dot{m}_{turb_{LP\%}} = \frac{\Delta h_{turb_{LP}}}{\Delta h_{comp} - \Delta h_{turb_{HP}}} \tag{4.8}$$

Considering this definition, *Eq 4.4* can be extended for this system as:

$$\dot{m}_{ratio} = \frac{x_{exp}}{\dot{m}_{H_2O_{ratio}} \left(1 + \dot{m}_{turb_{LP\%}}\right)} \tag{4.9}$$

The optimization of this system only relies on $\dot{m}_{ratio}$ as the COP is not calculated as no external energy source is needed for the system to work, eliminating the need for a multi-objective optimization.
Some fixed parameters were assumed in the model for both CO_2 based configurations. They are listed in the table below:

Table 4.2: CO_2 based HTHP Fixed Parameters

Symbol	Description	Value
η_{comp}	Compressor Efficiency	0.8
η_{turb}	Turbine Efficiency	0.75
η_{pump}	Water pump Efficiency	0.8
T_0	Temperature at the inlet of the well	35°C
ΔT_{HE}	Temperature difference between the water and sCO_2 in the heat exchanger (see *Fig 4.1*)	8°C

c. Standard heat pump connected to the well water circuit (*Fig 4.1*.c)

In this setup, water serves as the designated working fluid within the geothermal well. The heated water is directed to supply the evaporator of a traditional regenerative heat pump. Steam generation occurs in the High-Pressure (HP) condenser, modeled as a shell and tube heat exchanger where the water from the geothermal well flows inside the pipes. Various alternative working fluids have undergone testing for the HTHP to determine the most suitable option for meeting the system's requirements. To determine the optimal water flow rate within the well, the temperature range of the water in the HP evaporator ($Range_EVA$ in *Fig 4.2*) can be optimize to minimize x_{min}. The efficiency of the regenerator was fixed at 0.5 as a parameter in the system.

d. Direct compression of steam generated by the well water flash (*Fig 4.1*.d)

In this setup, the hot water extracted from the well is directly flashed via a valve in a steam cylinder. Subsequently, the resulting steam is compressed to attain the desired pressure and temperature levels, tailored to the specific requirements of the industrial process. To enhance the overall process efficiency, a proposed multistage inter-cooled compression is employed, with each inter-cooler utilizing the stream of saturated liquid returning from the plant as a coolant.

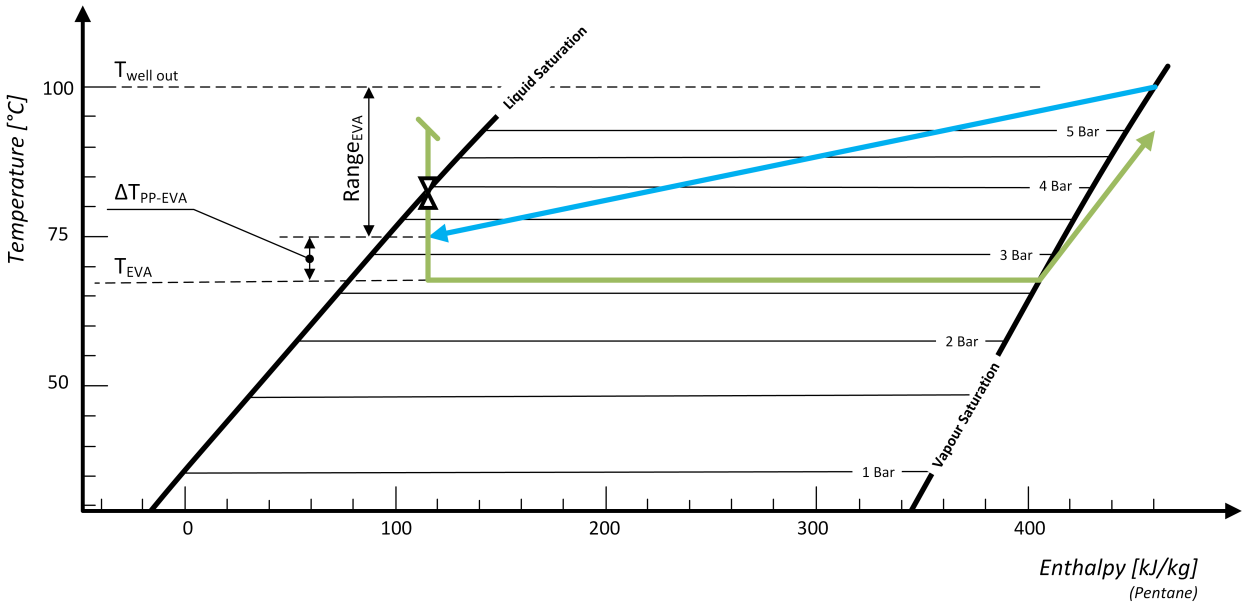

Figure 4.2: Diagram illustrating the temperature profile in the high-pressure (HP) evaporator. The HP working fluid (n-pentane in this instance) is denoted in green, while geothermal water is represented in blue. The enthalpy scale and saturation lines are based on n-pentane, with the water enthalpy scale adjusted to match $\Delta h_{pentane} = \Delta h_{H_2O}$ in the heat exchanger for enhanced visualization.

The saturation temperature inside the cylinder (T_{GC}) is identified in the optimization process that minimizes x_{min}. In fact, in contrast to $T_{CO_2 max}$, an increase in T_{GC} will result in reduced vapor production during the flash process, whereas its decrease means that the compression power required to achieve the desired T_{steam} will increase.
Again following the same reasoning followed for $T_{CO_2 max}$, the optimization has been performed on an adimensional parameter bounded between 0 and 1:

$$T_{GC\%} = \frac{T_{GC max} - T_{lim_-}}{T_{lim_+} - T_{lim_-}} \tag{4.10}$$

where this time:

$$\begin{aligned} T_{lim_-} &= T_{trip} \\ T_{lim_+} &= T_{well_{out}} \end{aligned} \tag{4.11}$$

Where $T_{well_{out}}$ is the temperature of the water at the outlet of the well and T_{trip} is the temperature of the triple point of water (0.01°C) under which ice formation will prevent the flashing to occur.
To conclude, for each water based HTHP the following fixed parameters have been imposed:

Table 4.3: Water based HTHP Fixed Parameters

Symbol	Description	Value
η_{comp}	Compressor Efficiency	0.8
ΔT_{pp}	THeat exchangers pinch points	10°C

4.3 Results

Standalone CO_2 configuration

Fig 4.1 shows the behavior of the standalone sCO_2 system for an 800m deep well and 90°C rock temperature. Density was used instead of pressure in optimizing the input condition of the BHE for stability reasons, but the two parameters are related. From the figure, a clear optimal condition emerges for $\rho_{in} \approx 600 kg/m^3$ for which $\dot{m}_{ratio}$ is maximum. Unfortunately, even in at the optimum $\dot{m}_{ratio}$ is extremely low. *Tab 4.1* displays the expected values of flow rates that has to be circulated in the well to produce 1kg/s of steam, for the sake of clarity.

Table 4.1: Well flow rate to produce 1kg/s of steam in optimal condition *(800m deep well and 90°C rock temperature)*

Configuration	Well Flow Rate
Direct sCO_2 heat pump (*Fig 4.1*.a)	16.7 kg/s
Standalone sCO_2 heat pump (*Fig 4.1*.b)	220 kg/s
Indirect ORC heat pump (*Fig 4.1*.c)	3.6 kg/s
Direct steam generation (*Fig 4.1*.d)	4.8 kg/s

The huge amount of fluid that must be circulated is mainly caused by the LP turbine which needs more than 90% of the overall flow to drive the HTHP in the optimal condition (right-hand side of *Fig 4.1*). This makes this configuration extremely impractical and surely uneconomical as it will probably require a great number of wells to handle the expected flow rate. For this reason it has been excluded from the following analysis.

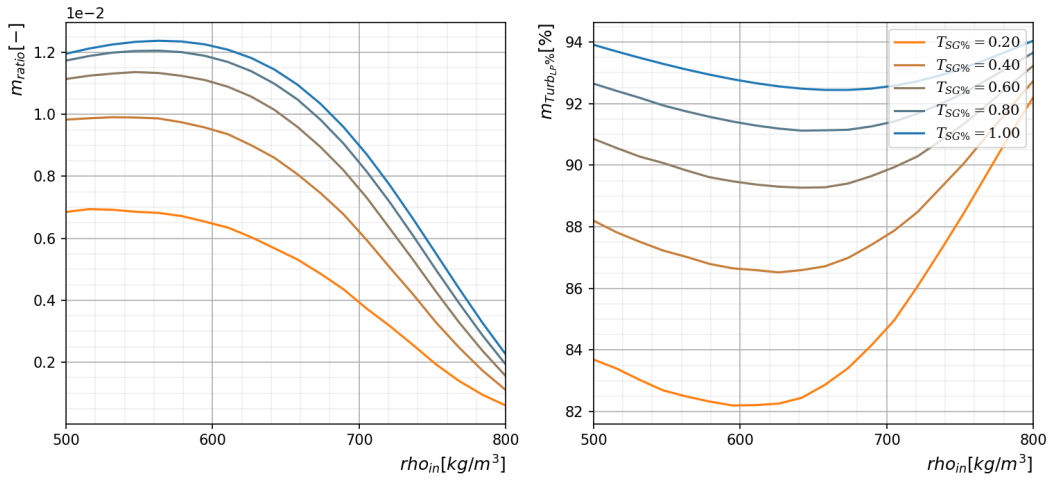

Figure 4.1: $\dot{m}_{ratio}$ and $\dot{m}_{turb_{LP\%}}$ relation with ρ_{in} and $T_{SG\%}$ for standalone sCO_2 configuration considering an 800m deep well and 90°C rock temperature

Optimization of other HTHP

To understand how the optimization will proceeds is possible to analyze how the effect of the optimization parameter over the heat pump behaviour for a specific condition (*a 90°C reservoir 800m deep*).

As depicted in *Fig 4.2*.a, for the direct CO_2 HTHP, an increase in $T_{SG\%}$ results in a simultaneous increase in both the COP and $\dot{m}_{ratio}$. This observation suggests that, in this specific geological context, there is no distinct minimum value for x_{min}. Instead, the performance of the configuration is constrained by its maximum pressure.
Conversely, for the *direct steam generation* and *indirect heat pumps*, it becomes apparent that COP and $\dot{m}_{ratio}$ has opposite behaviors. This divergence implies that a minimum for x_{min} can be identified through the optimization process, with the exact position of this optimum depending on the chosen value for Ω.

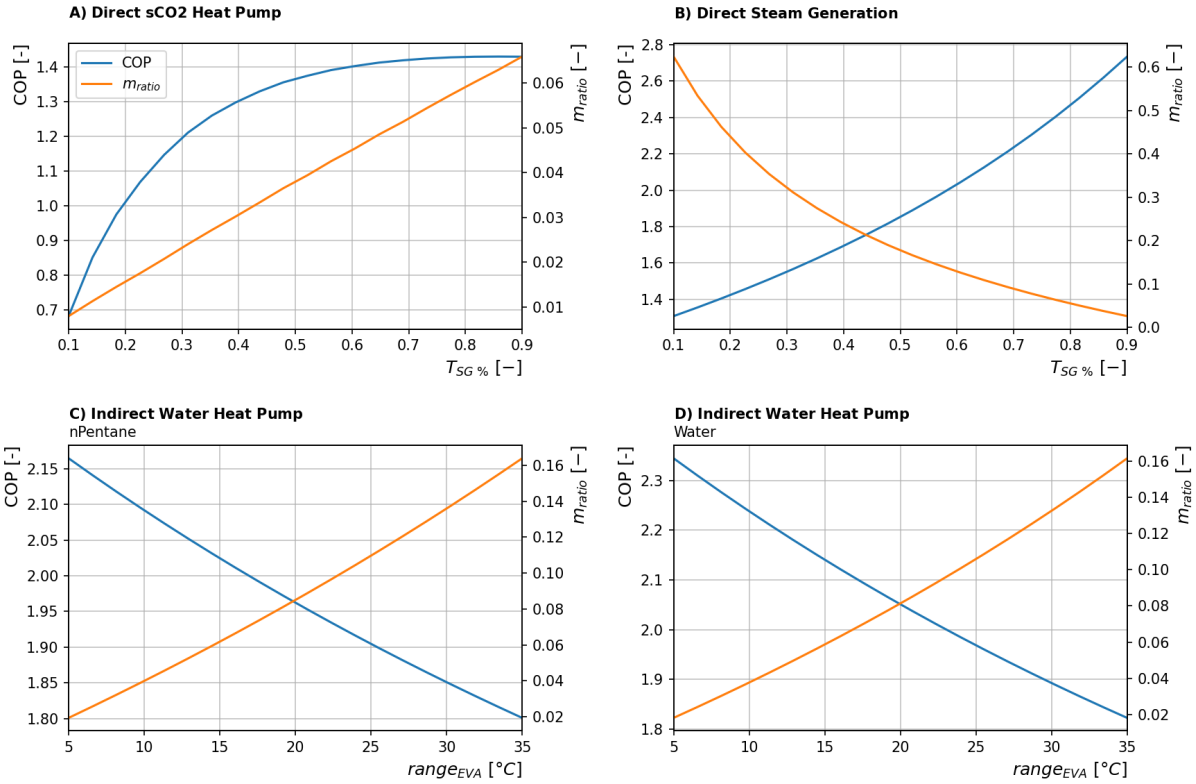

Figure 4.2: COP and $\dot{m}_{ratio}$ for various system configurations considering an 800m well depth and 90°C rock temperature: A) sCO_2 direct HTHP powered by an electric motor (*Fig 4.1*.a). B) Direct water HTHP (*Fig 4.1*.d). C) Indirect ORC heat pump with *n-Pentane* as the ORC fluid (*Fig 4.1*.c). D) Indirect ORC heat pump with *water* as the ORC fluid (*Fig 4.1*.c).

The fact that CO_2 based systems cannot be optimized while water based system can is explained noting that, in the case of water-based systems, the COP and $\dot{m}_{ratio}$ are mathematically related, ensuring their inverse trends. In fact, for the energy conservation within the entire system, it can be deduced that:

$$\dot{Q}_{well} + \dot{W}_{net} = \dot{Q}_{steam} \tag{4.12}$$

Rearranging:

$$\Delta h_{ratio} \dot{m}_{ratio} = \frac{COP}{COP - 1} \tag{4.13}$$

Where $\Delta h_{ratio} = \Delta h_{steam} / \Delta h_{well}$ does not depend on the surface plant configuration. Taking the

derivative of *Eq 4.13*:

$$\frac{d\dot{m}_{ratio}}{dCOP} = -\frac{1}{\Delta h_{ratio}\,(COP-1)^2} \tag{4.14}$$

Which indicates that $d\dot{m}_{ratio}/dCOP$ is negative, meaning that $\dot{m}_{ratio}$ decrease as COP increase, given that Δh_{well} is positive, hence the well is extracting energy.
However, what just said for water based systems do not hold for CO_2 based systems due to the inclusion of a cooler, which makes *Eq 4.12* no more valid, explaining why an optimal x_{min} cannot be found.

Configurations Comparison

Fig 4.3 summarizes how the optimization parameter Ω impacts various configurations at different rock temperatures. Depth variations are excluded for the water-based BHE system due to water's incompressibility, as is clear from. The sCO_2 based heat pump is unaffected by Ω due to the absence of a clear maximum, as shown in *Fig 4.2*.a. Conversely, water-based systems respond to changes in Ω as expected.

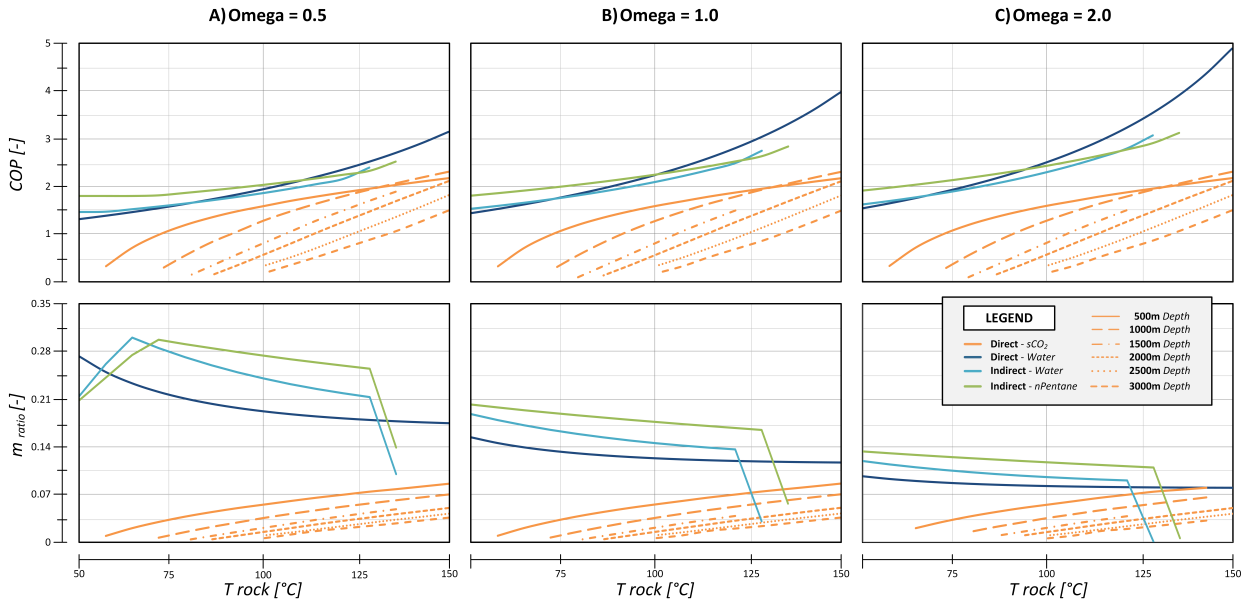

Figure 4.3: Effect of Ω on the optimization process for different rocks temperature and well depth.

Higher rock temperatures generally improve COP for all systems, but this affects $\dot{m}_{ratio}$ differently, increasing for CO_2 based systems while decreasing for water based systems as COP increase as explained earlier.
Increased depth diminishes performance for sCO_2 systems due to sCO_2 expansion and cooling in the *ascending section*. For most cases, the direct water configuration excels at rock temperatures above 100°C, while indirect configurations perform better at lower temperatures.

Depth-T_{rocks} maps

Figures 9 and 10 depict the behaviour of COP and $\dot{m}_{ratio}$ with changing depth and rock temperature for Ω=1. The water-based configurations display minimal depth dependence, whereas for the direct sCO_2 configuration, depth proves to be a significant factor due to the compressibility of CO_2 .

Increasing depth amplifies the pressure difference, favoring thermosiphon conditions but reducing the temperature of the fluid at the outlet of the well requiring further compression.
Notice that, due to the fact that the effectiveness of sCO_2 based HTHP is limited by its maximum pressure, neither having an higher outlet pressure from the well is beneficial for the surface plant, leaving less space for compressing the fluid before the limiting pressure is reached.

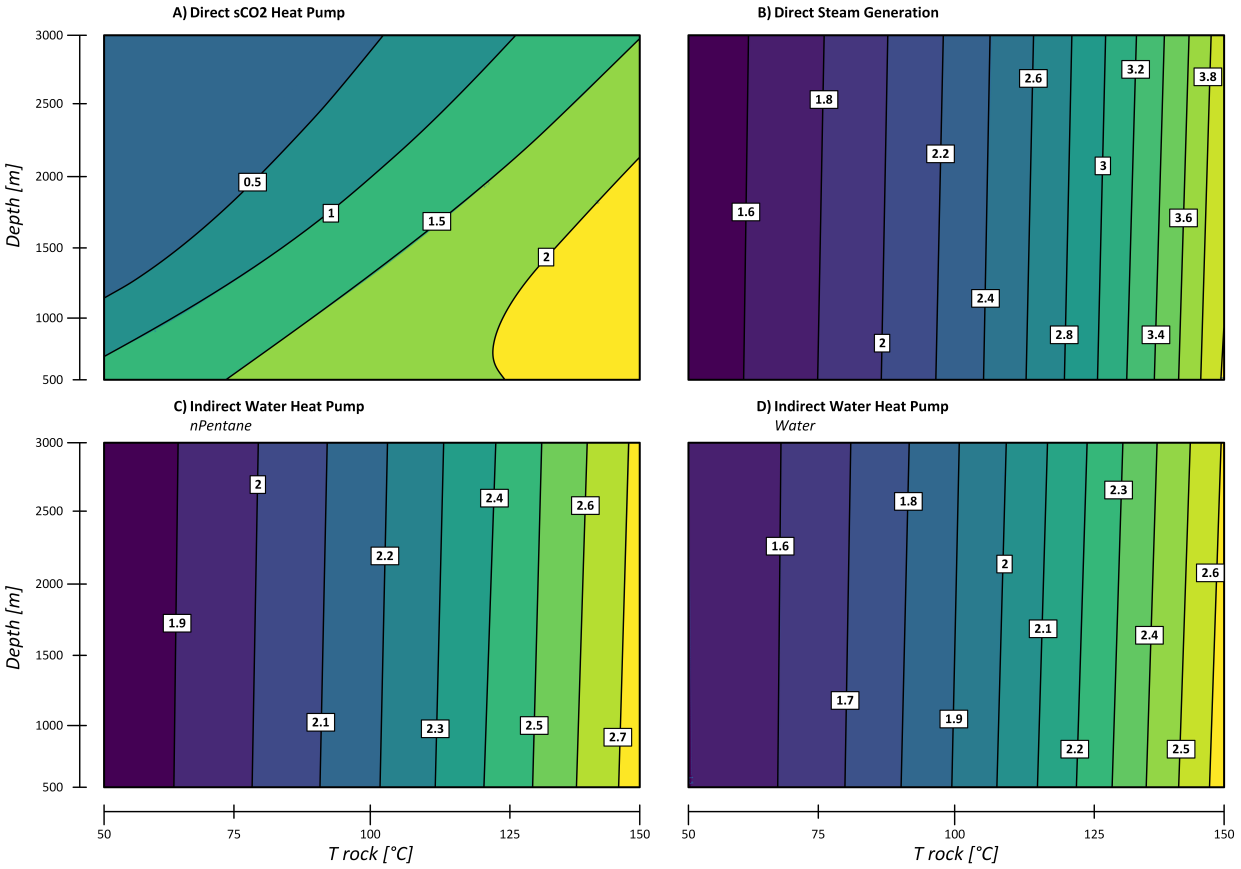

Figure 4.4: *COP* relation with resource depth and temperature for different surface plant configurations

On the other hand, water based configurations exhibit remarkably high COP. Direct steam generation, for instance, achieves a COP exceeding 3.5 with a 90°C resource temperature. Conversely, the sCO_2 heat pump attains a maximum COP of over 2.
In Figure 10, isoline contours are utilized to facilitate ratio readings, with fractions indicating the required fluid circulation for steam production. For instance, 1/100 implies that 1 kg/s of steam necessitates 100 kg/s of CO_2 circulation in the well.
Finally, Figure 11 demonstrates how these maps aid in estimating the behavior of a geothermal HTHP based on the geological conditions of the chosen location. Superimposing real geothermal gradients [11]–[15] onto the graph enables the identification of anticipated COP and $\dot{m}_{ratio}$ values at varying depths.
For example, for a direct sCO_2 heat pump installed in the location linked to gradient d.1 (southern Tuscany), a maximum COP of 1 can be anticipated for a 1500 m depth well, while a direct water plant in the same location could achieve a COP as high as 2.2 with the same well depth.

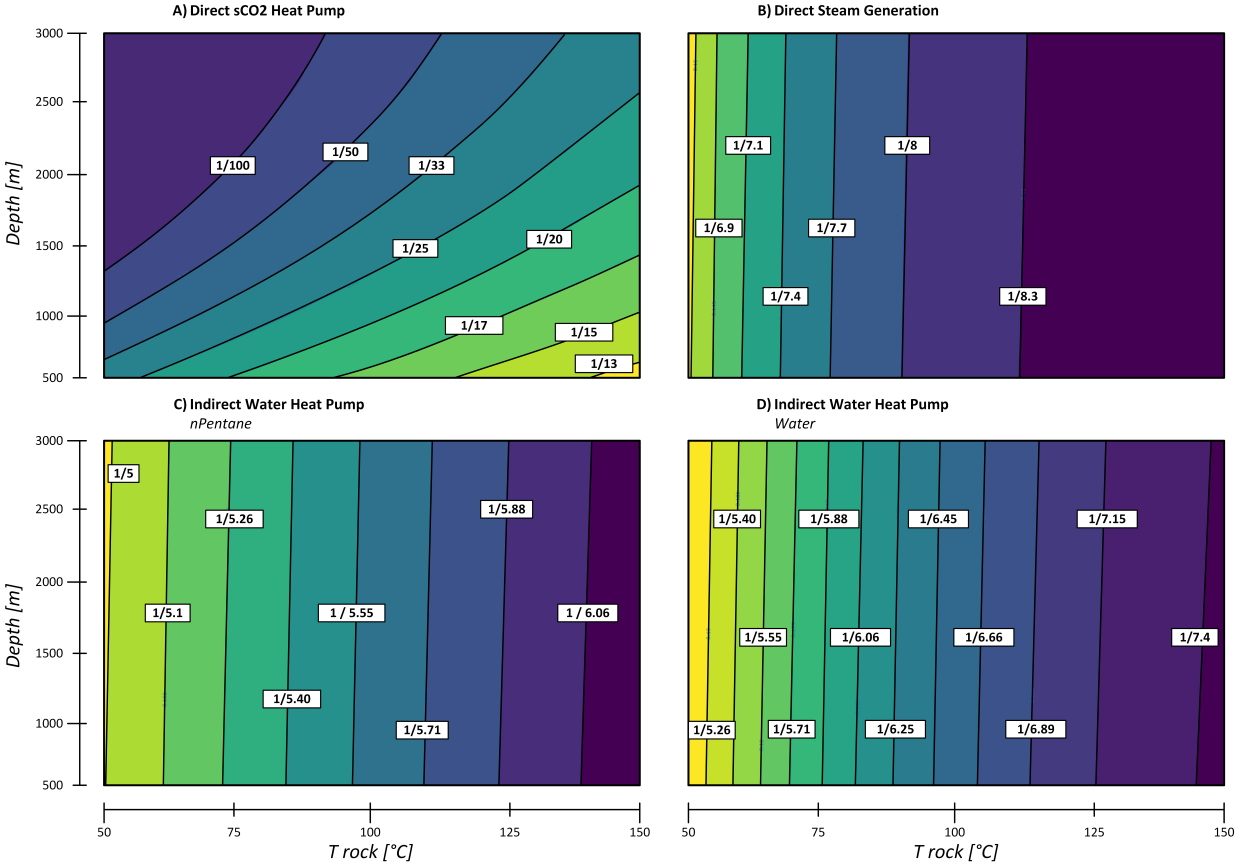

Figure 4.5: $\dot{m}_{ratio}$ relation with resource depth and temperature for different surface plant configurations: A) sCO2 direct HTHP powered by an electric motor (*Fig 4.1*.a). B) Direct Water HTHP (*Fig 4.1*.d). C) Indirect ORC heat pump with nPentane as ORC fluid (*Fig 4.1*.c). D) Indirect ORC heat pump with Water as ORC fluid (*Fig 4.1*.c).

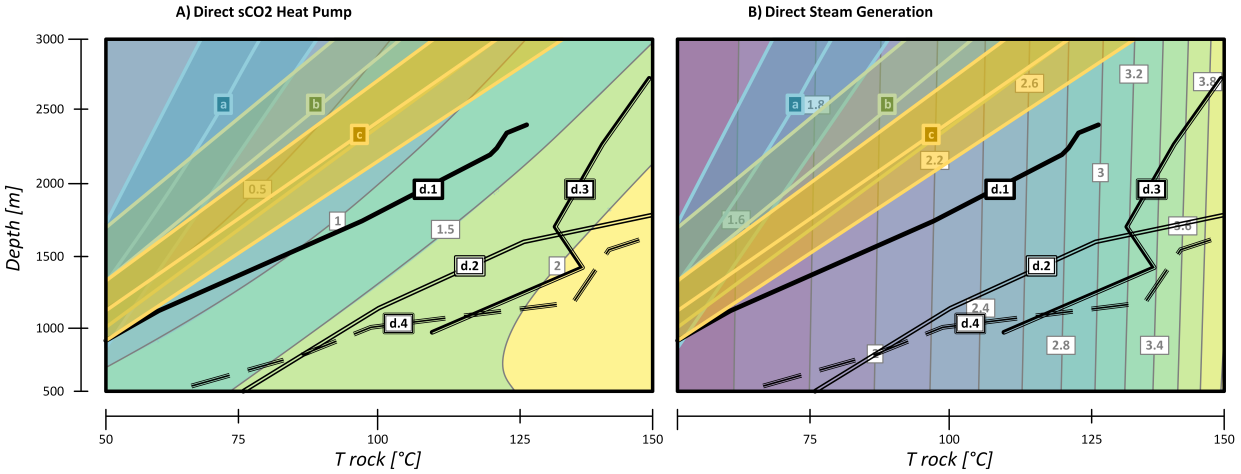

Figure 4.6: Real geothermal gradients superimposed on estimated maximum COP from figure 8. Gradients a, b and c are mean and standard distribution from multiple exploration wells in: a) Absheron peninsula (Azerbaijan) [11] and in Alberta (Canada) [12], b) Netherlands [13], c) Daqing Oilfield, Northeast China [14]. Gradients d.1, d.2, d.3 and d.4 are well log from a south Tuscany geothermal field [15]

4.4 Conclusions

This study presents a comprehensive design procedure for predicting the thermodynamic behavior of a general geothermal high-temperature heat pump industrial heat production.
Two correlation parameters, *depth* and T_{rocks}, were introduced to optimize the well conditions during the design phase.
A crucial aspect of this research is the introduction of a generalized approach that encompasses diverse heat extraction configurations, ranging from the sCO_2 heat pump to standard water-based systems. Key findings from this work include:

- Illustration of multiple solutions for producing high-temperature steam (at 12 barg) using a geothermal-fueled high-temperature heat pump, with water-based systems proving more promising than sCO_2 cycles from a thermodynamic standpoint.
- The utility of the maps depicted in figures 9 and 10, aiding designers in assessing the potential of such systems based on existing geological conditions.
- Promising thermodynamic performance of water-based configurations, warranting a thorough thermo-economic analysis to evaluate the feasibility of the solution.
- The in-feasibility of CO_2 based systems, particularly as standalone solutions, due to limitations in heat extraction. The conversion of enthalpy gain in the reservoir into pressure difference in the ascending section is very appealing to power production but not for heat upgrade configurations as the fluid must be pressurize again almost to the reservoir pressure just to get to the same temperature level that the liquid naturally achieve.
- Finally, the analysis conducted herein highlights the attractiveness of the anticipated COP values for the proposed configuration. As state-of-the-art technology struggles to achieve a COP of 2 for steam production, in some very favourable conditions analyzed configurations could surpass a COP of 3.5.

References

[1] P. Ungar, D. Fiaschi, G. Manfrida, and L. Talluri, "Thermodynamic Assessment of Geothermal High-Temperature Heat Pumps for Industrial Steam Production," *Available at SSRN*, 2023. [Online]. Available: https://dx.doi.org/10.2139/ssrn.4350038.

[2] IEA, *Heating*, 2022. [Online]. Available: https://www.iea.org/reports/heating.

[3] IEA-IETS, "Application of Industrial Heat Pumps," Tech. Rep., 2014.

[4] A. Honore, "Decarbonization and industrial demand for gas in Europe," Oxford Institute for Energy Studies, Oxford, United Kingdom, Tech. Rep., May 2019. DOI: 10.26889/9781784671396.

[5] C. Arpagaus, F. Bless, M. Uhlmann, J. Schiffmann, and S. S. Bertsch, "High temperature heat pumps: Market overview, state of the art, research status, refrigerants, and application potentials," *Energy*, vol. 152, pp. 985–1010, Jun. 2018, ISSN: 03605442. DOI: 10.1016/j.energy.2018.03.166.

[6] B. Zühlsdorf, F. Bühler, M. Bantle, and B. Elmegaard, "Analysis of technologies and potentials for heat pump-based process heat supply above 150°C," *Energy Conversion and Management: X*, Apr. 2019, ISSN: 25901745. DOI: 10.1016/j.ecmx.2019.100011.

[7] D. Brown, "A Hot Dry Rock Geothermal Energy Concept Utilizing Supercritical CO2 Instead of Water," *Twenty-Fifth Workshop on Geothermal Resevoir Engineering*, 2000, ISSN: 2195-9706.

[8] M. Shamoushaki, P. H. Niknam, L. Talluri, G. Manfrida, and D. Fiaschi, "Development of Cost Correlations for the Economic Assessment of Power Plant Equipment," *Energies*, vol. 14, no. 9, p. 2665, May 2021, ISSN: 1996-1073. DOI: 10.3390/en14092665.

[9] X. Xu, M. Abeysekera, C. Gutschi, *et al.*, "Quantifying flexibility of industrial steam systems for ancillary services: a case study of an integrated pulp and paper mill," *IET Energy Systems Integration*, vol. 2, no. 2, pp. 124–132, Jun. 2020, ISSN: 2516-8401. DOI: 10.1049/iet-esi.2019.0082.

[10] N. T. Weiland, B. W. Lance, and S. R. Pidaparti, "sCO2 Power Cycle Component Cost Correlations From DOE Data Spanning Multiple Scales and Applications," in *ASME Turbo Expo 2019: Turbomachinery Technical Conference and Exposition*, Phoenix, Arizona, USA: American Society of Mechanical Engineers, Jun. 2019, ISBN: 978-0-7918-5872-1. DOI: 10.1115/GT2019-90493.

[11] A. V. Mammadova, "Temperature Distribution and Heat Flow Density Estimation in Geothermal Areas of Absheron Peninsula," *International Journal of Terrestrial Heat Flow and Applications*, vol. 3, no. 1, pp. 26–31, Mar. 2020, ISSN: 2595-4180. DOI: 10.31214/ijthfa.v3i1.44. [Online]. Available: http://ijthfa.com/index.php/journal/article/view/44.

[12] K. Huang, C. Hickson, D. Cotterill, and Y. Champollion, "Geothermal assessment of target formations using recorded temperature measurements for the alberta no. 1 geothermal project," *Applied Sciences (Switzerland)*, vol. 11, no. 2, pp. 1–10, Jan. 2021, ISSN: 20763417. DOI: 10.3390/app11020608.

[13] E. Békési, M. Struijk, D. Bonté, *et al.*, "An updated geothermal model of the Dutch subsurface based on inversion of temperature data," *Geothermics*, vol. 88, p. 101 880, Nov. 2020, ISSN: 03756505. DOI: 10.1016/j.geothermics.2020.101880.

[14] G. Jiang, Y. Wang, Y. Shi, C. Zhang, X. Tang, and S. Hu, "Estimate of hot dry rock geothermal resource in Daqing Oilfield, Northeast China," *Energies*, vol. 9, no. 10, Oct. 2016, ISSN: 19961073. DOI: 10.3390/en9100731.

[15] G. Buonasorte, R. Cataldi, A. Ceccarelli, *et al.*, "Ricerca ed esplorazione nell'area geotermica di Torre Alfina (Lazio-Umbria)," *Italian Journal of Geosciences*, vol. 107, no. 2, pp. 265–337, Jan. 1988, ISSN: 2038-1719.

Appendix A

Exergo-Economic Analysis Tool

This section describes the Exergo-Economic Analysis tool developed within the scope of this PhD thesis and used to perform calculations presented in *Chapter 4*. The description that follows is a revised and expanded version of the paper *Development of an exergo-economic and exergo-environmental tool for power plant assessment: evaluation of a geothermal case study* [1] which has been presented at the ECOS 2021 conference in Taormina.

A.1 Introduction

In pursuit of the objective to limit global warming to 1.5°C compared to pre-industrial levels, numerous countries are embarking on the path of cleaner and renewable energy generation. However, in the short term, reliance solely on renewable energies may prove insufficient. Hence, it becomes imperative to focus on enhancing energy efficiency and optimizing industrial systems. Energy system optimization encompasses a multifaceted approach, encompassing thermodynamic optimization, cost analysis, and environmental considerations. It pertains to both energy systems and industrial projects, with the aim of determining the most suitable design solution aligned with specific objectives, whether it's reducing production costs or minimizing environmental impact.
Within the realm of energy system optimization, two methodologies have gained prominence since the 1980s: Exergo-Economic Analysis (EEA) and Exergo-Environmental Analysis (EEvA). These methodologies fuse exergy analysis with economic and environmental assessments, respectively. Exergy represents the net available energy that can be transformed into useful work during a thermodynamic process, factoring in interactions with the environment. Exergy analysis embodies the principles of both the first and second laws of thermodynamics, accounting for irreversible processes. Exergy losses and destruction refer to energy that isn't efficiently converted into useful work. Losses encompass energy dissipated to the environment, including heat losses and the discharge of fluid flows with non-zero energy, alongside direct work losses. Exergy destruction is linked to the irreversibility of systems or components, such as friction losses and heat transfer from high- to low-temperature fluids. As a result, exergy analysis has emerged as a potent tool for assessing energy conversion systems, proving instrumental in refining the design of power plants by identifying system inefficiencies. Integrating this powerful tool with economic and environmental assessments yields a robust and dependable method for pinpointing components or systems with the most substantial economic and environmental impacts.

More specifically, the integration of exergy analysis and economic evaluation gives rise to exergo-economic analysis. This method is employed to ascertain the production costs of all services delivered by specific system elements, whether it's electricity or heat production. The exergo-economic approach adheres to the cost balance equation, which can be formulated for each component within the system as follows:

$$\sum_{prod} \dot{C}_{k,p} = \sum_{fuels} \dot{C}_{k,f} + \dot{Z}_k \tag{A.1}$$

Where:

- $\dot{C}_{k,p}$ and $\dot{C}_{k,f}$ are the cost rates associated with the exergy products (p) and fuels (f), respectively.
- $\dot{Z}_k$ is the investment cost for the k-th component.

Much like exergo-economic analysis, exergo-environmental analysis integrates exergy analysis with an assessment of environmental impact. This environmental assessment is conducted using life cycle assessment (LCA) methodologies, allowing for the evaluation of how each component within a system affects the environment. Subsequently, these environmental impacts can be attributed to each exergy stream in the analyzed system, providing insights into the combined effects of resource utilization, including materials, production, and services, as well as the impacts stemming from component inefficiencies and irreversibilities. Similar to exergo-economic analysis, exergo-environmental analysis relies on the environmental balance equation (*Eq A.2*) as a fundamental tool.

$$\sum_{prod} \dot{B}_{k,p} = \sum_{fuels} \dot{B}_{k,f} + \dot{Y}_k \tag{A.2}$$

Where:

- $\dot{B}_{k,p}$ and $\dot{B}_{k,f}$ are the environmental impact rates associated with the exergy products (p) and fuels (f), respectively.
- $\dot{Z}_k$ is the environmental impact of the k-th component.

Exergo-economic and exergo-environmental analyses have found diverse applications across various fields, including energy systems such as gas turbines [2], steam power plants [3], combined cycles [4], organic Rankine cycles [5], [6], inverse cycles [7], and in renewable energy assessments, such as solar [8], [9], biomass [10], and geothermal power plants [11]–[13]. These analyses have also been applied to storage assessment applications, including thermo-electric storage [14], [15] and phase change materials [16].

The development of these analyses often relies on in-house coding [17], starting with commercial software such as Aspen Plus, EES [18], Matlab [19], Unisim Design [20], and Ebsilon for thermodynamic analysis. Subsequently, exergy, exergo-economic, and exergo-environmental analyses are computed independently. Only a few tentative codes have been developed to streamline these processes. One such code was developed by Zhao in 2015 during his Ph.D. work, involving the creation of a computer program for exergo-economic analysis of energy conversion systems. The inputs for this software, which are the thermodynamic variables of the systems, were obtained from Aspen

Plus but could have been derived from other simulation software. The exergo-economic software was developed in C++ programming using Microsoft Visual Studio 2008. While this software demonstrated high capabilities through the simulation of several case studies, it is not currently available online.

The only available online software for exergo-economic assessment is TAESS, Thermo-economic Analysis and Energy Systems Software, developed by CIRCE and the Department of Mechanical Engineering at the University of Zaragoza. TAESS features a Microsoft Excel 2007/2010 interface and requires input data, including the thermodynamic model and system configuration. Once the system is defined within the Excel environment, and all thermodynamic properties of streams are accurately reported, the code automatically generates a Fuel-Product table and assesses cost structures. While this software has been utilized by several researchers [21], [22] for exergo-economic analysis, it has not gained widespread adoption, possibly due to its less intuitive interface.

The literature review indicates a growing interest in exergo-economic and exergo-environmental analyses for assessing energy systems. However, it appears that a clear and comprehensive design tool for these analyses, offering simplicity and flexibility, is lacking. Therefore, the main objectives of this study are (i) to develop a user-friendly exergy-based tool for exergo-economic and exergo-environmental analyses and (ii) to provide a clear explanation of its features.

The current version of the software does not yet include a drag-and-drop user interface. However, the beta version is already accessible at https://pypi.org/project/3ETool/ and can be freely tested by any researcher.

A.2 Methodology

The methodology outlined below is primarily discussed in the context of exergo-economic analysis. Nonetheless, owing to the evident symmetry between them, wich is evident comparing *Eq A.1* and *Eq A.2*, both exergo-environmental and exergo-economic analyses are conducted using the same methodology but with distinct input sets as will be detailed in this section.

A.2.1 Inputs Definition

To conduct the analysis, the application necessitates four primary inputs:

1. The physical topology of the plant.
2. Exergy flows for each stream (e.g., $\dot{e}_x$ [kW]).
3. The cost or environmental impact of each plant component (e.g., $\dot{Z}_k$ [€/s] or $\dot{Y}_k$ [Pts/s]).
4. The specific cost or environmental impact of each connection originating from the ambient (e.g., $\dot{c}_0$ [€/kJ] or $\dot{b}_0$ [Pts/kJ]).

Plant Topology

In the program's convention, the plant's topology is represented as a *directed graph*. This means that a set of *blocks*, representing the plant's components, is linked by various *connections*, representing the material streams or energy flows.
For each block, users must specify the type of the corresponding component (e.g., "expander" or "valve") to enable the program to correctly identify product and fuel streams. *Fig A.1* illustrates how this description applies to a simple regenerated gas turbine system.

A)

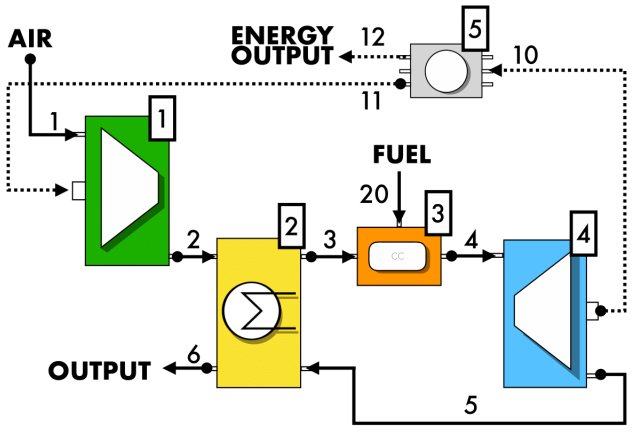

B)

Blocks

ID	Name	Type
1	*Compressor*	*Compressor*
2	*Regenerator*	*Heat Exchanger*
3	*Combustion Chamber*	*Combustion Chamber*
4	*Turbine*	*Expander*
5	*Power Shaft*	*Generic*

Connections

ID	Name	From ID	To ID
1	*Air Inlet*	*Ambient*	*1*
2	*Compressor Outlet*	*1*	*2*
3	*CC Inlet*	*2*	*3*
4	*Turbine Inlet*	*3*	*4*
5	*Turbine Outet*	*4*	*2*
6	*Air Outlet*	*2*	*Ambient*
10	*Turbine Power Output*	*4*	*5*
11	*Comp Power Input*	*5*	*1*
12	*Net Power Output*	*5*	*Output*

Figure A.1: A regenerated gas turbine power plant described following our topology convention. A) *Directed graph* representation, and B) *Block* and *connections* representation

Exergy Flows

The program requires the exergy values for each stream listed in the connection list. These values can be extracted from the software used for thermodynamic modeling of the components and must be provided to the program via an Excel sheet or a *.dat* file.

Component and Connection Costs

Users must supply the investment cost or environmental impact (for exergo-environmental analysis) of each component listed in the block inventory. This cost can be directly input by users or calculated by the software using built-in cost correlations. In the latter case, users must provide the parameters for the cost correlation, such as the surface area of a heat exchanger. If no cost data is provided for the input streams of the system, the program will automatically set it to 0.
The user must input these parameters via a *precompiled* Excel sheet. However, this method has proven to be error-prone, particularly for defining the plant's topology. Therefore, a more intuitive drag-and-drop user interface is currently in development and is expected to significantly enhance the accuracy of calculations, especially for users who may lack experience and struggle to immediately evaluate the correctness of the results obtained.

A.2.2 Cost Matrix Generation

The objective of an exergo-economic analysis is to determine the specific cost (in €/kW) associated with each exergy stream within the process. This is achieved by solving a linear system composed of the cost balance equation for each component. However, balance equations alone may not suffice to fully close the system, especially when the process involves more streams than components. To address this issue, many authors introduce a set of auxiliary equations to make the system solvable. This work adopts a slightly different approach. Instead of solving the system to find the specific cost of each connection, we treat the cost of the product of each block as the unknowns. This implicitly assumes that, in the case of a component producing multiple products, all of these products have the same specific cost. This assumption aligns with the *"P principle"* described by Lazzaretto and Tsatsaronis in defining the SPECO methodology [23].
The advantage of this approach is that it obviates the need for auxiliary equations in system definition. This simplifies the matrix generation algorithm and reduces the matrix's dimensions. The resulting system from this new approach consists solely of the cost balance equations for each component, as represented in *Eq A.1*, which can be rewritten as:

$$\sum_{prod} \dot{c}_{k,p}\dot{e}_{k,p} = \sum_{fuels} \dot{c}_{k,f}\dot{e}_{k,f} + \dot{Z}_k \tag{A.3}$$

Or, considering the "P principle" assumption:

$$\dot{c}_k \sum_{prod} \dot{e}_{k,p} = \sum_{fuels} \dot{c}_{k,f}\dot{e}_{k,f} + \dot{Z}_k \tag{A.4}$$

In *Eq A.4*, $\dot{c}_{k,f}$, specifically the specific cost of fuel, can either be a known value if the fuel is a global input of the process, or equal to $\dot{c}_k$ of the component that generates such a fuel stream.

Consequently, the summation over fuels in *Eq A.4* can be rewritten as:

$$\dot{c}_k \sum_{i=prods} \dot{e}_{i,k} - \sum_{j=f_{int}} \dot{c}_j \dot{e}_{k,j} = \sum_{j_0=f_{ext}} \dot{c}_{j_0} \dot{e}_{k,j_0} + \dot{Z}_k \tag{A.5}$$

Where:

- f_{ext} stands for *external fuels*: streams of exergy entering the system from the outside of its boundary, such as the gas entering a combustion chamber. Their cost is known and must be provided by the user. If no cost is provided, the program automatically sets it to 0.
- f_{int} refers to an *internal fuels* hence a stream of exergy that has been generated by another component of the process.
- $\dot{e}_{k,j}$ represents an exergy flow that is a product of the j-th component and fuel for the k-th one. In this framework, j = 0 represents a stream coming from the outside of the system.

Eq A.5 is the balance equation for the k-th component and is used for the matrix generation purpose in our application.
Considering that the system's unknowns comprise the product costs ($\dot{c}_k$), each class *block*, representing a component in the topology, has the capability to generate an array that encapsulates its cost balance equation (*Eq A.5*). These arrays are then assembled to construct the matrix to be solved by another class (named *ArrayHandler*). The arrays are generated following these simple rules:

1. For every internal fuel (f_{int}) and consequently for each input connection originating from another system block, the specific exergy ($\dot{e}_{k,j}$) must be included with a negative sign in the j-th position. Here, j, within our formalism, denotes the index of the block from which the connection originates.
2. The sum ($\sum_{i=prods} \dot{e}_{i,k}$) of the exergies of connections originating from the block is positioned in the k-th location, effectively representing the diagonal of the matrix (each component generates the k-th row of the matrix).
3. The term $\sum_{j_0=f_{ext}} \dot{c}_{j_0} \dot{e}_{k,j_0} + \dot{Z}_k$ is separately collected to form the known variable vector.

Fig A.2 provides a visual representation of this array generation process.

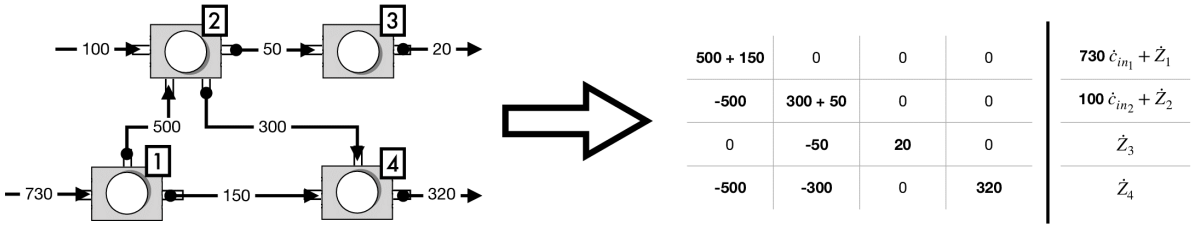

Figure A.2: Example of Array Generation: Each row in the matrix is generated by its corresponding block following the previously outlined procedure. $\dot{c}_{in_i}$ represents the cost of the in-flowing stream to the system, and $\dot{Z}_k$ denotes the cost of the k-th block.

A.2.3 Topology Modification

Unfortunately, directly executing the described calculation on the user-provided topology may lead to incorrect results because, in most applications, the definition of products and fuels may not correspond to the physical inflow and outflow streams from a block. To address this issue, the program autonomously adjusts the topology through a two-step process before running the calculation:

STEP 1: Block fuels and product identification:

The initial step involves ensuring that the input and output connections of each component accurately represent fuels and products, respectively. The program does so employing some *support bocks*. To illustrate how this has been done, let's consider a simple expander, such as the one depicted in *Fig A.3*, as an example.
As explained in many publications [23], [24] the fuel of an expander must be identified as follows:

$$\dot{e}_f = (\dot{e}_{flow_{in}} - \dot{e}_{flow_{out}}) \tag{A.6}$$

Where $\dot{e}_{flow_{in}}$ and $\dot{e}_{flow_{out}}$ are the physical connections while $\dot{e}_f$ is the fuel that should be used in the matrix definition.
Representing an expander in such way is important because the residual exergy that is flowing out from the turbine is not something that the turbine has produced but rather something that the turbine has not utilized, so it should be subtracted from the amount of exergy that the turbine has used.
Moreover, for the same reason, $\dot{e}_{flow_{out}}$ still represents the exergy produced by a component before the turbine (such as a combustion chamber) and should be valued as the cost of the exergy produced by that particular component itself:

$$\dot{c}_f = \dot{c}_{flow_{in}} = \dot{c}_{flow_{out}} \tag{A.7}$$

In the SPECO methodology, *Eq A.7* is called the *"F-Pronciple"*.
The behaviour described in *Eq A.6* and *Eq A.7* is reproduced in the software by introducing a support block at the expander's input and connecting all fluid streams to it, as depicted in *Fig A.3*. To achieve this, each support block is programmed to adjust the exergy value of the stream linked to the primary block to conserve the exergy passing through it:

$$\dot{e}_{main} = \sum \dot{e}_{flow_{in}} - \sum \dot{e}_{flow_{out}} \tag{A.8}$$

Additionally, each support block is set to have no specific investment cost ($\dot{Z}_k = 0$), so that the general cost balance for a component (*Eq A.4*) will become:

$$\dot{c}_k \sum_{prod} \dot{e}_{k,p} = \sum_{fuels} \dot{c}_{k,f} \dot{e}_{k,f} \tag{A.9}$$

Which, considering that from *Eq A.8* results that $\sum_{prod} \dot{e}_{k,p} = \sum_{fuels} \dot{e}_{k,f}$, means that the cost of the products of a support block equals the weighted mean of the cost of the input exergies, which aligns with the prescription of the *F-Principle*.

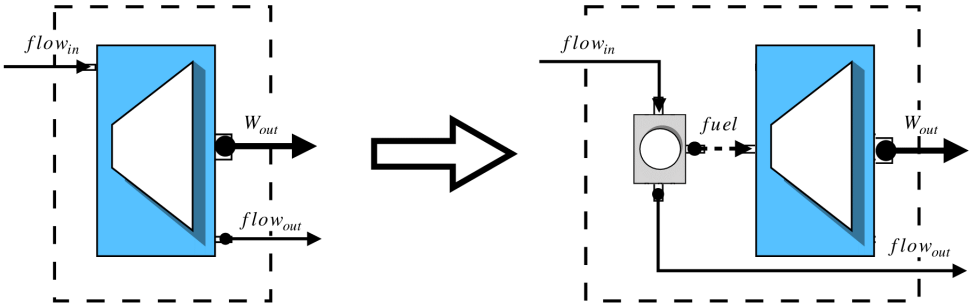

Figure A.3: Generation of Support Blocks for an Expander

This method is applicable in situations where a process's fuel or product is determined by the difference between input and output exergies, and when preserving the associated costs is necessary. The program automatically generates and connects support blocks based on the component type. Solving the system using the matrix created by this set of blocks and support blocks, with input connections designated as "fuels" and outputs as "products," is functionally equivalent to solving the system derived from SPECO analysis. In practice, for standard blocks, the inputs and outputs align with the genuine fuel and product definitions in SPECO, ensuring identical cost balances. Furthermore, as demonstrated, the balances of support blocks correspond to the auxiliary equations of the F-Principle, resulting in the same system.

STEP 2: Product-Fuel Diagram generation:

A second adjustment to the system's topology is necessary to enable the proper redistribution of costs associated with exergy losses within the components. To appreciate the need for this step, it's essential to understand how the program manages exergy loss streams. Therefore, a brief explanation of this issue is provided below.
Exergy loss refers to a stream of exergy leaving the system without contributing to useful work, such as the residual heat in gas turbine exhaust gases or unburned particles exiting a coal boiler. In literature, two primary approaches exist for pricing exergy losses, allowing users to choose the one best suited to their needs:

- $\dot{c}_{loss} = \dot{c}_{fuel}$: This approach, proposed by Lazzaretto and Tsatsaronis for the SPECO methodology, has the advantage if maintaining the *"F-Principle"*. Morover, it assigns an actual cost to the loss stream which is useful in the . However, it does not preserve the overall cost balance of the system. Pricing the loss with $\dot{c}_{loss} \neq 0$ implies that there is a buyer willing to pay that price for the exergy stream, which reduces the price of the actual product of the system, potentially impacting return on investment [1].

- $\dot{c}_{loss} = 0$: This approach resolves the issues associated with the previous approach but does not provide a clear cost for the dispersed energy. It also breaks the *"F-Principle"*, as can be

[1]Discussions of this nature can occasionally be perplexing, particularly for less experienced users. This is mainly because of the fact that what is referenced as the "cost" of the loss is actually, in the perspective of the component, the "price" at which the component sells the outgoing exergy. In this perspective, it's easy to understand that, pricing the losses with $\dot{c}_{loss} \neq 0$ is an economic advantage for the system, despite intuition suggesting otherwise.

seen in the regenerator shown in *Fig A.4*, in which, according to the *"F-Principle"*, $\dot{c}_6$ should theoretically equal $\dot{c}_5$. However, as stream 6 represents an exergy loss, in this case, $\dot{c}_6 = 0$.

This creates a problem in cost redistribution because using the described topology, all cost increases are allocated to the component directly connected to the loss, such as the regenerator, even if it's not the primary source of the loss in this case. To resolve this issue, the topology must be adjusted to align with the fuel-product diagram, as described by Torres and Valero [21]. *Fig A.4* illustrates this transformation for the system in Figure 2.1. After this transformation, any change in $\dot{c}_6$ affects both the fuel cost of the turbine and the regenerator, resulting in a more equitable cost distribution.

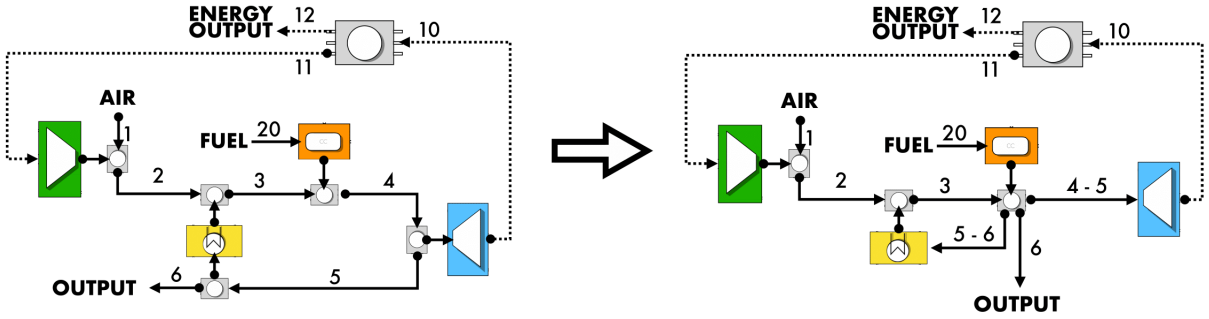

Figure A.4: Generation of the Product-Fuel Diagram for the Plant Illustrated in *Fig A.1*. Left Side: Topology with Support Blocks. Right Side: P-F Diagram Representation

To execute this transformation, the program identifies support blocks having only one fuel (such as the one connected to the turbine in *Fig A.4*) and eliminates them by connecting their output to the block from which the exergy comes from. The specific costs evaluated using the resulting topology (called *P-F diagram*) are then assigned to the corresponding streams in the physical setup.

A.3 Results

A.3.1 Geothermal Case Study: Hellisheiði Power Plant

The chosen case study focuses on the double-flash geothermal power plant at Hellisheiði, which combines heat and power generation. This power plant offers several noteworthy aspects for exergo-economic and exergo-environmental analysis, including the treatment of cooling towers and the concurrent generation of heat and power. A simplified schematic of the power plant can be seen in *Fig A.1.*

The geothermal fluid, extracted from the production well, undergoes an initial pressure reduction to 10 bar within the first steam separator. Subsequently, the steam is expanded in high-pressure (HP) turbines, comprising six turbines, each with a capacity of 45 MW, and then condensed in the HP steam condenser. A portion of the heat recovered from the condensing steam is utilized for heating the cold fresh water, which is then directed to the Reykjavìk district heating system. The condensed liquid from the HP separator undergoes flashing once more, and the resulting steam is directed to a low-pressure turbine with a capacity of 33 MW. Simultaneously, the condensed heat contributes to heating the fresh water destined for the district heating network.

The subsequent sections present the essential components required for a comprehensive exergo-economic analysis, along with the results derived from the application. Additionally, we have developed an in-house code within the EES environment to validate the outcomes of the developed tool. This EES code enables the calculation of both exergo-economic and exergo-environmental analyses.

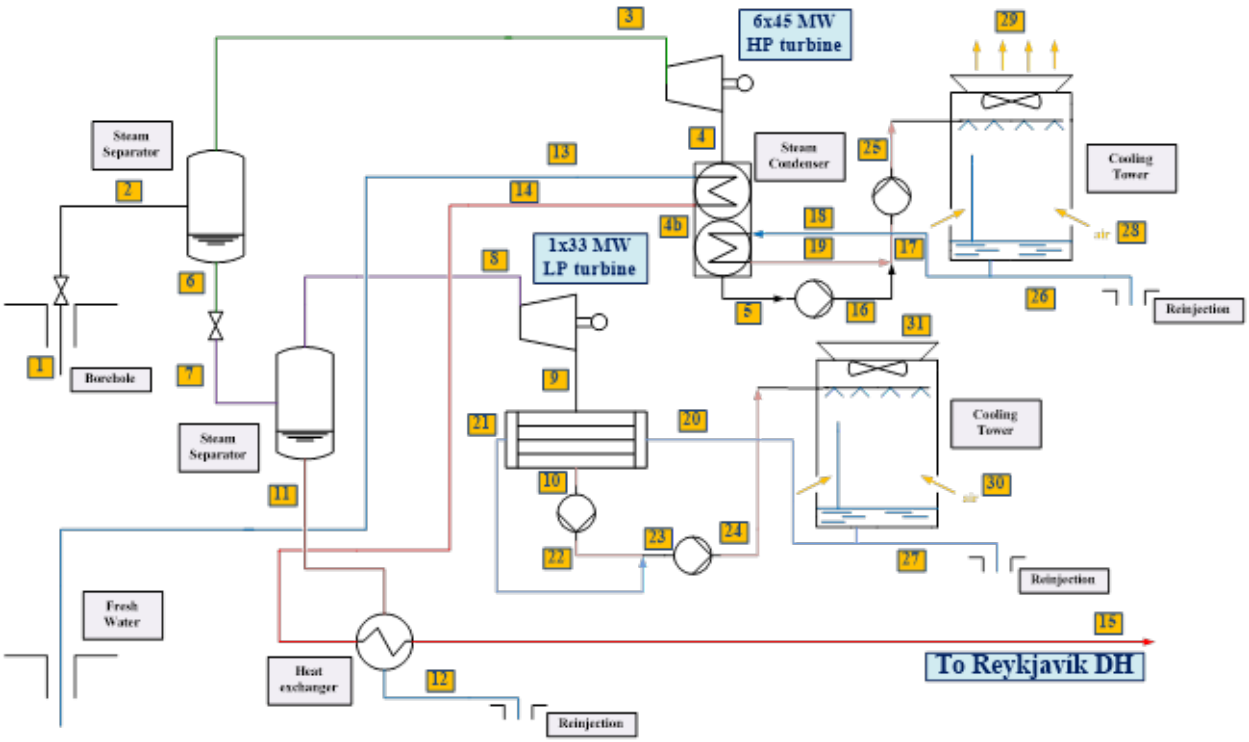

Figure A.1: Schematic of Hellisheiði power plant

A.3.2 Exergo-Economic Analysis

Inputs of the calculations

To assess the investment and operation and maintenance (O&M) costs of the power plant, an economic analysis was conducted. The initial step involved computing the costs of the individual components, following the methodologies outlined in [25]–[29]. The component costs were determined based on a standard mathematical relationship, which was subsequently refined with correction factors accounting for the component's class, working pressure, and equipment materials. These costs are denominated in dollars ($) and were later converted into euros (€) using a conversion factor of 0.92 [€/$]. The resulting value was then adjusted to the reference year (2015) using the CEPCI (Chemical Engineering Plant Cost Index) inflation index [30]. The Operation and Maintenance costs (O&M) for each component were established as a fraction (1.5%) of the Purchased Equipment Costs (PEC), in accordance with the suggestion by Schuster et al. [31].
The detailed calculation of the Total Capital Investment cost (TCI) is elaborated upon in [12]. Once TCI was determined, and considering the total annual operating hours of the power plant, $\dot{Z}_k$ in €/s was computed. For this analysis, a realistic working time of 7,446 hours per year over an expected plant lifespan of 30 years was assumed, which is a common value for geothermal power plants [32]. The cost of the incoming geothermal brine was set at 2.9 c€/kWh, accounting for well drilling expenses, while other input streams were considered cost-free.
Exergy values were calculated, and the plant's thermodynamic modeling was performed using an EES script as described in [11].

Exergo-Economic Analysis Results

The exergo-economic analysis serves to evaluate the costs associated with electricity and heat generation. The resulting Levelized Cost of Electricity (LCOE) stands at approximately 3.3 c€/kWh, falling within the anticipated range of 3 to 5 c€/kW, as recommended in [34]. Currently, the average national electricity production cost in Iceland from geothermal power plants hovers around 5.8 c€/kWh [35]. The cost of the co-generated heat is notably affected by the calculation parameters and ranges between 8.1 and 4.5 c€/kWh.
The table below delves into the impact of calculation settings on these values. $\dot{c}_{elect}$ represents the specific cost of electricity, $\dot{c}_{heat}$ denotes the specific cost of co-generated heat per unit of exergy, and $\dot{C}_{tot}$ represents the overall production cost, calculated as $\sum_{prod} \dot{c}_{prod}\dot{e}_{prod}$ that has to be compared with the overall investment in order to understand if the economic balance is respected.

Table A.1: Setting Comparison

Calculation Topology	$\dot{c}_{loss}$ setting	$\dot{c}_{elect}$ [€/kW]	$\dot{c}_{heat}$ [€/kW]	$\dot{C}_{tot}$ [€/s]
Support Block	$\dot{c}_{loss} = 0$	0.0325	0.0814	3.1577
PF Diagram	$\dot{c}_{loss} = 0$	**0.0335**	0.0546	3.1577
Support Block	$\dot{c}_{loss} = \dot{c}_{fuel}$	0.0325	0.0450	2.9698
PF Diagram	$\dot{c}_{loss} = \dot{c}_{fuel}$	0.0325	0.0450	2.9698

As can be seen from the table, changing the loss costing approach has a significant impact on $\dot{c}_{heat}$, moreover, the overall production cost decreases considering $\dot{c}_{loss} = \dot{c}_{fuel}$, showing that this approach results in an underestimation of the production costs. Besides, it is interesting to notice that the

calculation topology representation has an impact only considering $\dot{c}_{loss} = 0$, because otherwise no redistribution is needed, and that the *"PF Diagram"* topology succeeded in obtaining a better redistribution effect.
Please notice that the program returns specific cost with respect to the unit of exergy. This is not a problem for electricity, because electrical energy and exergy are equivalent, but can lead to some misunderstanding for the district heating energy production price. Anyway, the resulting price per unit of energy can be easily calculated as:

$$\dot{c}_{en} = \dot{c}_{ex}\dot{e}_x/\dot{w} \tag{A.10}$$

Where $\dot{e}_x$ is the exergy and $\dot{w}$ is the energy value of the stream. In Hellisheiði plant, production cost per unit of energy of the cogenerated heat is between 1.14 and 0.63 c€/kWh, again influenced by the calculation setting, considering a district heating power of 133 MW. Costs relative to other parameters can be calculated as well using the same approach, e.g. for a district heating network is interesting to access the cost in €/m3: in this case, the range is between 1.08 and 0.601 €/m3, considering a mass flow of 0.387 m3/s.
EES calculation result has been performed only considering the *"support block"* topology and $\dot{c}_{loss} = 0$. As expected, the results are exactly the same as the ones reported in *Tab A.1.* As was expected considering the fact that they both solve the same linear system.
Other results that can be obtained from the application are the specific and total cost for each stream, *Fig A.2.*
Moreover, for each *block* the app returns the following information:

- The overall investment cost PEC [€]
- The specific cost $\dot{Z}_k$ [€/s]
- The exergy lost $\dot{e}_{L,k}$ or destroyed $\dot{e}_{D,k}$ by the component [kW] and their "cost" [€/kJ]. The cost will be evaluated considering the average cost of the fuels, hence following the SPECO approach, regardless of the actual costing approach selected by the user. This is reasonable because in both cases it represents the cost that would have been spared if those losses had not existed.
- Multiple adimensional performance indicators:
  - Specific cost increase r_k across the component: $r_k = \left(\dot{c}_{prod} - \dot{c}_{fuel}\right)/\dot{c}_{fuel}$
  - component exergetic efficiency η_k: $\eta_k = \dot{e}_{prod}/\dot{e}_{fuel}$
  - Exergo-Economic factor f_k: $f_k = \dot{Z}_k/\left(\dot{Z}_k + \dot{c}_{fuel}\left(\dot{e}_{L,k} + \dot{e}_{D,k}\right)\right)$
  - Specific exergy destruction y_k: $y_k = \dot{e}_{D,k}/\left(\sum \dot{e}_{D,k}\right)$

A.3.3 Exergo-Environmental Analysis

Inputs of the calculations

In order to determine the environmental impact rate associated with the life cycle of components, the recently published work [11] has been taken as a reference for the input of this analysis. Concerning

Stream	Name	Exergy Value [kW]	Specific Cost [Euro/kJ]	Specific Cost [Euro/kWh]	Total Cost [Euro/s]
1	GEO Fluid Extraction	716166	5,09E-06	0,02	3,64
2	HP Steam Separator Input	607152	6,00E-06	0,02	3,64
3	HP Turbine Input	492082	6,03E-06	0,02	2,97
4	DH Condenser Input	154952	6,03E-06	0,02	0,93
4,1	HP Condenser Input	146569	6,03E-06	0,02	0,88
5	HP Condenser Output	7231	6,03E-06	0,02	0,04
6	HP Steam Separator Brine Output	115070	6,03E-06	0,02	0,69
7	LP Steam Separator Input	106698	6,51E-06	0,02	0,69
8	LP Turbine Input	57361	8,96E-06	0,03	0,51
9	LP Condenser Input	20430	8,96E-06	0,03	0,18
10	LP Condenser Output	775,8	8,96E-06	0,03	0,01
11	LP Steam Separator Brine Output	49337	8,96E-06	0,03	0,44

Figure A.2: Excel program output example, stream costs

the total environmental impact ($\dot{B}_{TOT,k}$), the wells and main valve emerged as the most impacting component, representing about 35% of the global effect. Both the HP turbine and HP Condenser contribution are mainly attributable to the specific cost of the component $\dot{y}_k$, while for the HP cooling tower, the environmental cost is dominated by exergy destruction.

Exergo-Environmental Analysis Results

The same results presented for the exergo-economic are returned also for the exergo-environmental analysis. The environmental cost of electricity is of 1.82cPts/MWh, generated by 81% by the specific cost of the component and by 19% by the exergy destruction, the environmental cost of heat is 4.42*10^{-2} cPts/m3 of generated hot water, derived by 73% by the specific cost of the components and 27% by the exergy destruction. These results are retrieved considering $\dot{c}_{loss} = 0$ and the *"PF diagram"* calculation topology. The environmental cost of heat is much dependent on the calculation setting, as seen in the exergo-economic analysis.

A.4 Conclusions

The developed tool allows non-experienced users to correctly perform exergo-economic and exergo-environmental analyses by ensuring that they are not forced to select the correct auxiliary equations set. In fact, the users are only required to provide the topology, the exergy values for each streams and the input costs in order to perform the analysis. Obviously, some basic knowledge of the topic is still required by the user in order to understand the results. Nevertheless, according to the experience of the authors, understanding what has generated a specific outcome is much easier than understanding the choice of an auxiliary equation which, in appearance, may seem arbitrary. Moreover the usage of such tool speed up the calculation process also for standard users as it remove the need of manually implementing the analysis in some thermodynamic simulation environment like EES.
The tool has been developed in Python hence it is extremely portable and easy to download. Furthermore, a new feature, that is still under development, will allows the tool to be launched by other programming languages, such as EES or MATLAB, in order to perform run time calculation on a topology that has been previously defined. To conclude, other features that are currently under development are:

- A much detailed exergetic analysis, modelled on the equation developed by Lozano and Valero [24]
- The implementation of the analysis for systems where different forms of exergy interact, such as chemical reactors or LNG regasification processes.
- A drag and drop user interface for the definition of the plant topology

References

[1] D. Fiaschi, G. Manfrida, P. Ungar, and L. Talluri, "Development of an exergo-economic and exergo-environmental tool for power plant assessment: evaluation of a geothermal case study," in *34th International Conference on Efficiency, Cost, Optimization, Simulation and Environmental Impact of Energy Systems (ECOS 2021)*, Tokyo, Japan: ECOS 2021 Program Organizers, 2022, pp. 24–35, ISBN: 978-1-7138-4398-6. DOI: 10.52202/062738-0003. [Online]. Available: http://www.proceedings.com/062738-0003.html.

[2] O. Turan and H. Aydin, "Exergetic and exergo-economic analyses of an aero-derivative gas turbine engine," *Energy*, vol. 74, pp. 638–650, Sep. 2014, ISSN: 03605442. DOI: 10.1016/j.energy.2014.07.029.

[3] S. Khanmohammadi, A. R. Azimian, and S. Khanmohammadi, "Exergy and exergo-economic evaluation of Isfahan steam power plant," *International Journal of Exergy*, vol. 12, no. 2, p. 249, 2013, ISSN: 1742-8297. DOI: 10.1504/IJEX.2013.053386.

[4] A. Z. Sahin, A. Al-Sharafi, B. S. Yilbas, and A. Khaliq, "Overall performance assessment of a combined cycle power plant: An exergo-economic analysis," *Energy Conversion and Management*, vol. 116, pp. 91–100, May 2016, ISSN: 01968904. DOI: 10.1016/j.enconman.2016.02.079.

[5] M. Leveni and R. Cozzolino, "Energy, exergy, and cost comparison of Goswami cycle and cascade organic Rankine cycle/absorption chiller system for geothermal application," *Energy Conversion and Management*, vol. 227, p. 113 598, Jan. 2021, ISSN: 01968904. DOI: 10.1016/j.enconman.2020.113598.

[6] D. Fiaschi, G. Manfrida, B. Mendecka, M. Shamoushaki, and L. Talluri, "Exergy and Exergo-Environmental analysis of an ORC for a geothermal application," *E3S Web of Conferences*, vol. 238, p. 01 011, Feb. 2021, ISSN: 2267-1242. DOI: 10.1051/e3sconf/202123801011.

[7] F. Siddiqui, M. El-Shaarawi, and S. Said, "Exergo-economic analysis of a solar driven hybrid storage absorption refrigeration cycle," *Energy Conversion and Management*, vol. 80, pp. 165–172, Apr. 2014, ISSN: 01968904. DOI: 10.1016/j.enconman.2014.01.029.

[8] Y. Chen, D. Zhao, J. Xu, J. Wang, and P. D. Lund, "Performance analysis and exergo-economic optimization of a solar-driven adjustable tri-generation system," *Energy Conversion and Management*, vol. 233, p. 113 873, Apr. 2021, ISSN: 01968904. DOI: 10.1016/j.enconman.2021.113873.

[9] D. Fiaschi, G. Manfrida, K. Petela, F. Rossi, A. Sinicropi, and L. Talluri, "Exergo-Economic and Environmental Analysis of a Solar Integrated Thermo-Electric Storage," *Energies*, vol. 13, no. 13, p. 3484, Jul. 2020, ISSN: 1996-1073. DOI: 10.3390/en13133484.

[10] E. Shayan, V. Zare, and I. Mirzaee, "On the use of different gasification agents in a biomass fueled SOFC by integrated gasifier: A comparative exergo-economic evaluation and optimization," *Energy*, vol. 171, pp. 1126–1138, Mar. 2019, ISSN: 03605442. DOI: 10.1016/j.energy.2019.01.095.

[11] V. Colucci, G. Manfrida, B. Mendecka, L. Talluri, and C. Zuffi, "LCA and Exergo-Environmental Evaluation of a Combined Heat and Power Double-Flash Geothermal Power Plant," *Sustainability*, vol. 13, no. 4, p. 1935, Feb. 2021, ISSN: 2071-1050. DOI: 10.3390/su13041935.

[12] D. Fiaschi, G. Manfrida, E. Rogai, and L. Talluri, "Exergoeconomic analysis and comparison between ORC and Kalina cycles to exploit low and medium-high temperature heat from two different geothermal sites," *Energy Conversion and Management*, vol. 154, pp. 503–516, Dec. 2017, ISSN: 01968904. DOI: 10.1016/j.enconman.2017.11.034.

[13] D. Fiaschi, M. Leveni, G. Manfrida, B. Mendecka, and L. Talluri, "Geothermal power plants with improved environmental performance: assessment of the potential for an Italian site," *E3S Web of Conferences*, vol. 238, p. 01 010, Feb. 2021, ISSN: 2267-1242. DOI: 10.1051/e3sconf/202123801010.

[14] L. Talluri, G. Manfrida, and D. Fiaschi, "Thermoelectric energy storage with geothermal heat integration – Exergy and exergo-economic analysis," *Energy Conversion and Management*, vol. 199, p. 111 883, Nov. 2019, ISSN: 01968904. DOI: 10.1016/j.enconman.2019.111883.

[15] D. Fiaschi, G. Manfrida, K. Petela, and L. Talluri, "Thermo-Electric Energy Storage with Solar Heat Integration: Exergy and Exergo-Economic Analysis," *Energies*, vol. 12, no. 4, p. 648, Feb. 2019, ISSN: 1996-1073. DOI: 10.3390/en12040648.

[16] H. Atalay and E. Cankurtaran, "Energy, exergy, exergoeconomic and exergo-environmental analyses of a large scale solar dryer with PCM energy storage medium," *Energy*, vol. 216, p. 119 221, Feb. 2021, ISSN: 03605442. DOI: 10.1016/j.energy.2020.119221.

[17] B. Mendecka, L. Lombardi, P. Gładysz, and W. Stanek, "Exergo-Ecological Assessment of Waste to Energy Plants Supported by Solar Energy," *Energies*, vol. 11, no. 4, p. 773, Mar. 2018, ISSN: 1996-1073. DOI: 10.3390/en11040773.

[18] S. Klein, *EES – Engineering Equation Solver*, Jun. 2020.

[19] The MathWorks Inc., *MATLAB*, 2022.

[20] Honeywell, *UniSim Design®*, 2022.

[21] C. Torres and A. Valero, "The Fuel Impact Formula Revisited," in *ECOS 2012 - THE 25TH INTERNATIONAL CONFERENCE ON EFFICIENCY, COST, OPTIMIZATION, SIMULATION AND ENVIRONMENTAL IMPACT OF ENERGY SYSTEMS*, Perugia, Italy, 2012.

[22] C. J. Okereke, O. A. Lasode, and I. O. Ohijeagbon, "Exergoeconomic analysis of an industrial beverage mixer system," *Heliyon*, vol. 6, no. 7, e04402, Jul. 2020, ISSN: 24058440. DOI: 10.1016/j.heliyon.2020.e04402.

[23] A. Lazzaretto and G. Tsatsaronis, "SPECO: A systematic and general methodology for calculating efficiencies and costs in thermal systems," *Energy*, vol. 31, no. 8-9, pp. 1257–1289, Jul. 2006, ISSN: 03605442. DOI: 10.1016/j.energy.2005.03.011. [Online]. Available: https://linkinghub.elsevier.com/retrieve/pii/S0360544205000630.

[24] M. Lozano and A. Valero, "Theory of the exergetic cost," *Energy*, vol. 18, no. 9, pp. 939–960, Sep. 1993, ISSN: 03605442. DOI: 10.1016/0360-5442(93)90006-Y.

[25] R. Turton, R. C. Bailie, W. B. Whiting, J. A. Shaeiwitz, and D. Bhattacharyya, *Analysis, Synthesis, and Design of Chemical Processes*. 2001, vol. 40, p. 9823, ISBN: 9780132618120. DOI: 10.1002/1521-3773(20010316)40:6<9823::AID-ANIE9823>3.3.CO;2-C. [Online]. Available: http://ptgmedia.pearsoncmg.com/images/9780132618120/samplepages/0132618125.pdf.

[26] C. H. Bloomster, P. D. Cohn, J. G. De Steese, *et al.*, "GEOCOST: A computer program for geothermal cost analysis," Tech. Rep., 1975.

[27] S. Soltani, S. Mahmoudi, M. Yari, T. Morosuk, M. Rosen, and V. Zare, "A comparative exergoeconomic analysis of two biomass and co-firing combined power plants," *Energy Conversion and Management*, vol. 76, pp. 83–91, Dec. 2013, ISSN: 01968904. DOI: 10.1016/j.enconman.2013.07.030.

[28] P. Roosen, S. Uhlenbruck, and K. Lucas, "Pareto optimization of a combined cycle power system as a decision support tool for trading off investment vs. operating costs," *International Journal of Thermal Sciences*, vol. 42, no. 6, pp. 553–560, Jun. 2003, ISSN: 12900729. DOI: 10.1016/S1290-0729(03)00021-8.

[29] P. Dumas, M. Antics, and P. Ungemach, "Report on geothermal drilling," *Europe Union: GeoElec*, 2013.

[30] W. M. Vatavuk, "Updating the CE plant cost index," *Chemical Engineering*, vol. 109, no. 1, pp. 62–70, 2002.

[31] A. Schuster, S. Karellas, E. Kakaras, and H. Spliethoff, "Energetic and economic investigation of Organic Rankine Cycle applications," *Applied Thermal Engineering*, vol. 29, no. 8-9, pp. 1809–1817, Jun. 2009, ISSN: 13594311. DOI: 10.1016/j.applthermaleng.2008.08.016.

[32] E. Gunnlaugsson, "The Hellisheidi geothermal project—financial aspects of geothermal development," *Short Course on Geothermal Development and Geothermal Wells, UNU-GTP and LaGeo.. http://www. os. is/gogn/unu-gtp-sc/UNUGTP-SC-14-12. pdf*, 2012.

AI Tools usage

The author acknowledge the use of ChatGPT3.5 as grammar corrector and for increase the overall thesis readability.

Acknowledgements

I would like to express my gratitude to prof.Manfrida for his continuous willingness in sharing his enormous expertise in the field and for the effort that he put in tutoring me during these three years. It has been very nice to discover during these three years how privileged I've been to be one of his students.
I would also like to thank prof.Fiaschi for his support, for the advice that he has given me, and for the opportunity that he is giving me in collaborating with him to the HOCLOOP project, which has proven to be an incredible opportunity to grow from both a personal and professional point of view.
To conclude I had to thank all my colleagues from the SERG group, for the friendship that has been born throughout these years.

Pietro Ungar, Florence, October 2023